Technical University of Crete

School of Electrical and Computer Engineering
Digital Image and Signal Processing Laboratory

FUNCTIONAL CONNECTIVITY IN THE WRIST SOMATOSENSORY NETWORK: AN EEG/MEG STUDY

Diploma Thesis

Konstantinos Politof

Diploma committee:

Supervisor: Prof. Michael Zervakis (Technical University of Crete)

Prof. Athanasios Liavas (Technical University of Crete)

Prof. Carsten Hermann Wolters (University of Münster, Institute for Biomagnetism and Biosignalanalysis IBB)

Chania, June 2019

……………………
Konstantinos Politof

Electrical and Computer Engineer
Technical University of Crete

ACKNOWLEDGEMENTS

First and foremost, I would like to address a special thanks to my supervisor Prof. Michael Zervakis for all his assistance and support from the beginning till the end of my thesis and to Prof. Carsten Hermann Wolters (University of Münster, Institute for Biomagnetism and Biosignalanalysis IBB) who kindly provided me with the dataset and offered me the opportunity to participate in his team for the duration of a three-months internship with the Erasmus+. Additionally, I would like to thank Prof. Athanasios Liavas for accepting to evaluate the work presented in this thesis as member of my thesis committee.

Moreover, I would like to thank Marios Antonakakis, Ph.D. student at the University of Münster, for his contribution and patience towards the completion of my thesis. Furthermore, I would like to thank Marios and his wife Maria for all their help during the three months stay in Germany.

Last but not least, I would like to thank my parents, Kallia and Manolis, my step father Michalis, my family, my life partner Stella and all my friends who stood by my side and supported me all these years to accomplish my dreams.

ABSTRACT

Motivation: We attempt to cover the lack of an integrated way to describe the early interactions within the primary somatosensory network. A combination of EEG and MEG (EMEG) has been shown to outperform single EEG or MEG in source analysis. EMEG may be a promising integrated way for the goal of the current study

Objective: The current study investigates the time-variant connectivity network of the primary somatosensory cortex by means of a functional source separation approach and source analysis of different measurement modalities.

Methods: The brain signals are recorded by the non-invasive modalities of electro- and magneto-encephalography (EEG and MEG) on a healthy subject, who participated in an experiment for measuring somatosensory evoked responses by median nerve stimulations on the right wrist. After the prepossessing, time-locked analysis (TLA) is applied for the reduction of the non-cerebral activity in both, EEG and MEG. After the estimation of the somatosensory evoked potentials (SEP) and fields (SEF), the goal was the extraction of the time-functional (or functional) components. The separation of the somatosensory functional components is accomplished by a semi-blind algorithm, the functional source separation (FSS), which uses a priori information of each functional component to extract the functional sources (FSs) for each modality. The back-projected SEP and SEF responses are calculated for each functional source. The EMEG measurement modality is estimated by these EEG and MEG back-projected data of the same components. Then, for every back-projected data of each modality (EEG, MEG or EMEG) and for each of their time points we find a solution to source localization by using the sLORETA algorithm and we obtain the source waveforms. The used individual and realistic head model includes six tissue compartments (scalp, skull compacta, skull spongiosa, cerebrospinal fluid, gray and white matter), brain anisotropy and calibrated skull conductivities. The source waveforms all of the modalities were set the base for the estimation of the effective and time-varying primary somatosensory connectivity network using time-varying Generalized Orthogonalized Partial Directed Coherence (tv-GOPDC).

Result: Three time instants are chosen for each modality EEG, MEG and EMEG to highlight the thalamocortical and corticocortical interactions. The results show that the three modalities share similar information flow patterns with negligible amplitudes on the cortico-thalamic connections for EMEG compare to the single modality EEG. Since MEG could not detected any flow between the thalamic and the cortical areas, the current result indicated that the complementarity of both EEG and MEG in EMEG can lead to an sufficient and stable result suppressing simultaneously the spurious flows within the primary somatosensory network.

Novelty: The novelty of this study is that it provides a subject specific pipeline to investigate the connectivity of the functional sources within the primary somatosensory cortex. For a specific subject, we use both its functional information for the modalities EEG, MEG and their combination, EMEG. It exploits anatomical characteristics to extract the realistic head model that is produced by FEM and combines novel techniques (FSS for the functional component separations, EEG, MEG or EMEG source analysis upon a realistic FEM head model and effective connectivity based on tv-GOPDC) to reveal functional connectivity.

Keywords: Electroencephalography (EEG), Magnetoencephalography (MEG), primary somatosensory cortex (SI), Functional Source Separation (FSS), Standardized low resolution brain electromagnetic tomography (sLORETA), Finite element method (FEM), effective connectivity, time-varying Generalized Orthogonalized Partial Directed Coherence (tv-GOPDC)

ΠΕΡΙΛΗΨΗ

Κίνητρο: Θα θέλαμε να καλύψουμε την έλλειψη ενός ολοκληρωμένου τρόπου για την περιγραφή των πρώιμων αλληλεπιδράσεων στο κύριο σωματοαισθητικό δίκτυο.

Στόχος: Η τρέχουσα μελέτη διερευνά το δίκτυο συνδεσιμότητας στον χρόνο του πρωτογενούς σωματοαισθητικού φλοιού μέσω μιας προσέγγισης διαχωρισμού των λειτουργικών πηγών και εντοπισμό αυτών για τους διαφορετικούς τρόπους μέτρησης

Μέθοδοι: Τα σήματα του εγκεφάλου καταγράφονται με τις μη επεμβατικές μεθόδους ηλεκτρο- και μαγνητο- εγκεφαλογραφίας (EEG και MEG) για ένα υγιές άτομο, το οποίο υποβλήθηκε σε διέγερση του μέσου νεύρου στον δεξιό καρπό. Μετά την προεπεξεργασία, εφαρμόζουμε χρονική μέση ανάλυση (time-locked analysis -TLA) για τη μείωση της μη εγκεφαλικής δραστηριότητας τόσο στο EEG όσο και στο MEG. Μετά από την εκτίμηση των σωματοαισθητικών προκληθέντων δυναμικών (SEP) και των πεδίων (SEF), ο στόχος είναι η εξαγωγή των χρονικά λειτουργικών (ή λειτουργικών) στοιχείων. Ο διαχωρισμός των σωματοαισθητικών λειτουργικών στοιχείων γίνεται με έναν ημι-αυτοματοποιημένο (semi-blind) αλγόριθμο για διαχωρισμό λειτουργικών πηγών (functional source separation-FSS), ο οποίος χρησιμοποιεί εκ των προτέρων πληροφορία για κάθε λειτουργικό στοιχείο για την εξαγωγή των λειτουργικών πηγών (FSs) για κάθε τύπο. Για κάθε λειτουργική πηγή υπολογίζονται τα οπισθο-προβαλλόμενα (back-projected) SEP και SEF δεδομένα. Το συνδυασμένο σήμα EMEG για κάθε λειτουργική πηγή υπολογίζεται με τη χρήση αυτών των δεδομένων EEG και MEG. Στη συνέχεια, προχωράμε στον εντοπισμό των πηγών σε συγκεκριμένη θέση του μοντέλου του εγκεφάλου με τον αλγόριθμο sLORETA για κάθε για κάθε χρονικό σημείο και σαρώνοντας όλο το χρονικό διάστημα, μέχρι την απόκτηση των κυματομορφών των διπόλων. Ένα ρεαλιστικό μοντέλο κεφαλής παράγεται την μέθοδο πεπερασμένων στοιχείων FEM χρησιμοποιείται στον εντοπισμό των πηγών το οποίο περιλαμβάνεται από έξι τμήματα (τριχωτό μέρος του κεφαλιού, συμπαγές κρανίο, σπογγώδες κρανίο, εγκεφαλονωτιαίο υγρό (ΕΝΥ), γκρι και λευκή ουσία) και συμπεριλαμβάνει την ανισοτροπία της λευκής ύλης και του κρανίου. Τέλος, για κάθε τύπο δεδομένων παρουσιάζουμε τη λειτουργική συνδεσιμότητα που προκύπτει χρησιμοποιώντας τις κατωφλιομένες τιμές από το time-varying Generalized Orthogonalized Partial Directed Coherence (tv-GOPDC) των κυματομορφών διπόλων (sLORETA) για συγκεκριμένες χρονικές στιγμές.

Αποτελέσματα: Τρεις χρονικές στιγμές επιλέγονται για κάθε τύπο EEG, MEG και EMEG για να αναδειχτούν οι αλληλεπιδράσεις μεταξύ θαλάμου και φλοιού και μεταξύ διαφορετικών περιοχών στον φλοιό. Τα αποτελέσματα δείχνουν ότι οι τρεις μέθοδοι μοιράζονται παρόμοια μοτίβα ροής πληροφοριών με πιο αμελητέα δραστηριότητα στις κορτικο-θαλαμικές συνδέσεις για το EMEG σε σύγκριση με το EEG από μόνο του. Δεδομένου ότι το MEG δεν ανιχνεύει καμία ροή μεταξύ του θαλαμου και των περιοχών στον φλοιό, το τρέχον αποτέλεσμα έδειξε ότι η συμπληρωματικότητα τόσο του EEG όσο και του MEG στο EMEG μπορεί να οδηγήσει σε επαρκές και σταθερό αποτέλεσμα που καταστέλλει ταυτόχρονα τις παρασιτικές ροές μέσα στο πρωτογενές σωματοαισθητικό δίκτυο.

Καινοτομία: Η καινοτομία αυτής της μελέτης είναι ότι συνδιάζει μια σειρά από μεθόδους σε ένα τυποποιημένο διάγραμμα ροής για την συνδεσιμότητα των λειτουργικών πηγών μέσα στον στον κύριο σωματοαισθητικό φλοιό. Για κάθε άτομο χρησιμοποιούμε τις λειτουργικές του πληροφορίες από τα EEG, MEG και τον συνδυασμό τους EMEG, καθώς και τα ανατομικά χαρακτηριστικά για την εξαγωγή του ρεαλιστικού μοντέλου κεφαλής. Επιπλέον, η μελέτη μας συνδυάζει νέες τεχνικές (FSS για τον διαχωρισμό των λειτουργικών στοιχείων, EEG, MEG ή EMEG για τον εντοπισμός πηγής μαζί με ένα ρεαλιστικό μοντέλο κεφαλής FEM και την συνδεσιμότητα παραγώμενη από tv-GOPDC) για να τονίσει τη λειτουργική συνδεσιμότητα.

TABLE OF CONTENTS

LISTS OF FIGURES

Chapter 1:

Chapter 2:

Chapter 3:

LISTS OF TABLES

CHAPTER 1: INTRODUCTION

1.1 STRUCTURE OF CURRENT STUDY

The current study explores the functional connectivity in the wrist somatosensory network, which is measured by non-invasive electro- and magneto-encephalography (EEG and MEG) techniques. The aim and objective are presented at the end of Introduction, after addressing the framework of our study. More specifically, the Thesis structure proceeds as follows.

Chapter 1 includes the introduction to this study, with **sections 1.2-1.4** describing the anatomy and the physiology of the nervous system, brain and primary somatosensory cortex. Furthermore **section 1.5-1.6** presents all the non-invasive brain measurements being used in this study. Finally, **sections 1.7-1.8** refer to related work and outline the aim and innovation of the study.

Chapter 2 presents the methodology for acquisition of the functional connectivity. The content of **section 2.2** presents all the preprocessing steps that should be done before moving on to further analysis methods. **Section 2.3** describes methods for isolation of principal, independent and functional components for EEG and MEG data. Interesting signal components can be derived from principal component analysis (PCA), independent component analysis (ICA) and functional source separation (FSS), respectively. Following the neuro-physiological signal characterization, **section 2.4** describes the source localization (forward and inverse problem) of an unknown source(s) which produces an electrical activity inside the brain from the observed data (EEG or MEG). Finally, **section 2.5** introduces the methods for extracting the connectivity among brain regions.

Chapter 3 forms the basic experimentation of this study and presents the results derived. We briefly outline the content and aim of each section as follows: **Section 3.2:** preprocessing and computation of the average of the trials at each channel (Time-Locked Analysis TLA) of the EEG and MEG data. **Section 3.3:** isolation of the functional sources (FSs) for each time-locked data by the algorithm of functional source separation (FSS). **Section 3.4:** extraction of the source waveform of each FSs of the EEG, MEG and EMEG data using the realistic head model and sLORETA. **Section 3.4:** computation and representation on graphs of the connectivity between the source waveforms of each modality.

Chapter 4 addresses a comparison with other studies as to highlight the new findings and discuss the value of the joint processing of EEG and MEG. Furthermore, it provides the concluding remarks and important methodological notes resulting from our study.

1.2 NERVOUS SYSTEM

The nervous system (NS) (Purves, et al., 2004; Widmaier, et al., 2008) consists of billions of neurons and it is vital for the proper function of the human being. The nervous system is divided in three main functions: sensory input, integration and motor output. The sensory input deals with the detection of an external or internal stimulus of the body. Then, the analysis and the interpretation of this input comprise the integration function. The last function is the motor output which is the response of the body to the stimulus by activating the effector organ. Furthermore, the nervous system is divided into two main structural systems: the central nervous system (CNS) and the peripheral nervous system (PNS). The CNS consists of the brain and the spinal cord and coordinates the analysis and the management of sensory and motor information (integration state). The PNS is composed of cranial and spinal nerves and connects the CNS with the rest of the body. Additionally, the PNS separates into two functional areas: sensory (afferent) and motor (efferent) division. Also, the motor (efferent) division is subdivided into visceral or automatic and somatic motor system. In a sequential operation scenario, an external or internal stimulus (or a combination of the two) is detected by the receptors and that signal is conveyed by the afferent nerve fibers to the spinal cord and then to the brain for further analysis (sensory input stage of NS or sensory division of PNS). In some cases, the body should react immediately, for example to avoide injuries (e.g. when the hand approaches fire). These types of quick actions are taken by the spinal cord, which is called the reflex arc. In these situations, the spinal cord lets the brain know about the event produced (as a feedback mechanism), for further investigation. Otherwise, the analysis and interpretation of the input signal is processed mainly by the brain. Both situations refer to the integration stage in CNS, whereas the response of the body has to do with the motor division of PNS. After the decision for reaction has been made, the response signal transfers either from the brain to the spinal cord or immediately to the spinal cord and from there to the effector organ via the efferent nerve fibers.

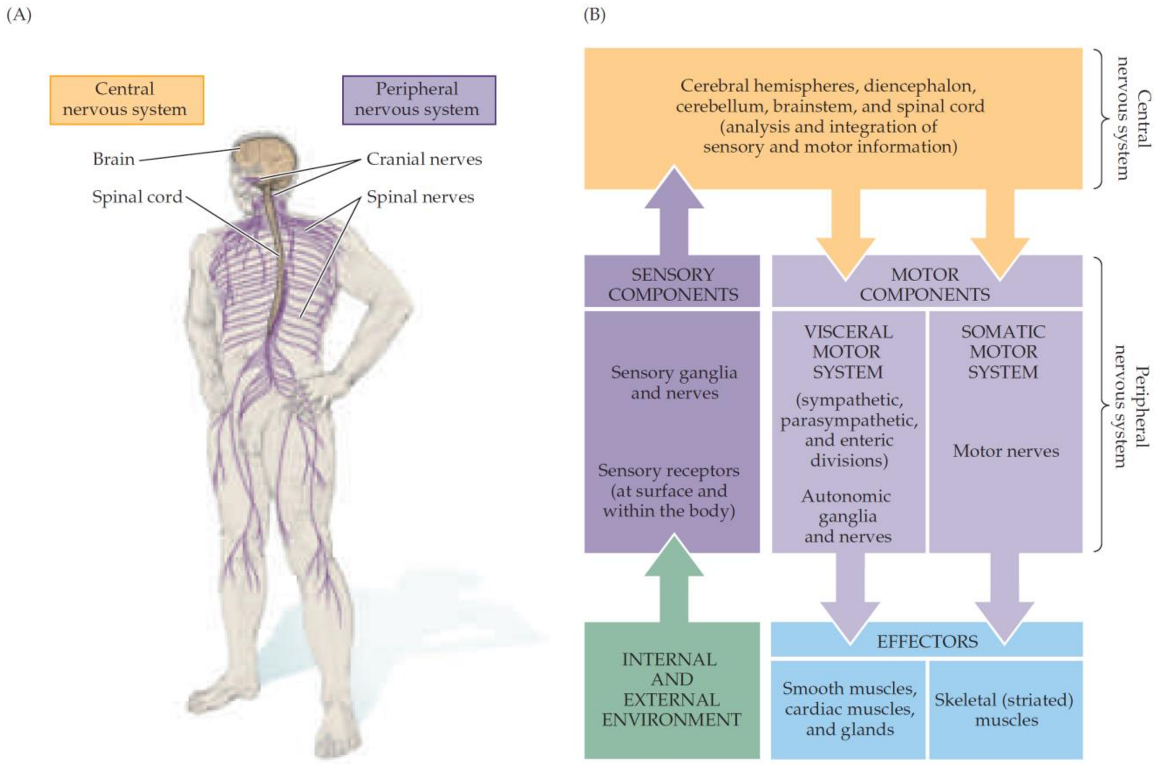

Figure 1. 1: a) The central and the peripheral nervous system and b) their interactions, adapted from (Purves, et al., 2004).

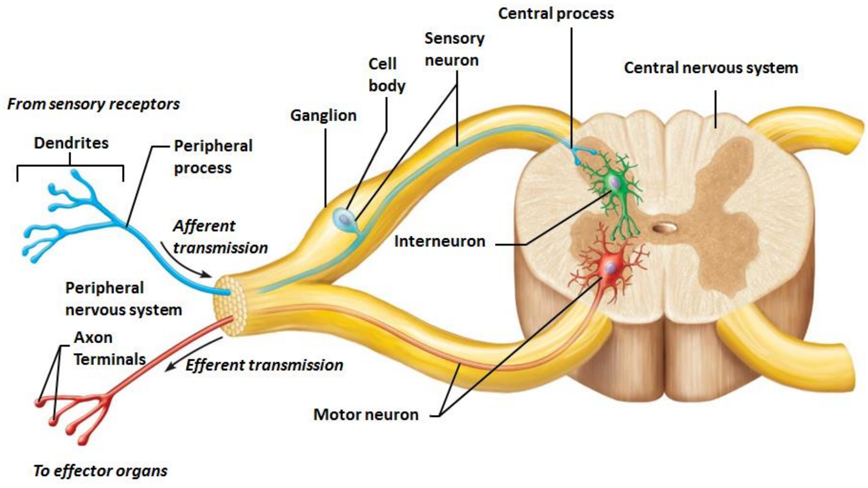

Figure 1. 2: The reflex arc, the sensory receptors receive the signal and they send to the spinal cord. The spinal cord maybe could be respond imminently with interneuron or send the signal to the brain. Then then motor signal travels via the motor neurons to the effector organ. In this figure is also visible the gray and white matter of spinal cord (adapted from 2012 Pearson Education, Inc.)

The operation of the nervous system becomes feasible due to the communication between neurons. No matter the structure of different neurons, they share four common parts: the dendrites, soma (cell body), axon and terminal buttons (Figure 1. 3). The interaction between the neurons is partially electrical and partially chemical. The synapse (Figure 1. 4 a) is the area where two neurons are close enough, so they can interact without touching and the gap between them is the synapse cleft. The presynaptic neuron (i.e. transmitter) sends the chemical signals (the neurotransmitters) through the synapse cleft to the postsynaptic neuron (i.e. receiver). The latter receives it via its receptors on dendrites and then the chemical signal is transformed to electrical signal. Sometimes, it is also possible the presynaptic neurons to stimulate part of the soma of the postsynaptic neuron. The stimulations cause changes to the membrane potential of neuron, which are the postsynaptic potentials PSPs. There are two types of PSPs: the excitatory (EPSPs) that depolarizes and the inhibitory (IPSPs) that hyperpolarizes the membrane potential. If the sum of PSPs exceeds a specific threshold, then a temporal electrical activation of the neuron occurs, which is going to transmit the electrical message through the axon to the terminal buttons. This electrical activation is called action potential (AP). More specifically, the states of the action potential are (Figure 1. 4 b):

1. The stimulations to the postsynaptic neuron make the membrane potential to diverge from the resting state at $-70mV$. If the potential exceeds the threshold of $-55\ mV$, then the activation of the AP starts.
2. In the Depolarization state, the Sodium ion Na^{+}gates open and more Na^{+} will enter inside the axon. This inflow creates a positive potential that increases rapidly until it reaches an upper limit, approximately at $+40\ mV$. The transfer of this potential through the axon is the AP.
3. Then, the Na^{+}gates close and the Potassium ion K^{+} gates open, so the influx of Na^{+}stops and the outflow of K^{+} starts outside the membrane. This will make the potential to decrease rapidly. This is the state of Repolarization.
4. The final state before the neuron returns in the resting state is the Hyperpolarization, where the potential reaches a negative lower limit until the neuron restores the original balance of K^{+} and Na^{+} inside it. In this state, the AP has already been transmitted via the axon.

When the electric signal reaches the terminal buttons, the new chemical message will be released through the synapses to inform the other neurons. In summary, this is the process of integration that each neuron conducts (Sanei & Chambers, 2007).

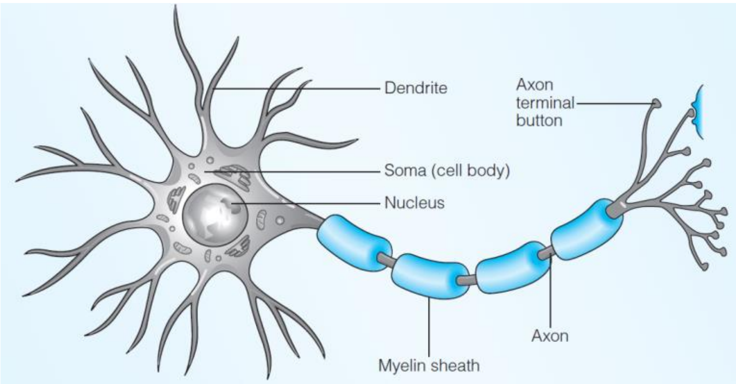

Figure 1. 3: The base structures of a neuron, adapted from (Sternberg & Sternberg, 2012).

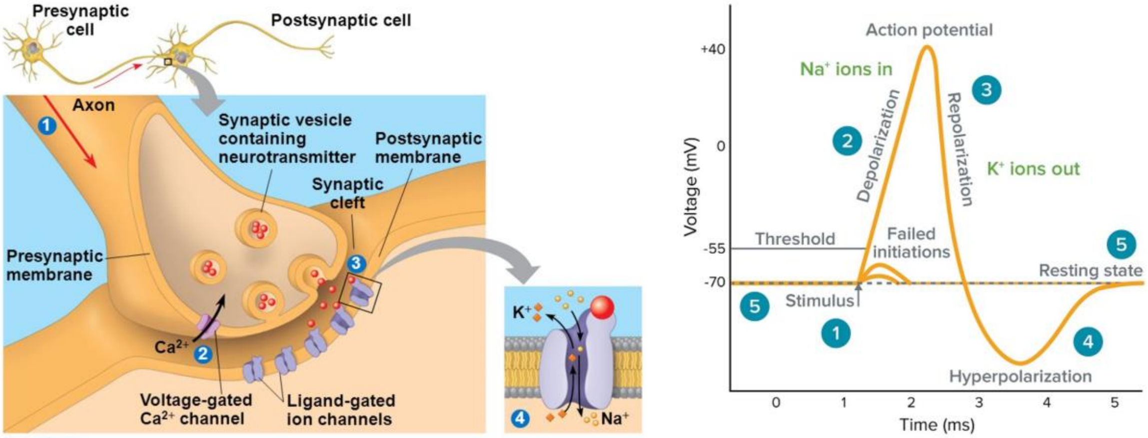

a) b)

Figure 1. 4: a) The synapse (adapted from 2011 Pearson Education, Inc.) b) The states of the action potential (adapted from www.moleculardevices.com)

The classification of neurons (Kibble & Halsey, 2008) could be done with several systems, because of variations at the size, shape and the functional properties of neurons. Consequently, the generalized categories are:

1. The numbers of neurites:
    - Unipolar neurons have only one neurite (e.g. primary sensory neurons)
    - Bipolar neurons have two neurites (e.g. retina bipolar cell)
    - Multipolar neurons are the most common type and have three or more neurites (e.g. spinal motor neuron)

2. The organization of dendrites. Specifically in cerebral cortex, there are two general types:
    - Pyramidal neurons
    - Stellate (star-shaped) neurons
3. Axon length:
    - Golgi type I neurons have long axons and convey the information among areas of the nervous system.
    - Golgi type II neurons have short axons and are activated in local areas.
4. Functional classification:
    - Primary sensor (afferent) neurons transfer the sensory information to the CNS.
    - Motor (efferent) neurons end on muscles and activate them.
    - Interneurons are the neurons that mediate between other neurons and are the majority of neurons.
5. Type of neurotransmitter being released.

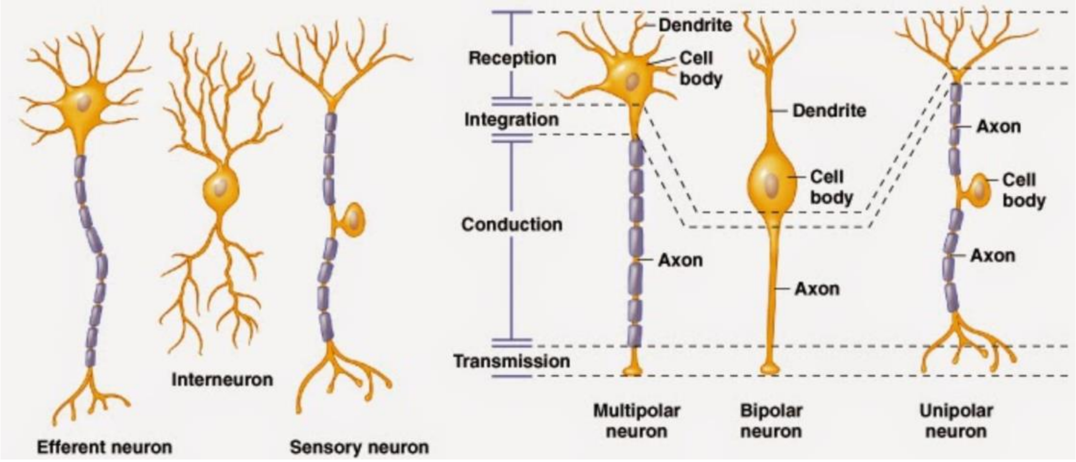

a) b)

Figure 1. 5: This figure shows two types of classification of neurons a) the functional classification and the b) classification by the numbers of neurites (adapted from 2006 Pearson Education, Inc. publishing, as Benjamin Cummings)

1.3 ANATOMY OF THE HUMAN BRAIN

The brain is responsible for the most important functionalities of the humans. Thus, the human head contains a certain number of layers, some of which protect the brain from injuries. In short, from the outer to inner parts of the human head, it consists of scalp (or skin), aponeurosis, periosteum, skull (hard-spongiform-hard layers), meninges (dura mater, arachnoid mater and pia mater), arachnoid mater, cerebrospinal fluid (CSF, which flows under the arachnoid mater) and the brain.

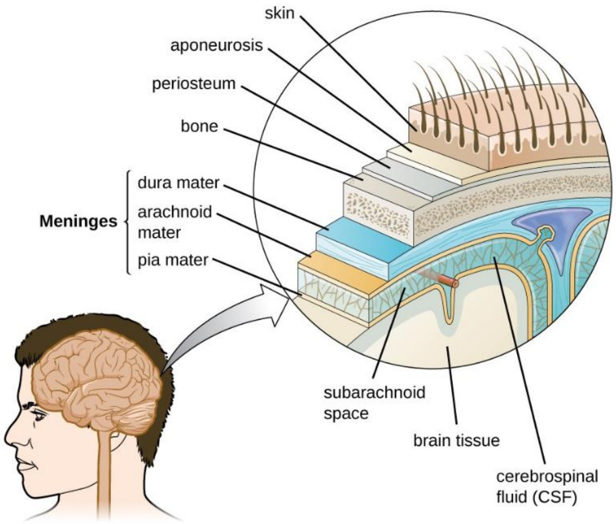

Figure 1. 6 : The different layers of the human head. In this work we focus on the scalp (skin), skull (bone), CSF and the brain (adapted from National Institutes of Health)

The brain (Purves, et al., 2004; Widmaier, et al., 2008; Kibble & Halsey, 2008; McCorry, 2009; Sternberg & Sternberg, 2012; Kandel, et al., 2013) is located inside the skull and it is surrounded by the CSF that is also flowing inside the brain through the cerebral ventricles. The brain is divided in four regions: the cerebrum, diencephalon, brainstem and cerebellum. The cerebrum consists of two cerebral hemispheres, the right and the left, which are separated by the longitudinal fissure and connected by the corpus callosum, as well as some other structures. The cerebral hemispheres are responsible for the opposite side of the body (i.e. the left hand is controlled by the right cerebral hemisphere and vice versa). The cerebral hemispheres consist of two layers, the outer layer of gray matter which is the cerebral cortex and an inner layer of the white matter. The gray matter is mainly composed of cell bodies of neurons and glial cells, the latter of which have a supporting role in holding the neuron together, so it has darker color and its functionality serves as a processing unit. The gray matter can be found in the cerebral cortex and in the inner part of the spinal cord. The neurons inside the gray matter at the cerebral cortex have a vertical organization of six layers (Figure 1. 8 and Figure 1. 9). The white matter consists primarily of myelinated fiber tracts (i.e. a bundle of axons with common origin and destination), which connect areas between the gray matter inside the brain and the spinal cord. There are three categories of nerve fiber inside the brain that can be distinguished according to the regions which connect (Figure 1. 10):

- Projection fibers, which connect areas of the cerebral cortex with the spinal cord or low parts of the brain (e.g. thalamus). They could be efferent (i.e. descending) if they carry motor information from cerebral cortex to the low regions of the brain or spinal cord. Alternatively, they could be afferent (i.e. ascending) if they carry sensory information the reverse way of the efferent.
- Association fibers, which transmit information between different parts of the gray matter inside the same cerebral hemisphere.

- Commissural fibers, which connect and transmit information between the two cerebral hemispheres (e.g. corpus callosum).

The cerebral cortex has an average thickness of about 3mm, although it is highly folded. Its surface has a toothed appearance; the ridges are referred as guri (singular: gyrus) and the grooves are the sulci (singular: sulcus). The sulcus could be shallow or deeper grooves and if they are deeper they are called fissures. The cerebral cortex for each hemisphere is divided into four lobes (Figure 1. 7), where the location and the main functionality is listed below:

- The Frontal lobe, which is located in the front part of the brain controls the movement, speech and higher intellectual activities. Furthermore, posterior to the frontal lobe there is the primary motor cortex.
- The Parietal lobe, which is behind the frontal lobe is associated with the sense of touch, pain and temperature. Additionally, anterior to the parietal lobe there is the primary somatosensory cortex.
- The Occipital lobe, which is located at the back of the brain behind the parietal lobe controls the vision.
- The Temporal lobe, which is underneath the frontal and parietal lobes is associated with auditory and memory.

Furthermore, the lobes of each hemisphere are distinguished by three different sulcus:

- The central sulcus is a shallow groove that differentiates the frontal lobe from the parietal lobe.
- The lateral sulcus (or Sylvian fissure) is a fissure that separates the temporal lobe from the frontal lobe and with a large area of parietal lobe.
- The parieto-occipital sulcus (or Parietooccipital fissure) is a fissure that differentiates the occipital from the parietal and temporal lobe.

The thalamus is a primary part of the diencephalon, which is a mass of gray matter and mainly functions as a relay center for sensory signals from the spinal cord to the cerebrum and vice versa. The brainstem contains the midbrain, the pons and the medulla oblongata and it carries the information from the spinal cord to the other main parts of the brain. Finally, the cerebellum mainly has to do with the control of movement.

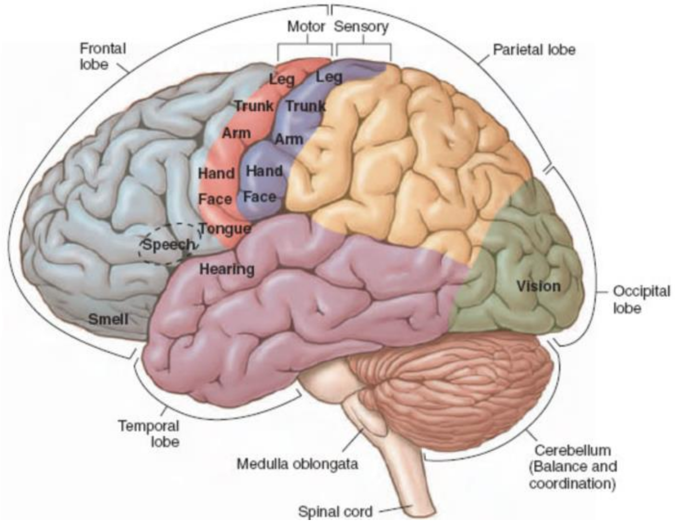

Figure 1. 7: The lobes of the left cerebral hemisphere, the primary motor and sensory cortex, brainstem and the cerebellum (adapted from biocyclopedia.com)

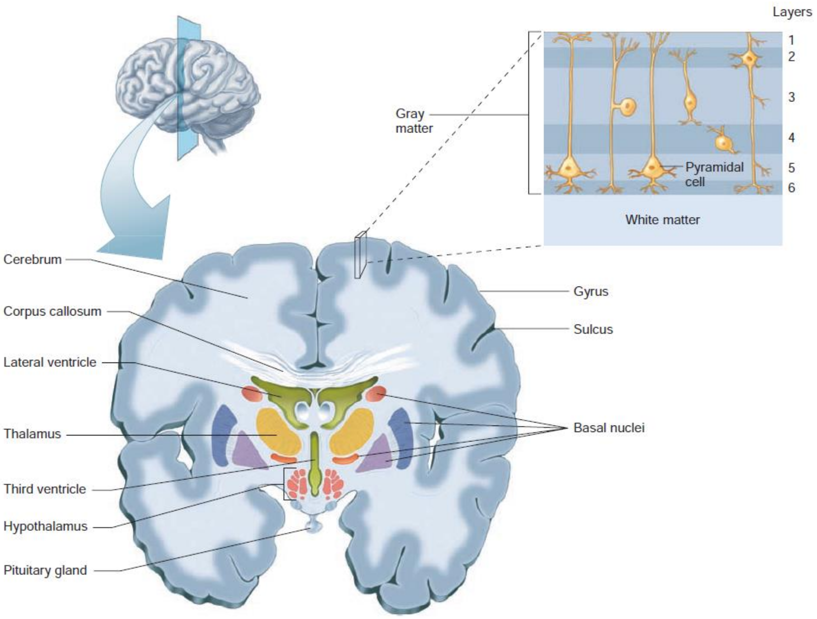

Figure 1. 8: Frontal slice of brain showing interior structures (e.g. thalamus) and the six layers of gray matter, adapted from (Widmaier, et al., 2008).

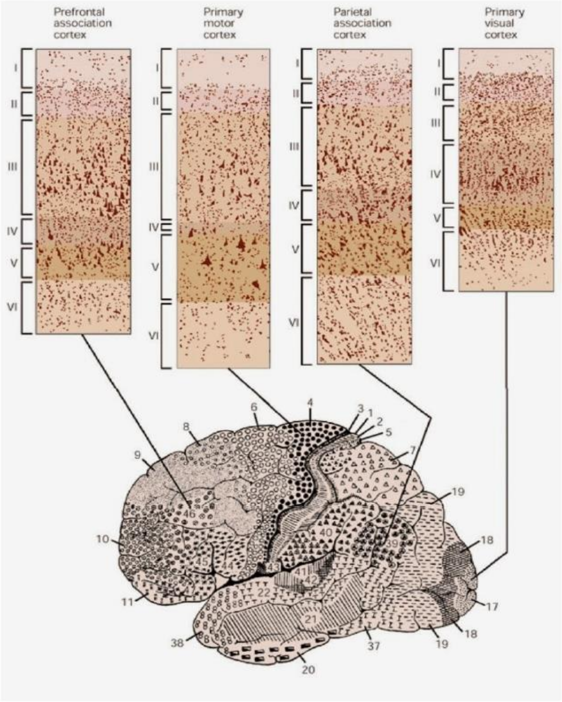

Figure 1. 9: The six layers of the gray matter for some regions at the cerebral cortex, adapted from (Kandel, et al., 2013).

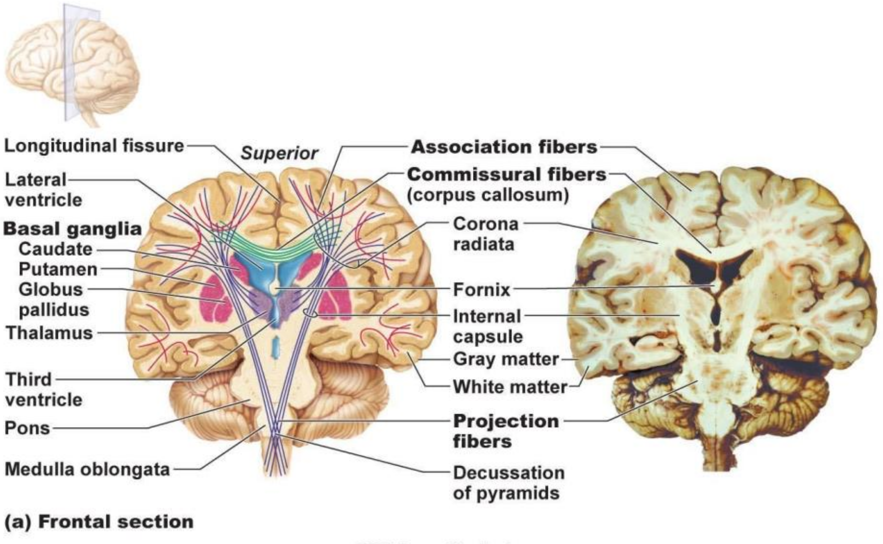

© 2011 Pearson Education, Inc.

Figure 1. 10: The different types of fiber (projection, commissural and association) inside the white matter of brain (adapted from 2011 Pearson Education, Inc.)

1.4 PRIMARY SOMATOSENSORY CORTEX

The primary somatosensory cortex (S1) (Purves, et al., 2004) is located in the postcentral gyrus of the parietal lobe (Figure 1. 7) and controls the somatic sensory information of the body. Each part of the human body occupies a region at S1 (Figure 1. 11). The sensory signals transfer through the afferent nerves from the receptors to the spinal cord, brainstem, thalamus and finally to the primary somatosensory cortex (Figure 1. 12). These signals are sent to the ventral posterior (VP) complex of the thalamus, which consists of the ventral posterior lateral nucleus (VPL) that conveys the signal from body to S1 and the ventral posterior medial nucleus (VPM) that transmits from face to S1. The Brodmann's areas divide the postcentral gyrus into four regions: 3a, 3b, 1 and 2. The main functionality of each region is described as follows: the area 3a responds to proprioceptive stimulus, the areas 3b and 1 respond to cutaneous stimulus and the area 2 processes the tactile and proprioceptive stimulus.

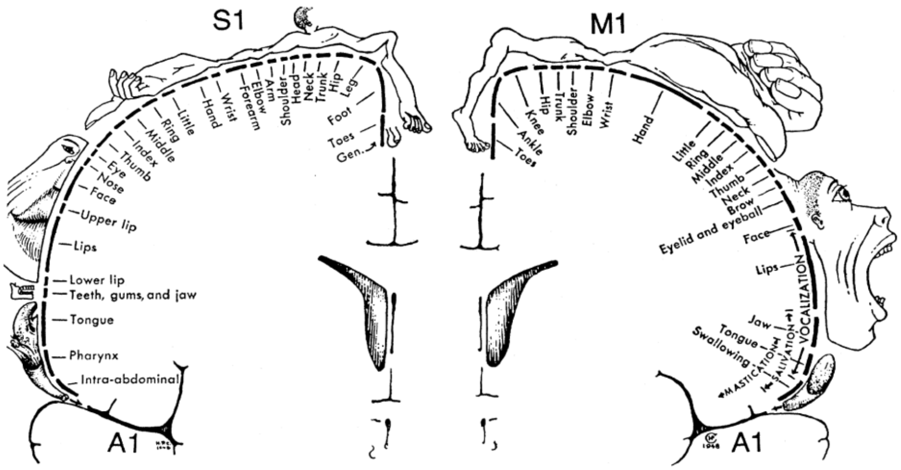

Figure 1. 11: The representation of parts of human body (Homunculus) at primary somatosensory cortex (S1) at the left cerebral hemisphere and motor (M1) cortex at the right cerebral hemisphere, adapted from (Hämäläinen, et al., 1993).

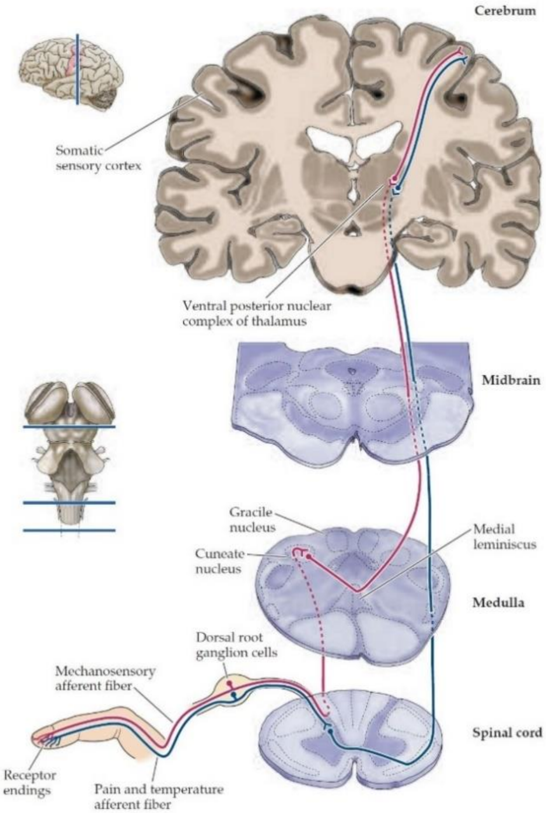

Figure 1. 12: The pathway of somatosensory signal from the receptors to the primary somatosensory cortex via the afferent fibers. Mechanosensory information (e.g. touch, vibration) reach the brain through the three red neurons. The pain and temperature sensation are transferred via the three blue neurons, respectively, adapted from (Purves, et al., 2004).

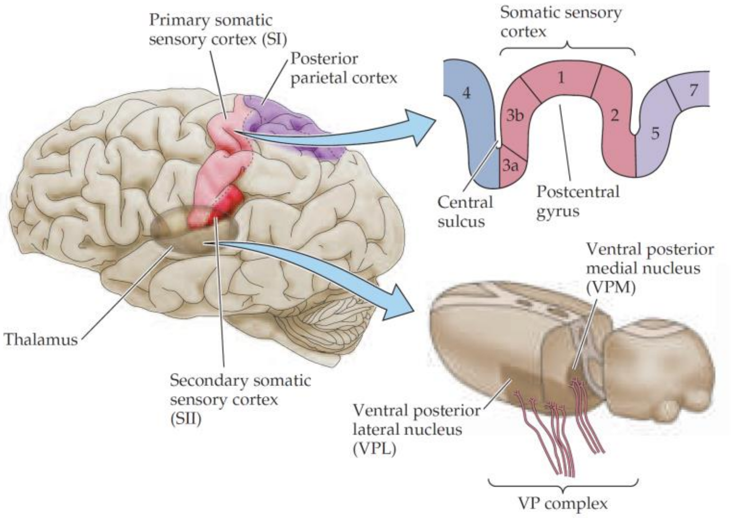

Figure 1. 13: The primary somatosensory cortex (S1) and its division (i.e. the postcentral gyrus) into four Brodmann's areas: 3a, 3b, 1 and 2. The ventral posterior (VP) complex and its division into the ventral posterior lateral nucleus (VPL) and the ventral posterior medial nucleus (VPM). Adapted from (Purves, et al., 2004).

1.5 NON-INVASIVE BRAIN MEASUREMENTS

The functions of the brain are manifested by the induced electrical fields due to the electrical activations of the neurons, which also produces vertical magnetic fields. The synchronous activation of nearby neurons evokes an electromagnetic field that can be recorded by the proper non-invasive systems on the outskirt of the head. These functional characteristics mapped on the electric potential and the magnetic field can be recorded by electroencephalography (EEG) and magnetoencephalography (MEG), respectively. Furthermore, the non-invasive magnetic resonance imaging (MRI) acquires anatomical characteristics of the human head and its inner tissues in the brain. Thereby, the combination of the functional information from EEG, MEG or their combination EMEG with the anatomical information in the MRI sequences can lead to more accurate and realistic investigation of the brain's functionality. The EEG, MEG and their comparison will be further analyzed in this section.

1.5.1 ELECTROENCEPHALOGRAPHY (EEG)

The EEG system (Sanei & Chambers, 2007) consists of electrodes, amplifiers, filters and analogue to digital converters (ADCs) to store the signal into computer or a needle (pen)-type register to draw the signal on the paper (Figure 1. 14).

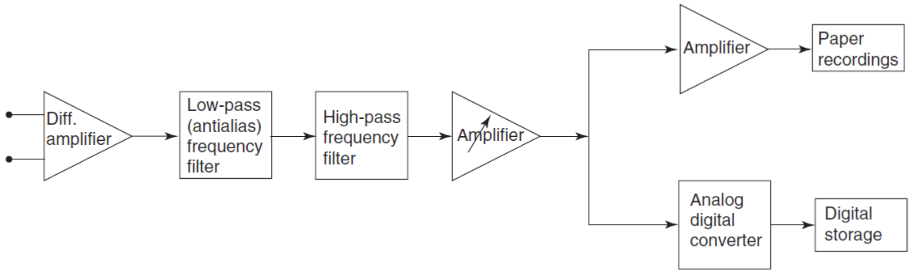

Figure 1. 14: The EEG system diagram of a single channel, adapted from Wiley Encyclopedia of Biomedical Engineering, Copyright © 2006 John Wiley & Sons, Inc.

The electrodes of the EEG device record the electrical activity on the scalp (Figure 1. 15 a) over time through the electrode caps, which form the most common type for multichannel recordings. The positions of the electrodes are determined by international systems, such as the 10-20 system or its extensions, such as the 10-10 system. For instance, the 10-20 system has 21 electrodes (Figure 1. 15 b) that are placed with intervals at 10% or 20% of constant distances measured by anatomic landmarks on the skull. These landmarks are the nasion (Nz), the inion (Iz) and the left and right pre-auricular points (A1 and A2). The electrode positions are named and characterized by two parts. The first denotes the brain area that the positions are located: Fp (Frontal pole), F (Frontal), C (Central), P (Parietal), O (Occipital) and T (Temporal). The second part can be either a number or z; if it is an even number, then the position is located on the right side, if it is an odd number on the left side, while the letter z from zero implies a position at the center. In addition, if the EEG study needs higher density, the 10-10 system can be used, which is an extension of the 10-20 system with 75 electrodes or other systems up to 256 electrodes. Each channel of EEG measures the corresponding electric potential on the scalp, which is the difference between an electrode and a reference in a range of μV. That reference depends on the montage we choose (e.g. it could be another electrode, common average reference etc.), which is appropriate to highlight our data. Then, the signal of each channel passes through the filters to reduce the external noise, it is further amplified, digitized and stored to a computer for subsequent analysis.

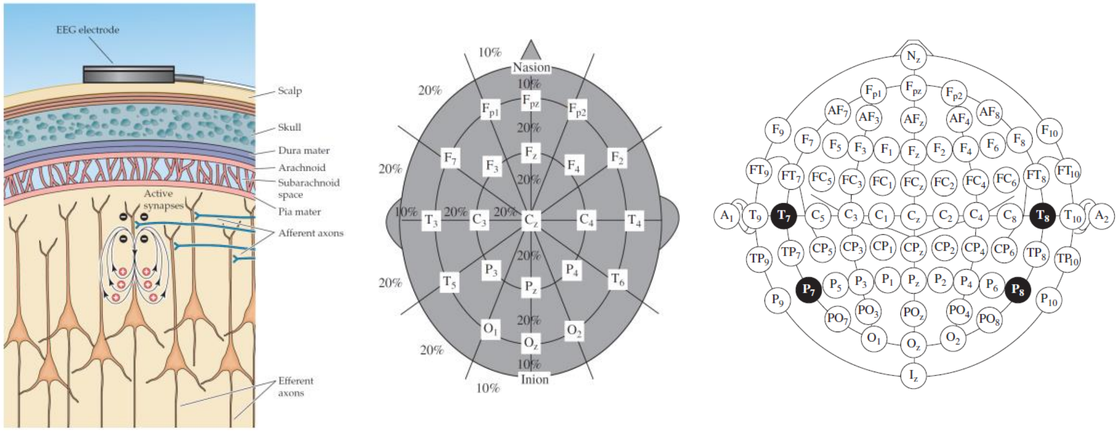

a) b) c)

Figure 1. 15: a) The EEG electrode on the scalp is adapted from (Purves, et al., 2004) and b) The 10-20 system with 21 electrodes c) The 10-10 system with 75 electrodes which is an extension of the 10-20 system, both b and c are adapted from (Sanei & Chambers, 2007).

1.5.2 MAGNETOENCEPHALOGRAPHY (MEG)

The synchronous electrical activation of neurons produces a weak perpendicular magnetic field that can be recorded by the MEG device in a range of fT (Hämäläinen, et al., 1993). MEG is very sensitive to external magnetic fields that are not produced by the brain (Figure 1. 17 b). For instance, the earth's static geomagnetic filed is higher at 8-9 orders of magnitude and the noise that could be found in the laboratory, such as produced by electronic devices, is some orders larger than the brain magnetic fields. To reduce the external noise, the MEG system is placed inside a magnetically shielded room (MSR, Figure 1. 16 b) with additional electronic and pre-processing techniques being applied. The subject is either sitting or lying, with the head placed as close as possible to the curved part of the MEG Dewar (Figure 1. 16 a), where the sensors are. Only the brain's magnetic field that passes outside the head can be measured by the MEG (Figure 1. 17 a). The tiny amplitude of brain magnetic fields can be detected by very sensitive devices, the superconducting quantum interference devices (SQUIDs). Because the SQUIDs are small, less than $1mm$ in diameter, they have the drawback of poor coupling to the magnetic field. This problem can be solved by using superconductive flux transformers (Figure 1. 18 b), which have large coils (pickup coils) that collect more magnetic flux and are connected to small coils (input coils) that transfer that stronger flux more compact to the SQUIDs. These complex superconductive sensors need to be cooled down to be efficient, by using liquid helium at temperature $-296^{\circ}\mathrm{C}$, where sensor resistivity is minimal avoiding losses in magnetic flux. There are two main types of pickup coils (Figure 1. 18 a), with different sensitivity and noise cancelation profiles:

- The Magnetometer is a single coil and is the simplest form; it is more sensitive to detect remote and deeper sources but is also influenced by ambient noise. It has bigger absolute amplitude when it is on the left and the right of the current source and zero when it is right above it.
- The gradiometers consist of two opposite connected coils and are divided into two categories depending their arrangement either at axial or planar. Thus, they can remove the residual ambient noise inside the shielded room. The axial gradiometer has similar sensitivity with the magnetometer without the influence of the noise. The planar gradiometer has the maximum sensitivity on the top of the source and is more suppressed on the left and the right of the source.

The pickup coils operate in non-linear form of various orders that make them more efficient, which could be controlled electronically or digitally. After the measurement of the signals, they are passed through a set of similar processes as the EEG, in order to be digitalized. Moreover, it is worth mentioning that the MEG does not take into consideration the position of the head. In order to solve this problem, before the measurement we attach 3-5 head-position indicator (HPI) coils at fiducial landmarks of the head, which will during the measurement indicate the position of the head. This procedure makes possible the combination with other modalities such as MRI and it is also used for detecting head movements that could be artifacts.

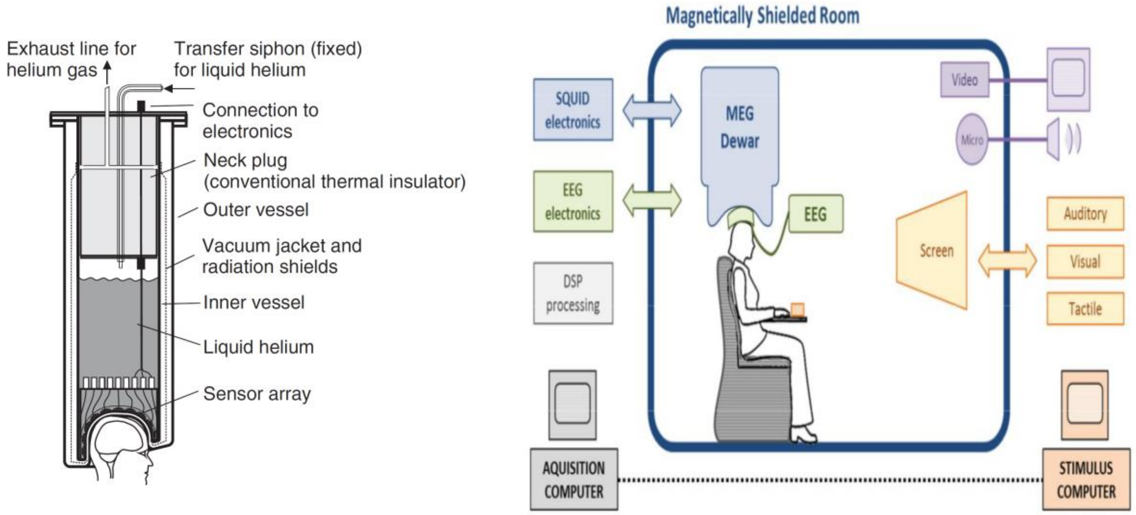

a) b)

Figure 1. 16: a) The structure of a MEG Dewar adapted from, (Hansen, et al., 2010) b) The MEG system combined with the EEG system, adapted from (Galán, 2013).

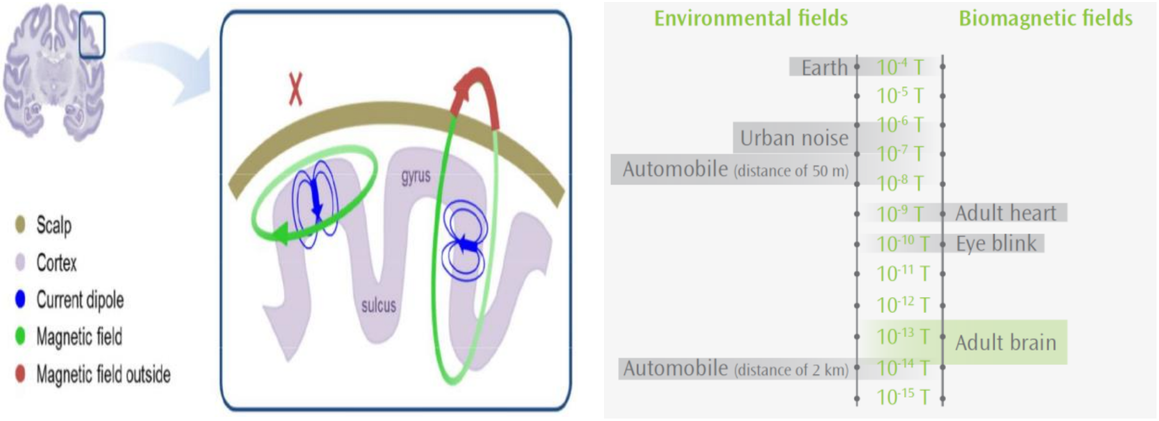

a) b)

Figure 1. 17: a) Only the magnetic field that pass through outside the head can be detected by the MEG, adapted from (Galán, 2013) and b) The amplitude of different magnetic fields (adapted from, www.elekta.com)

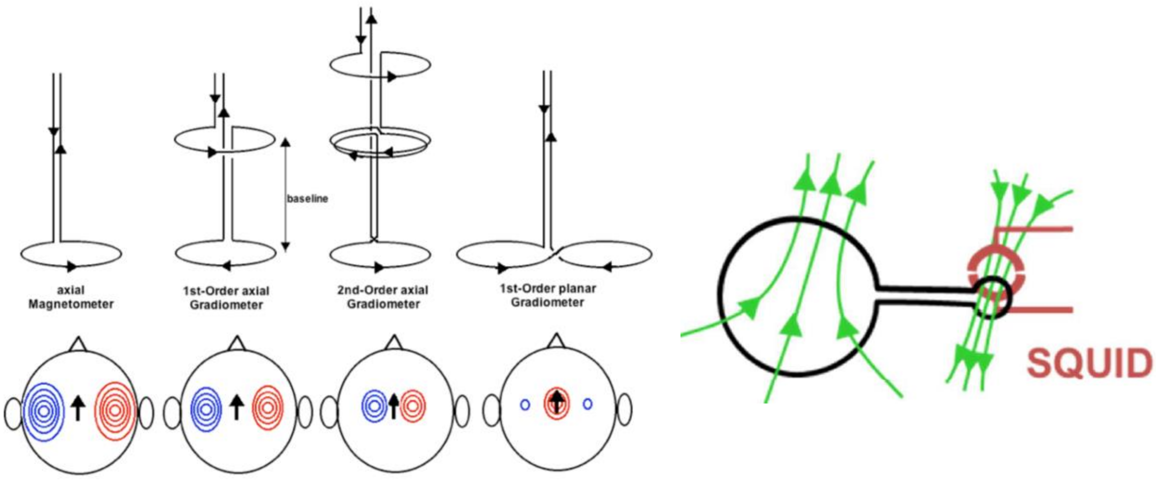

A) B)

Figure 1. 18: A) This figure illustrate how different types of pickup coils measure the magnetic field of a source (black arrow adapted from, Singh 2006) and the figure B) shows a flux transformer with magnetometer that collects the magnetic flux and conveys it to the SQUID, adapted from (Galán, 2013).

1.5.3 COMPARISON BETWEEN EEG AND MEG

Both EEG and MEG modalities (Hämäläinen, et al., 1993; Fuchs, et al., 1998; Sanei & Chambers, 2007; Sharon, et al., 2007; Hansen, et al., 2010; Aydin, et al., 2014; Aydin, et al., 2017; Antonakakis, et al., 2018) measure the brain activity that originates from the same electrical source inside the brain, but these measurement fields are perpendicular to each other (Figure 1. 19). Comparing these modalities with other non-invasive techniques, they have the advantage of higher temporal resolution in a range from one to some milliseconds but are lacking in spatial resolution. Moreover, their spatial resolution is directly dependent on the number of electrodes/sensors that are used for recording the measurement. The MEG is more sensitive to sources being tangential to the skull and are located superficial close to the sensors (Figure 1. 17 a). In contrast, the EEG can detect activities from any orientation (i.e. both tangential and radial) of the source, even if it is deeper in the brain. Neither modality can detect sources whose activations are suppressed inside the brain (silence sources). The anisotropy of the skull and the white matter affect much more the EEG measurements in comparison with MEG, because the magnetic field is transparent to them. Additionally, the preparation time for MEG measurements is lower compared to EEG, because in the latter the right contact between the scalp and the electrodes must be first ensured. Long-term recordings are possible with EEG but not with MEG, where the subject has to be immobile. The EEG is inexpensive in relation to the MEG due to the expensive installation (e.g. shielded room) and maintenance of the latter. Finally, by comparing their recording means we reach to the conclusion that EEG and MEG have complementary information, so the combination of them by simultaneous recording EMEG provides more accurate results.

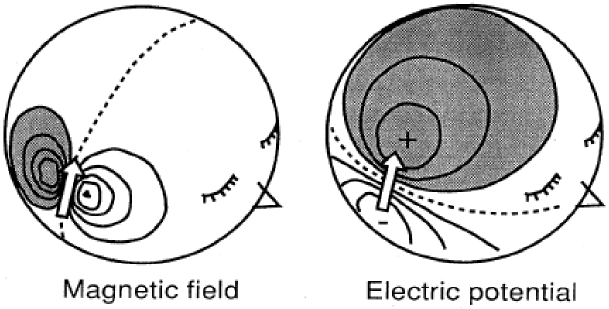

Figure 1. 19: The electric potential and magnetic field that are produced by the same electrical source (white arrow adapted from (Hämäläinen, et al., 1993)).

1.6 SOMATOSENSORY EVOKED ACTIVITIES

The somatosensory evoked potentials or fields (SEPs or SEFs) (Allison, et al., 1991a; Allison, et al., 1991b; Allison, et al., 1992; Buchner, et al., 1994; Haueisen, et al., 2007) are produced by the brain when it is stimulated by a touch stimuli. Those activities can be recorded by non-invasive brain measurements such as electro- and magneto-encephalography (EEG and MEG), respectively. The electrical activity inside the brain is represented by an equivalent current dipole (ECD) that gathers a synchronous activation by nearby neurons. This study focuses on early somatosensory components which are evoked by a median nerve stimulus. The somatosensory evoked activities can be divided into two temporal parts after the median nerve stimulus: short and long latency activations. The former are activations in the first 40 ms post-stimulus and are generated in peripheral nervous system, brainstem, thalamus and the corresponding portion of primary somatosensory cortex. The latter are activations after 40 ms post-stimulus and are generated in primary somatosensory cortex and additional cortical regions. In this work we will study the connectivity between four functional components/activations at the low-frequencies (up to 250 Hz). Apart from these components, we observed at the MEG measurement data the activation at 25 ms, which will be also referred below even though we excluded it from this study due to its very low amplitude. These components are named by the positive or negative activations which is observed at frontal or parietal lobes at a specific time instant. The first component, called P14, is coming at 14 ms and is located at subcortical region of the brain and it's mainly orientation is radial. Because the component P14 (frontal and parietal positivity) is located deep inside the brain and is the immediately preceding activation before the signal is relayed to the cortex and we model its location at the VPL of the Thalamus. The short-latency activations at 20 ms and 30 ms are the P20/N20 (frontal positivity/parietal negativity) and the N30/P30 (frontal negativity/parietal positivity). The positive activation at 20 ms is followed by a negative activation at 30 ms so P20-N30, vice versa. Each of the activations at 20 ms and 30 ms is produced by one mainly tangential generator at 3b Brodmann's areas. The intermediate component at 25 ms the P25/N25 (also referred to as P22/N22) is located in area 1 of the primary somatosensory cortex and produced by a radial source. The long-latency activation P45/N45 (frontal positivity/parietal negativity) at 45 ms is generated by combination of radial and tangential source close to 3b area. To recap, the explanation of the components in this study can be derived by four sources:

1. One deep mainly radial source which is located at the VPL of the Thalamus for the component P14.
2. Two mainly tangential sources in 3b Brodmann's areas:
   - One source for the activation P20/N20
   - One source for the activation N30/P30
3. A cortical source nearby to 3b area for the component P45/N45.

1.7 RELATED WORK

Preprocessing methods for noise cancelation and artifact rejection have been used in every study of EEG and MEG. The methodology of time-lock analysis has been studied in order to drastically reject the noise, while preserving synchronous activity. Furthermore, component analysis through PCA and ICA has been widely examined in association with several pathologies, such as epilepsy, Parkinson's and Alzheimer's, in order to better split the signal activity and recover the response dynamics with temporal and spatial region associations and/or interactions (Hyvärine, et al., 2001; Handy, 2005; Sanei & Chambers, 2007; Hansen, et al., 2010; Gross, et al., 2013). Localization methods have been widely used for both EEG and MEG signals, in order to trace the origins of brain activities as response to evoked and inherent events (including memory, cognition, education, etc.) and detect problematic regions in the brain in neuro-degenerative pathologies (Wolters, et al., 2006; Bast, et al., 2007; Hallez, et al., 2007; Grech, et al., 2008; Lucka, et al., 2012; Gross, et al., 2013; Aydin, et al., 2014; Aydin, et al., 2017; Antonakakis, et al., 2018). Studying the dynamics of brain signals, methods of synchronization have been widely established and used for either the signal recordings at several electrodes, or the extracted components, or even the signals of localized dipoles (Ioannides, 2007; Gross, et al., 2013; Omidvarnia, et al., 2013; Porcaro, et al., 2013; Hassan, et al., 2014; Bastos & Schoffelen, 2016).

1.8 AIMS AND INNOVATION OF CURRENT STUDY

The major aim of this thesis is to study the somatosensory response and its transmission in the brain. Since the somatosensory cortex is just a small area in the brain, the accurate localization of neurophysiological signals is of utmost importance. The first goal of this study is to appropriately decouple the brain signals (either EEG or MEG) so as to allow for more accurate localization. Furthermore, the response signals from a somatosensory event originate from the thalamus and transmit to the surface on the cerebrum S1 region. Thus, the localization of response signals should be able to handle dipoles close to the surface but also at deeper parts of the brain. The second goal or the thesis is to examine the capabilities of localization methods (particularly sLORETA) in terms of accurate dipole localization at different depths. We should mention here that an electric dipole perpendicular to the scalp produces a recordable electric field but its magnetic field is tangential to the head surface and cannot be recorded. However, a dipole tangential to the scalp produces both electric and magnetic fields that are recorded in both EEG and MEG. Thus, several parts of the response are mostly detectable on EEG. The third goal of this study is to consider the possibilities of EEG and MEG recordings in identifying the various parts of the somatosensory response and trace the synchronization in time. Nevertheless, we should note that EEG is most amendable to noise, its resolution is lower and localization potential is much worse that MEG. Thus, it becomes imperative to consider both EEG and MEG in a joint analysis, taking under account their different characteristics (especially in terms of response recordings). Thus, the fourth goal of the thesis is to consider the potential of joint analysis of EEG and MEG recordings, with the appropriate pre-processing and component analysis. These issues are studied in the next sections and applied on real EEG and MEG recordings, kindly provided by Prof. Carsten Hermann Wolters (University of Münster, Institute for Biomagnetism and Biosignalanalysis IBB).

CHAPTER 2: METHODS

2.1 SUMMARY OF CHAPTER

This chapter includes a brief overview of all methodological tools used in this Thesis, from the raw data acquisition to connectivity between brain areas for the wrist somatosensory. First, we discuss the way to simultaneously read in the same structure the EEG and MEG data for enabling joint preprocessing. We identify and separate the SEPs and SEFs trials of our experiment data from other recordings. Subsequently, the data will be preprocessed and separated at EEG and MEG structures and, for each structure, the bad channels and trials would be rejected. We also convert the gradiometer in a 3^{rd} order for more efficient suppression of noise in MEG. For each structure, an average of the trials at each channel will also be derived to drive the time-lock analysis (TLA). Then, we discuss the algorithm of functional source separation (FSS), which is a semi-blind source separation technique that extracts separately the functional sources (FSs). This process is of particular interest, since each FS reveals an enhanced functional behavior of the corresponding somatosensory component. After that, each FS component is back-projected to reveal the structure of the underlying brain component and source localization methods are used to derive the source waveforms for each back-projected FS data. This study investigates the interactions at connectivity level between these waveforms. To accomplish this, the waveforms are fitted to a multivariate auto-regressive (MVAR) model. The coefficient matrix of the MVAR model is used to compute the causalities between pairs, revealing their connectivity structure and the dynamics of the brain somatosensory response. Finally, the connectivity structure is displayed on a directional graph for a specific time of interest. The processing steps are schematical presented in Figure 2.1.

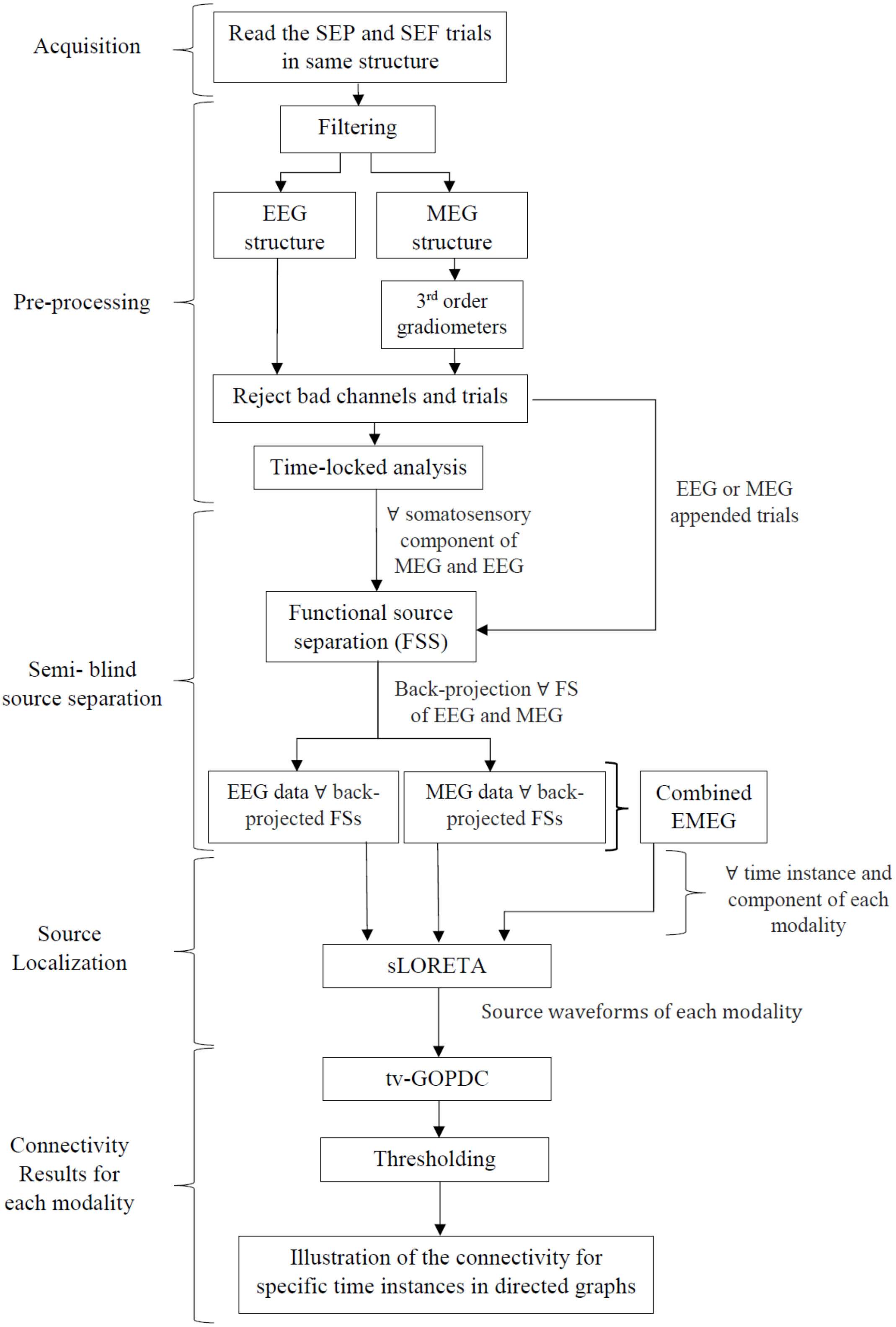

Figure 2. 1: The diagram with the steps of methodology which used in the current study

2.2 PREPROCESSING

As mentioned above, the state of preprocessing begins after the isolation of the data trials for the somatosensory evoked potentials and fields (SEPs and SEFs) produced by a stimulus at the median nerve of the hand. Thus, we have in the same structure the EEG and MEG measurements and the same preprocessing is applied. More specifically, we apply: a band-pass Butterworth filter 6th order from 20 to 250 Hertz to keep the frequencies of interest, a Notch filter for eliminating the harmonics of power line noise (PLN) of 50 Hz (European vs 60 Hz of American standard) and the window of each trial is defined as the time interval from -0.1 to 0.2 seconds triggered by the same event. Then, we separate the EEG and MEG structures, we clean them from channel and/or trial outliers and the MEG gradiometers are converted in a 3rd order. The rejection of outliers in trials was detected by the metrics zvalue, variance and kurtosis. The rejection of bad channels was achieved by visual inspection. The trials of somatosensory evoked activities are triggered by the same stimulus so they can be considered as synchronous. Therefore, we can apply time-locked analysis (TLA) (Hämäläinen, et al., 1993; Sanei & Chambers, 2007) to compute the average of the trials at each channel. The advantages of this technique are the increase of the signal-to-noise ratio (SNR) of the somatosensory component and the removal of noise that is non-synchronous to the stimulus, such as noise from eye movements and the heart. Additionally, the global mean field power (GMFP) (Lehmann & Skrandies, 1980; Esser, et al., 2006) is computed on the time-locked data, revealing the general activation structure within the data. For instance, the GMFP of EEG can be calculated by the equation:

$$\mathrm{GMFP}(t) = \sqrt{\frac{\sum_i^k \left(V_i(t) - V_{mean}(t)\right)^2}{k}} \qquad (2.2.1)$$

where, k is the number of the channels, V_i is the voltage at channel i and V_{mean} is the mean voltage in all channels.

2.3 COMPONENT ANALYSIS

2.3.1 INTRODUCTION OF COMPONENT ANALYSIS

The component analysis finds many different applications in studying the bio-signal. This chapter introduces methods of component analysis for EEG and MEG data. The first method we examine is the principal component analysis (PCA) (Jolliffe, 2002), which attempts to make the data uncorrelated (principal components PCs). It can also be applied for dimensionality reduction decreasing the data dimensions and the computational complexity. The PCA is also used as the first stage before applying the independent component analysis (ICA) (Hyvärinen & Oja, 2000; Hyvärine, et al., 2001), which is now searching for components that are independent (independent components ICs). In this work we also focus on the functional source separation (FSS) (Barbati, et al., 2006; Porcaro, et al., 2013) which is a variation of ICA with the addition of a priori information revealing an enhanced functional behavior of the each functional component.

2.3.2 PRINCIPAL COMPONENT ANALYSIS (PCA)

Principal component analysis (PCA) (Jolliffe, 2002) is a statistical procedure that transforms the data linearly to a new coordinate system with an orthogonal transformation based on data covariance. The new data is projected on the principal components (PCs) which are orthogonal to each other. Initially, before the application of PCA, a first step is to remove the mean from all data dimensions. The next step applies unit variance to the data dimensions, performing data standardization with zero mean and unit variance. From the PCA procedure the data will be whitened, which means they will be uncorrelated, in addition to having unit variance on each direction. The first principal component is chosen to represent the first projected coordinate axis which has the highest variation of data, the second principal component represents the second projected coordinate axis with the next highest variation under the constraint that it is orthogonal to the previous axis, and so on. The PCA can be computed either by singular value decomposition (SVD) of the data or by eigenvalue decomposition (EVG) of the covariance matrix of data. Therefore, using one of these methods the PCA succeeds to convert the covariance matrix of data into an identity matrix, hence after that process the data would be uncorrelated. The primary use of PCA is for making the data uncorrelated, but can also be used to simplify the computational complexity by making dimensionality reduction in the data. Furthermore, the PCA is used as the step before applying the independent component analysis (ICA) to the data in order to make them uncorrelated before transforming them to independent. More specifically, the dimensionality reduction could be done by keeping the least number of PCs with high information impact by the percentage of useful information (PUI) criterion (e.g. keep the PCs which all together have 95% of useful information).

2.3.2.1 PCA USING EIGENVALUE DECOMPOSITION (EVD)

The eigenvalue decomposition (EVD) (Hyvärine, et al., 2001) transforms the input matrix into an equivalent product using its eigenvalues and eigenvectors under the constraint that the matrix should be diagonalizable (that also means that the matrix should be squared). The aim of PCA is to find the principal components (PCs) of the centered input matrix X which convert the covariance matrix of X into an identity matrix using a linear transformation. Thus:

$$PCs = Y = PX \tag{2.3.1}$$

$$Cy = E\{YY^T\} = I \tag{2.3.2}$$

For simplicity reasons we set the *PCs* equal with *Y*. The PCA wants to find the matrix *P* which transform the matrix X into the matrix Y so as the covariance of Y should be identity matrix. As mentioned before, the eigenvalue decomposition is applied to the covariance matrix of the matrix *X*. Therefore, the covariance matrix of the matrix *X* decomposed into an equivalent product of its diagonal eigenvalues matrix *D* and eigenvectors matrix *E*. Thus:

$$Cx = E\{XX^T\} = EDE^T = ED^{1/2}D^{1/2}E^T = ED^{1/2}ID^{1/2}E^T$$

$$= ED^{1/2}E\{YY^T\}D^{1/2}E^T = (ED^{1/2})E\{YY^T\}\,(ED^{1/2})^T =$$

Assume that the $Z = (ED^{1/2})$

$$Z\,E\{YY^T\}Z^T = E\{ZYY^TZ^T\} = E\{(ZY)(ZY)^T\}$$

$$=> X = ZY => \; Y = Z^{-1}X = \; (ED^{1/2})^{-1}X = \; D^{-1/2}E^{-1}X = PX$$

Thus the matrix *P* is equal:

$$P = \; D^{-1/2}E^{-1} \tag{2.3.3}$$

Due to the fact that the E is orthogonal matrix it is true that $E^{-1} = \; E^T$ so the above equation could be rewritten as:

$$P = D^{-1/2}E^{T} \tag{2.3.4}$$

Finally, the principal components (*PCs*) could be rewritten as:

$$PCs = D^{-1/2}E^{T}X = D^{-1/2}E^{-1}X \tag{2.3.5}$$

As mentioned before the input matrix in eigenvalue decomposition should be squared, otherwise could be applied to the covariance matrix of the input matrix, which is positive semidefinite matrix (a symmetric matrix with positive or zero eigenvalues).

2.3.2.2 PCA USING SINGULAR VALUE DECOMPOSITION (SVD)

The singular value decomposition (SVD) (Jolliffe, 2002) on the centered input matrix X which is non-squared matrix it is a generalization of the eigenvalue decomposition of the covariance matrix of the *X* using a polar decomposition. Therefore, the SVD could be applied to any arbitrary dimension matrix either squared or not. The decomposition of the matrix X with dimensions $m \ x \ n$ (where the n are the samples) can always be as a factorization of three matrices:

$$X = U\Sigma V^{T} \tag{2.3.6}$$

where,

- The columns of the matrix *U* with dimensions *m x m* are the left singular vectors which are orthonormal (orthogonal unit vectors). Also, they are the eigenvector matrix of XX^{T}
- The Σ is a diagonal matrix *m x n* with the non-zero singular values at the diagonal. Additionally, the $\Sigma\Sigma^{T}$ is the diagonal matrix *m x m* with the eigenvalues of XX^{T} and the $\Sigma^{T}\Sigma$ is the diagonal matrix *n x n* with the eigenvalues of $X^{T}X$
- The columns of the matrix *V* with dimensions *n x n* are the right singular vectors which are orthonormal (orthogonal unit vectors). Also, they are the eigenvector matrix of $X^{T}X$
- The matrices XX^{T} and $X^{T}X$ can be computed by $U\Sigma\Sigma^{T}U^{T}$ and $V\Sigma^{T}\Sigma V^{T}$ respectively

The sample covariance matrix *m x m* for the centered matrix *X* is given by $Cx = \frac{1}{n-1}XX^{T}$ (the scale $(1/n - 1)$ reflects the unbiased sample covariance matrix). Thus, the eigenvalues of XX^{T} are obtained from the matrix $\Sigma\Sigma^{T}$ so that the eigenvalues of covariance matrix *Cx* are given by $\frac{1}{n-1}\Sigma\Sigma^{T}$. In analogy to PCA using eigenvalue decomposition we want to make the covariance matrix of *PCs* equal to identity matrix so the *PCs* can be computed as:

$$PCs = \left(\frac{1}{n-1}\Sigma\Sigma^T\right)^{-1/2} U^T X \tag{2.3.7}$$

where, the product U^T with the centered matrix X transform is the polar transformation which make the covariance matrix diagonal as a result makes the data uncorrelated. In addition, we multiply with $\left(\frac{1}{n-1}\Sigma\Sigma^T\right)^{-1/2}$ to make the covariance matrix unity that forces the PCs to have unit variance.

2.3.3 INDEPENDENT COMPONENT ANALYSIS (ICA)

Independent component analysis (ICA) (Hyvärinen & Oja, 2000; Hyvärine, et al., 2001) belongs to the category of blind source separation (BSS) and solves problems like the “cocktail party problem”. For instance, the “cocktail party problem” can be defined as the problem in which songs are recorded from singers who sing simultaneously in the same room and the aim is to separate each song individually by suppressing the others songs. The ICA method taking as input the records from different microphones in the room is able to solve the problem of separation of the songs.

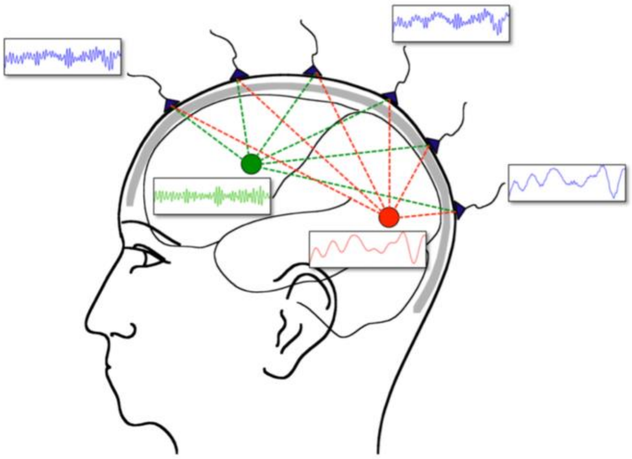

Figure 2. 2: An another example of “cocktail party problem” with sources that are produced by the brain (adapted from www.fieldtriptoolbox.org)

Generally, the ICA method finds the independent components (ICs) that are an estimation of unknown independent sources from an observed multivariate signal. In our case, the observed data *X* are acquired from EEG/MEG signals and produced by unknown brain sources *S*. For the sake of simplicity, we study the ICA method without the parameter of noise. According to the Central Limit Theorem (CLT), the data X tend to have a Gaussian distribution due to the X which are mixed by independent sources S, through an unknown mixing matrix A:

$$X = AS \tag{2.3.8}$$

The dimensions of the above are: $X \epsilon \mathcal{R}^{chs\ x\ samples}$, $A \epsilon \mathcal{R}^{chs\ x\ comps}$ and $S \epsilon \mathcal{R}^{comps\ x\ samples}$, where the chs are the channels from EEG/MEG the comps are the source components and samples are the discrete time points. The ICA method estimates the *ICs* along with an unmixing matrix *W* from the equation:

$$ICs = WX \tag{2.3.9}$$

The dimensions of the above are: $W \epsilon \mathcal{R}^{comps\ x\ chs}$ and $ICs \epsilon \mathcal{R}^{comps\ x\ samples}$. In order to solve the separation of ICs we need to take some assumptions of ICA method into consideration:

1. The X should be a linear combination of statistically independent sources *S* that have either non-Gaussian or at least one Gaussian distribution.
2. The observed data X should be standardized transformed that is unit variance and zero mean and also be whitened (uncorrelated) using the principal component analysis (PCA)
3. The mixing matrix *A* should be full rank.

There are two main methods to solve the ICA problem, either minimization of Mutual Information or maximization of non-Gaussianity. From now on we will concentrate on the latter definition of ICA method using an estimation of Kurtosis (fourth central moment) which is High-Order Statistics (HOS). The first step of ICA is to make X have zero mean and unit variance in order to make the data comparable. The second step is to make data uncorrelated removing dependences up to second order (making covariance matrix unit). In parallel with whitening the PCA allows dimensionality reduction for computational reasons (keeping in mind the assumption three).The last step is to remove high-order dependencies e.g. using kurtosis, entropy or mutual information. To isolate the number of sources (comps) we should have the same or a bigger number of channels (chs) for that reason the mixing matrix A should be full rank (chs >= comps). Otherwise, if there are fewer channels that sources the separation cannot isolate each source individually. As a last comment, notice that if A and B are independent then they are also uncorrelated, but the opposite does is not always valid.

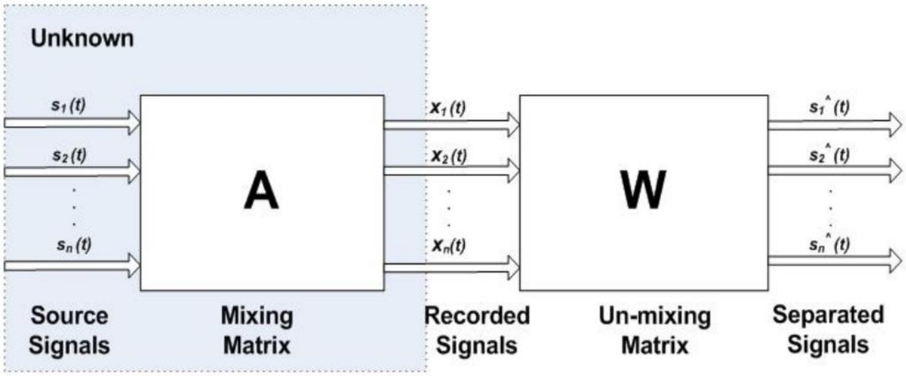

Figure 2. 3: This illustration shows how the way of acquisition of the estimation sources (adapted from Ganesh R. Naik and Dinesh K Kumar, 2009)

2.3.3.1 Kurtosis

The kurtosis (the fourth standardized moment) (Hyvärine, et al., 2001) is a measure that describes the curvature of a probability distribution. The definition of the kth central moments of a random variable X is $\mu_k = E[(X - E[X])^k]$, for $k \geq 0$. The mathematical expression of kurtosis is:

$$kurtosis(X) = E\left[\left(\frac{X - \mu}{\sigma}\right)^4\right] = \frac{E[(X - \mu)^4]}{(E[(X - \mu)^2])^2} = \frac{\mu_4}{(\mu_2)^2} = \frac{\mu_4}{(\sigma)^2} \quad (2.3.10)$$

If the data X is zero-mean and whitened ($\mu = 0$ and $\sigma = 1$) then:

$$kurtosis(X) = E[X^4] \quad (2.3.11)$$

Any Gaussian distribution with unit variance has kurtosis equal to 3. Alternatively, we can modify the expression of the kurtosis when it is equal with zero to give Gaussian distribution. That is the definition of the excess kurtosis which is *kurtosis(X) – 3*. Thus, it is easy to distinguish in three categories:

- Leptokurtic or super-Gaussian distribution has *kurtosis(X) – 3 > 0*. The super-Gaussian distributions have more sharp peaks compare with the Gaussian distribution.
- Mesokurtic or Gaussian distribution has *kurtosis(X) – 3 = 0.*
- Platykurtic or sub-Gaussian distribution has *kurtosis(X) – 3 < 0.* The sub-Gaussian distributions are more flat compare with the Gaussian distribution.

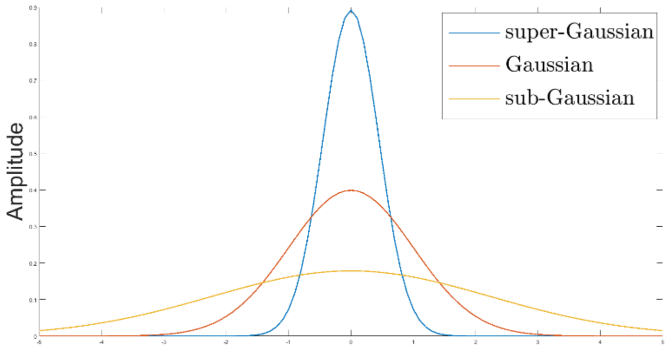

Figure 2. 4: The three categories of curves of Gaussian distribution (super-Gaussian, Gaussian, sub-Gaussian)

Additional properties of kurtosis are:

- Additivity: For two statistical independent random variables x and y it is true that

$$kurtosis(x+y) = kurtosis(x) + kurtosis(y) \tag{2.3.12}$$

- Scalar multiplication the random variable x

$$kurtosis(\alpha x) = a^4 kurtosis(x) \tag{2.3.13}$$

To sum up, kurtosis is an easy way which can bring out the non-Gaussianity of a random variables or a signal. The distribution of X is not Gaussian if $kurtosis(X) - 3 \neq 0$. The ICA disentangles the non-Gaussian independent sources by the unmixing matrix W from their mixtures that has Gaussian distribution form the central limit theorem.

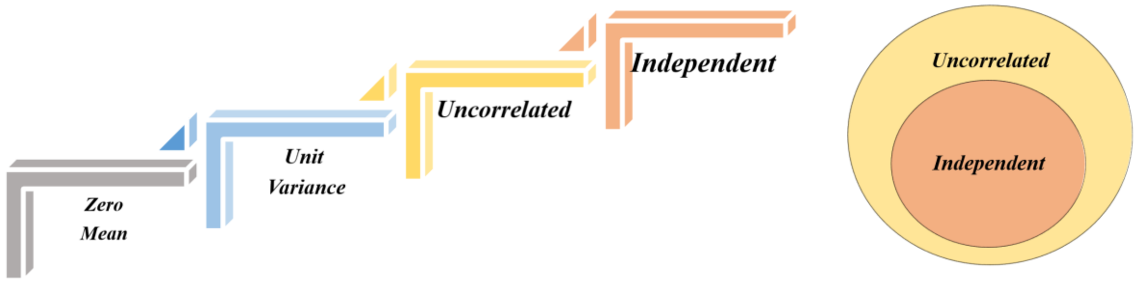

a) b)

Figure 2. 5: a) The steps for succeed the independence in data and b) If the data are independent, this means that are also uncorrelated but the opposite is not the case.

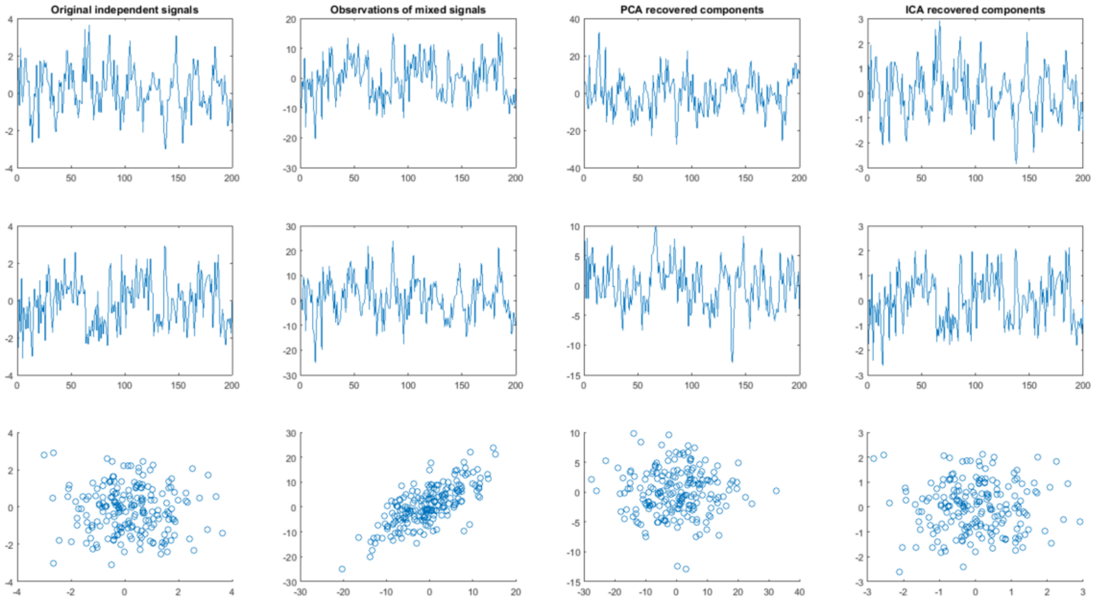

Figure 2. 6: This figure illustrate the comparison between PCA and ICA. Additional, it shows that ICA can estimates the independent sources

2.3.4 Functional Source Separation (FSS)

In this work, we apply the algorithm of Functional Source Separation (FSS) (Barbati, et al., 2006; Porcaro, et al., 2013), which is a variation of Independent Component Analysis (ICA) method with a priori information revealing the specific function features of data. Since the FSS method uses a priori knowledge, it is a semi-Blind Source Separation (semi-BSS) method. The FSS operates similarly to ICA and takes as input the observed data X (viewed as a linear combination of the sources S via the mixing matrix A). The difference is that the FSS isolates each source separately, one each time, starting every time from observed data X. The estimation of the k^{th} source is the k^{th} functional source FS_k and is achieved by finding the unmixing vector w from the optimization of the cost function of FSS by means of simulated annealing (*SA*). In this case, we obtain an unmixing vector instead of matrix because the FSS extracts one component at a time. Hence, the estimation of FS_k is given by the equation:

$$FS_k = w^T X \qquad (2.3.14)$$

As mentioned before, the unmixing vector w is found by the optimization of a cost function of FSS:

$$F = J + \lambda R_{FSk} \qquad (2.3.15)$$

where *J* is the function that ICA uses to find the unmixing matrix W; in our case is the estimation for the kurtosis used by the fastICA algorithm (Hyvärine, et al., 2001; Hyvärinen & Oja, 2000). The term R_{FSk} is the a priori information of the k^{th} source and λ is a weight constant that is chosen to maximize the influence of the R_{FSk} while minimizing the computational time. The R_{FSk} enhances the uniqueness of the each source in the cost function F and is defined for the k^{th} source as:

$$R_{FSk} = \sum_{t_k - \Delta 1 t_k}^{t_k + \Delta 2 t_k} |EA(t)| - \sum_{\alpha}^{\beta} |EA(t)| \tag{2.3.16}$$

where the evoked activity *EA* is computed by averaging signal trials of the source FSk, t_k is the time point with the maximum potential of the k^{th} source, the time points $\Delta 1 t_k$ and $\Delta 2 t_k$ denote the 50% of this maximum potential before and after t_k and the baseline (no response) reflects from the time interval α to β. The second sum can be skipped if the baseline correction has been applied at EA. Furthermore, the orthogonality constraint is not essential for the FSS, because it does not separate all the sources in one run but rather extracts each FS_k separately starting from observed data *X* and amplifying the characteristics of the k^{th} source.

2.3.4.1 SIMULATED ANNEALING (SA)

The simulated annealing (*SA*) (Kirkpatrick, et al., 1983; Naik & Wang, 2014) is an algorithm which implements global optimization (minimum or maximum) for a given function. In this section we will consider the SA as a global minimum optimization scheme (the global maximum optimization is almost the same procedure). The name of SA is inspired by annealing in metallurgy. The annealing is a heat treatment technique which changes the properties of the material. Firstly, the metal is heated until arriving to a maximum temperature in which it is possible to make the recrystallization. As a result, the metal from a hard and rigid material becomes softer and increases its ductility. Also, with this process some imperfections of the material could be repaired, such as crystal defects etc. Then the cooling process takes place, in which the annealing changes it in a slow way until the new state of the material reaches a more stable state of lower energy. At the end of this procedure, the material is more easily manageable by the blacksmith for further processing. The aim of SA in terms of physics is to find the state of lower energy and if it manages to achieve this, then it has reached the desirable global minimum. The SA is an iterative algorithm starting from a high initial temperature *T* (that makes possible the recrystallization) and a random starting state k with an energy E_k. For each iteration the algorithm computes the energy for the new state j and takes the difference with the energy of the previous state i. Therefore, the difference is defined as $\Delta E = E_j - E_i$. The new state j is accepted if it has $\Delta E < 0$ which means that state j has lower energy and the algorithm is driven to a minimum. Otherwise, if the difference is $\Delta E > 0$ then the energy E_j is bigger from the E_i and the algorithm does not be driven to converge to a minimum. However, instead of rejecting this state the SA could accept it with uncertainly, using a probability function defined as:

$$P_{ij} = e^{-\frac{\Delta E}{kT}} \tag{2.3.17}$$

where k is the Boltzmann constant. Thus, for each iteration with $\Delta E > 0$ the SA compare the P_{ij} with a random number from a uniform distribution $U(0,1)$. If the P_{ij} is greater than the random uniform number then the SA accepts the state j as the new one, else it stays in the previous state i. This procedure is useful to prevent a situation like the algorithm is stuck in a state with a local optimum in high temperatures T, that do not represent the state with low energy. For instance, in the high temperatures T the probability P_{ij} tend to have values near to one ($e^0 = 1$) so that more frequently the SA will accept the new state with high energy to avoid staying in a state with low topical energy. Alternatively, if the temperatures T are low then the probability P_{ij} tend to have values near to zero ($e^{-\infty} = 0$) so it becomes very difficult to choose a state like this, implying that the algorithm is near to global minimum and now the transitions is more critical. An important issue with the correct operation of the algorithm is to cool slowly, namely the changes of T should be done with appropriate small steps. If the steps are too big, the algorithm could consider a local minimum as a global. Otherwise, if the steps are too small then the algorithm would need a lot of computational time to reach convergence. This shows us that the changes of T should be done wisely. As outlined above the FSS computes the unmixing vector w by the optimization of the cost function F for each component separately. The SA enables such form of optimization in FSS and takes as input the cost function $F(w)$. Furthermore, it starts from initial random normalized vector w until it converges to an optimal w_{opt}. The procedure of cooling is done by a factor α (in our case we set the $\alpha = 0.8$). Accordingly, for each iteration of the algorithm we choose the new temperature T as α times smaller form the previous one, starting from an initial high temperature. Finally, the SA terminates when it reaches a stopping temperature that is chosen to balance between finding an approximation of global minimum and converging in a reasonable time. It is notable to mention that because of the nature of algorithm to seek for an approximation of the global optimum, it is possible to have small changes of the FS_k at equilibrium among different runs.

2.4 SOURCE ANALYSIS

2.4.1 EQUIVALENT CURRENT DIPOLE

Initially, it is important to mention the definition of equivalent current dipole (ECD) (Hämäläinen, et al., 1993; Hallez, et al., 2007) which is defined as a strong current dipole that represents the synchronous electrical activity of a large amount of neurons which are localized in a small area. These strong activities could be acquired by recording machines (e.g. EEG, MEG). Let us assume that the ECD Q is defined mathematically for a time instant with the following parameters: position r_Q, magnitude d_Q and orientation $\vec{e}_Q$, the last two parameters form the dipole moment $\boldsymbol{m_Q} = d_Q\vec{e}_Q$. The position r_Q is usually chosen as the half distance l between the sink and the source of ECD. The monopoles (source and sink) have absolute electrical charges equal to q. The magnitude at one time instant is $d_Q = ql$ in Cm. The unit vector $\vec{e}_Q$ gives the direction of the dipole (from sink to source). Additionally, the dipole Q could be decomposed in three dimensional Cartesian axes, like three dipoles in the same position of Q and each dipole has magnitude equal to the orthogonal projection on the respective axis:

$$\boldsymbol{m_Q} = d_x\vec{e}_x + d_y\vec{e}_y + d_z\vec{e}_z \tag{2.4.1}$$

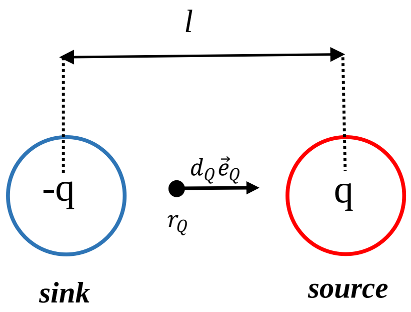

Figure 2. 7: The dipole moment for a time instant.

Furthermore, in time the ECD approximates the primary current $\mathbf{I}_{pr} = dq/dt$ that flows in a volume across distance l from sink to source. For one position r_Q defines the primary current density $\boldsymbol{J_Q^{pr}}(r_Q)$ caused by the synchronous electrical activity of neurons. Thus, the primary current density $\boldsymbol{J_Q^{pr}}$ is defined as:

$$\boldsymbol{J_Q^{pr}}(r_Q) = \mathbf{I}_{pr} l \delta(r - r_Q) \tag{2.4.2}$$

where the $\delta(r)$ is the Dirac function and the current density has unit A/m^2.

2.4.2 INTRODUCTION OF SOURCE ANALYSIS

The goal of the source localization problem is to find the parameters of an unknown source (position and dipole moment), which produces an electrical activity inside the brain from the observed data (EEG or MEG or combined EMEG). The source localization problem is divided in two main tasks: the forward and the inverse problem. The forward problem (Hallez, et al., 2007) finds an estimation of the observed measurement (electric potential or magnetic field) in all channels for each possible source (dipole), through a head model which is a simulation of the human head. These sources are located in the source space (or source model) which include all candidate positions inside the brain where the sources could be located (e.g. gray matter). Generally, a source is determined according to the position and moment (amplitude and orientation). As mentioned above, each source corresponds to one known position at the source space and that position is expressed in Cartesian coordinate system. Thereby, in order to determine a source in a certain location inside a volume in Cartesian coordinate system, only the three parameters of amplitude are needed because the orientation is known $\{\vec{e}_x, \vec{e}_y, \vec{e}_z\}$. For simplicity reasons, we assume that the source is determined by one amplitude and one orientation. Thus, the i dipole has dipole moment $m_i = d_i \vec{e}_i$ instead of $m_i = [d_{ix}\vec{e}_x \ \ d_{iy}\vec{e}_y \ \ d_{iz}\vec{e}_z]^T, \forall\, dipole/position \ \ i = 1 \ldots k$ and k is the number of locations in the source space (the number of dipoles is equal to the number of positions). It is time to introduce the lead-field matrix L (or gain matrix G) that represents how each source gives its estimation of the observed measurement. The simple mathematical equation without noise is:

$$X_{est} = LS \tag{2.4.3}$$

where the observed measurement $X_{est} \in \mathcal{R}^{chs\ x\ samples}$, the lead-field matrix $L \in \mathcal{R}^{chs\ x\ q}$, the magnitude of the sources (dipoles) $S \in \mathcal{R}^{q\ x\ samples}$ and $q = k$ (in Cartesian coordinate system the $q \in \mathcal{R}^{3\ x\ k}$). For instance, for N channels, k dipoles and one sample:

$$X_{est} = \begin{bmatrix} X_{est}(r_1) \\ \vdots \\ X_{est}(r_N) \end{bmatrix} = \begin{bmatrix} l(r_1, r_{sour1}) & \cdots & l(r_1, r_{sourk}) \\ \vdots & \ddots & \vdots \\ l(r_N, r_{sour1}) & \cdots & l(r_N, r_{sourk}) \end{bmatrix} \begin{bmatrix} d_1\vec{e}_1 \\ \vdots \\ d_k\vec{e}_k \end{bmatrix} \tag{2.4.4}$$

where $r_1 \cdots r_N$ are the positions of the channels and $r_{sour1} \cdots r_{sourk}$ are the positions of the dipoles inside the brain. In order to solve the forward problem and find the lead-field matrix, the head model, the source space and the channel (electrodes or sensors) positions are needed. These requirements should be registered in the same coordinate system (e.g. fiducial points) with the same units. Also, the MEG forward problem is solved by the solution of EEG forward problem as an integration. The inverse problem takes as input the lead-field matrix L from the forward solution and the original observed data (from EEG/MEG/EMEG) and it finds the unknown source(s).

$$S = L^{-1} X_{orig} \tag{2.4.5}$$

where the X are the original data $X_{orig} \in \mathcal{R}^{chs\ x\ samples}$. In general, in real life we cannot eliminate the factor of noise, so the forward equation is:

$$X_{est} = LS + n \tag{2.4.6}$$

As a result, the inverse solution finds an estimation of the source(s):

$$\hat{S} = L^{-1} X_{orig} \tag{2.4.7}$$

The inverse problem (Grech, et al., 2008) is an ill-posed problem because the same data measurement could be satisfied by different solutions (since the number of the sources is much greater than the number of channels, sources $\gg$ chs). There are two main categories of methods to solve the ill-posed inverse problem: parametric and non-parametric. For the former, we assume a few number of sources to limit the ill-posed problem. Also, the parametric techniques estimate the dipole position and moment. Because of the position estimation, the problem becomes non-linear. An example of parametric technique is the Beamforming. On the other hand, the latter estimates the source(s) moment in a predetermined source space and this is a linear problem, techniques such as MNE, LORETA, sLORETA. In addition, in this category a regularization method is used to approximate the ill-posed problem as well-posed. From now on, we will deal with non-parametric methods.

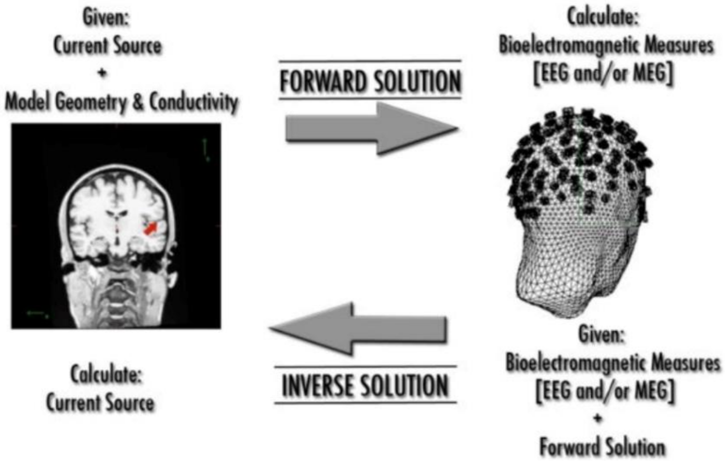

Figure 2. 8: The correlation between Forward and Inverse solutions (adapted from Bangera, 2008)

2.4.3 FORWARD PROBLEM

2.4.3.1 MATHEMATICAL BACKGROUND FOR THE FORWARD PROBLEM

- The vector field (vector-valued function) in a three-dimensional space $\Re^3$ is defined as $\vec{a}(x,y,z) = a_x\vec{e}_x + a_y\vec{e}_y + a_z\vec{e}_z = \boldsymbol{A}$, the $\{\vec{e}_x, \vec{e}_y, \vec{e}_z\}$ are the unit vectors of Cartesian axes and the $\vec{a}$ is composed by the functions for each axis $\{a_x(x,y,z), a_y(x,y,z), a_z(x,y,z)\}$.
- The del or nabla ∇ operator is defined as:

$$\nabla = \left[\frac{\partial}{\partial x}\vec{e}_x + \frac{\partial}{\partial y}\vec{e}_y + \frac{\partial}{\partial z}\vec{e}_z\right] \tag{2.4.8}$$

- <u>For a scalar field</u> (scalar function) $f(\vec{r}) = f(x,y,z)$:
  - The gradient of f <u>is a vector filed</u>. At a point, the direction of the gradient vector shows where the function f is increasing and the magnitude how rapidly it is increasing. It is defined as:

$$grand(f) = \nabla f = \frac{\partial f}{\partial x}\vec{e}_x + \frac{\partial f}{\partial y}\vec{e}_y + \frac{\partial f}{\partial z}\vec{e}_z \tag{2.4.9}$$

- <u>For a vector field</u> $\vec{a}(x,y,z) = \boldsymbol{A}$:
  - The divergence of $\vec{a}$ <u>is a scalar field</u>. The divergence of a vector field at a particular point shows how the flow interacts (if it is steady, goes in or out, then the corresponding value for the divergence is zero, positive and

negative) with a closed infinitesimal volume around this point. If a vector field has zero divergence, then it is called solenoid. It is defined as:

$$div(\vec{a}) = \nabla \cdot \vec{a} = \nabla \cdot \boldsymbol{A} = \frac{\partial a_x}{\partial x} + \frac{\partial a_y}{\partial y} + \frac{\partial a_z}{\partial z} \qquad (2.4.10)$$

- The curl of $\vec{a}$ <u>is a vector field</u>. The curl denotes for each point if the vector field has vortex. If it has, then the curl denotes the strength (by the magnitude of the curl vector) and the rotation (clockwise or not by the orientation of the curl vector) of the vortex. The curl is a vector perpendicular to the plane of the vortex. If a vector field has zero curl, then it is called irrotational. It is defined as:

$$curl(\vec{a}) = \nabla \times \vec{a} = \nabla \times \boldsymbol{A} = \begin{vmatrix} \vec{e}_x & \vec{e}_y & \vec{e}_z \\ \frac{\partial}{\partial x} & \frac{\partial}{\partial y} & \frac{\partial}{\partial z} \\ a_x & a_y & a_z \end{vmatrix} \qquad (2.4.11)$$
$$= \left(\frac{\partial a_z}{\partial y} - \frac{\partial a_y}{\partial z}\right)\vec{e}_x + \left(\frac{\partial a_x}{\partial z} - \frac{\partial a_z}{\partial x}\right)\vec{e}_y + \left(\frac{\partial a_y}{\partial x} - \frac{\partial a_x}{\partial y}\right)\vec{e}_z$$

The electromagnetic field is the combination of the electric field $\boldsymbol{E}$ in V/m^2 and the magnetic field $\boldsymbol{B}$ in Tesla and it can be computed by the Maxwell's equations and the continuity equation (Hämäläinen, et al., 1993).

Maxwell's equations:

$$\nabla \cdot \boldsymbol{E} = \rho/\varepsilon \qquad (2.4.12)$$

$$\nabla \times \boldsymbol{E} = -\partial \boldsymbol{B}/\partial t \qquad (2.4.13)$$

$$\nabla \cdot \boldsymbol{B} = 0 \qquad (2.4.14)$$

$$\nabla \times \boldsymbol{B} = \mu(\boldsymbol{J} + \varepsilon\, \partial \boldsymbol{E}/\partial t) \qquad (2.4.15)$$

Continuity equation:

$$\nabla \cdot \boldsymbol{J} = -\partial \rho/\partial t \qquad (2.4.16)$$

where ρ is the volume charge density in C/m^3, J is the current density in A/m^2 , μ is magnetic permeability in H/m and ε is the electrical permittivity of the medium in F/m.

Also, the Maxwell's equations and the continuity equation can be simplified with these two assumptions:

- The first notation is that the magnetic permeability μ for the human tissues is equal to vacuum permeability μ_0.
- The second is the omission of the time derivatives $\partial \boldsymbol{E}/\partial t$, $\partial \boldsymbol{B}/\partial t$ and $\partial \rho/\partial t$ in the above equations using the quasi-static approximation.

The electromagnetic field in the human brain has a small range of frequencies below 1 kHz in conjunction with the analysis interval, which has short duration of some ms. Therefore, we can apply quasi-static approximation in Maxwell's equations. As a result, the time-derivatives are small compared to passive Ohmic current, so they can be neglected (i.e. $|\varepsilon\, \partial \boldsymbol{E}/\partial t| \ll |\sigma \boldsymbol{E}|$ equivalent to $2\pi f \varepsilon/\sigma \ll 1$, because the human brain produces low frequencies, the latter equation is valid and we take into account the quasi-static approximation) (Larsson, 2007). The current density $\boldsymbol{J}$ is divided into primary current density $\boldsymbol{J}^{\boldsymbol{pr}}$ and the passive (or secondary) current density $\boldsymbol{J}^{\boldsymbol{pas}} = \sigma \boldsymbol{E}$, σ is the conductivity of the medium. The primary current density $\boldsymbol{J}^{\boldsymbol{pr}}$ represents the electrical activity of the neurons (source) in the brain and every other current activity is produced by the passive current induced by the electric field $\boldsymbol{E}$. Thus,

$$\boldsymbol{J} = \boldsymbol{J}^{\boldsymbol{pr}} + \sigma \boldsymbol{E} \;\; => \;\; \nabla \cdot \boldsymbol{J} = \nabla \cdot \boldsymbol{J}^{\boldsymbol{pr}} + \sigma \nabla \cdot \boldsymbol{E} \qquad (2.4.17)$$

From the quasi-static approximation, the continuity equation $\nabla \cdot \boldsymbol{J} = 0$. This means that there is no current leakage of the brain source because it is composed by a current source and a sink in an infinitely small space (assume a node). Therefore, divergence current source density in such small enclosed volume is equal to zero (Hämäläinen, et al., 1993; Hallez, et al., 2007). This way, the above equation becomes:

$$\nabla \cdot \boldsymbol{J}^{\boldsymbol{pr}} = -\, \sigma \nabla \cdot \boldsymbol{E} \qquad (2.4.18)$$

Due to the fact that the curl of the electric field is $\boldsymbol{E}$ zero ($\nabla \times \boldsymbol{E} = 0$) from the quasi-static approximation, this leads to express the electric field $\boldsymbol{E}$ with the gradient of potential field $\boldsymbol{V}$ as:

$$\boldsymbol{E} = -\nabla V \qquad (2.4.19)$$

Hence, we combine the equations (2.4.18 and 2.4.19):

$$\nabla \cdot \boldsymbol{J}^{\boldsymbol{pr}} = \nabla \cdot \big(\sigma(\nabla V)\big) \qquad (2.4.20)$$

The above equation could be solved for the potential field if the primary current source density and the conductivity are known. The solution can be analytic or numerical depending of the complexity of the head model. Also, the magnetic field $\boldsymbol{B}$ could be readily computed if the V is known by the Biot-Savart law (Hämäläinen, et al., 1993; Vallaghé, 2008):

$$\boldsymbol{B}(\boldsymbol{r}) = \frac{\mu_0}{4\pi}\int_{\mathfrak{R}^3} \boldsymbol{J}(\boldsymbol{r}') \times \frac{(\boldsymbol{r}-\boldsymbol{r}')}{\|\boldsymbol{r}-\boldsymbol{r}'\|^3} dr' \qquad (2.4.21)$$

in correspondence with $\boldsymbol{J} = \boldsymbol{J}^{\boldsymbol{pr}} + \boldsymbol{J}^{\boldsymbol{pas}} = \boldsymbol{J}^{\boldsymbol{pr}} - \sigma(\nabla V)$ the magnetic field is divided as:

$$\boldsymbol{B}(\boldsymbol{r}) = \boldsymbol{B}^{\boldsymbol{pr}}(\boldsymbol{r}) + \boldsymbol{B}^{\boldsymbol{pas}}(\boldsymbol{r})$$

$$= \frac{\mu_0}{4\pi}\int_{\mathfrak{R}^3} \boldsymbol{J}^{\boldsymbol{pr}}(\boldsymbol{r}') \times \frac{(\boldsymbol{r}-\boldsymbol{r}')}{\|\boldsymbol{r}-\boldsymbol{r}'\|^3} dr' - \frac{\mu_0}{4\pi}\int_{\mathfrak{R}^3} \sigma(\nabla V(\boldsymbol{r}')) \times \frac{(\boldsymbol{r}-\boldsymbol{r}')}{\|\boldsymbol{r}-\boldsymbol{r}'\|^3} dr' \qquad (2.4.22)$$

The $\boldsymbol{B}(\boldsymbol{r})$ is the magnetic field outside of the brain at the point of measurement $\boldsymbol{r}$ which is produced by the primary current with current density $\boldsymbol{J}(\boldsymbol{r}')$ at the point $\boldsymbol{r}'$ inside the brain. Additionally, the passive magnetic field is produced by the passive current.

2.4.3.2 CONDUCTIVITY

The Ohm's law links the electric field $\boldsymbol{E}$ with the passive current density $\boldsymbol{J}^{\boldsymbol{pas}}$ and the conductivity σ:

$$\boldsymbol{J}^{\boldsymbol{pas}} = \sigma\boldsymbol{E} \qquad (2.4.23)$$

Recent studies divide human head compartments in two categories depending on their conductivity σ: isotropic and anisotropic compartments. In the former category, the current flow passes through with the same effort in every direction in the volume; the compartments modeled as isotropic are the scalp, the cerebrospinal fluid (CSF) and the gray matter. Alternatively, in the latter category some directions facilitate the pass of the current flow easier than others, reflecting different conductivity properties across different directions; compartments modeled like this are the skull and the white matter. The skull is divided in three layers, two hard layers with low conductivity and a spongiform layer inside them, which is more conductive. The anisotropy of white matter is influenced by the directions of the different type nerve fibers (projection, association and commissural fibers Figure 1. 10). Additionally, the conductivity along the nerve bundle inside the white matter is larger than in the perpendicular direction. The conductivity σ for isotropic volume for each position r has the same scalar value. By contrast, the anisotropic volume in each position r is a directional matrix $\sigma(r) \in \mathfrak{R}^{3\times 3}$ (Wolters, et al., 2006; Hallez, et al., 2007).

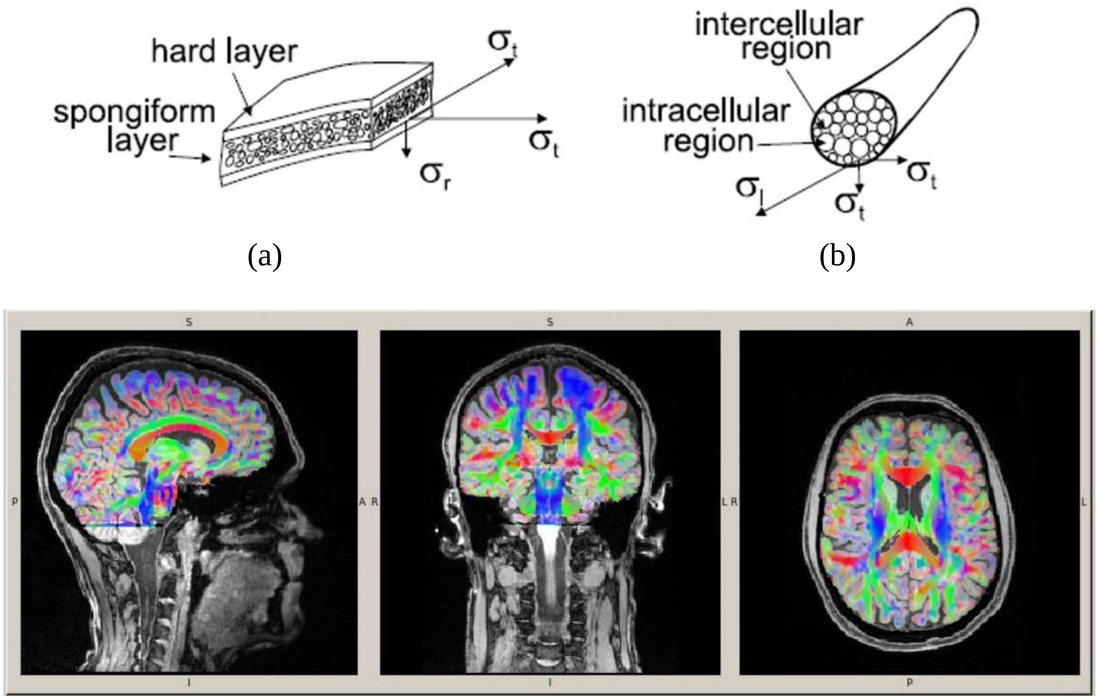

(a) (b)

(c)

Figure 2. 9: The anisotropy properties of the conductivity of skull and white matter. (a) The three layers of the skull (hard-spongiform-hard). The conductivity along the σ_t spongiform layer is 10 times bigger than the perpendicular σ_r. The anisotropy of the white matter is illustrate at figures (b) and (c). The (b) shows the conductivity inside the nerve fiber that consists of bundles of axons and the conductivity σ_l along to the bundles is 9 times bigger than the perpendicular direction σ_t. At (c) the colors indicates the primary fiber orientation (red: left-right, green: anterior-posterior and blue superior-inferior). Source: (a,b are adapted from (Hallez, et al., 2007) and c is adapted from https://www.baci-conference.com, http://www.sci.utah.edu/~wolters/PaperWolters/2017/AntonakakisTalkBACI2017.pdf).

2.4.3.3 BOUNDARY CONDITIONS

There are two boundary conditions for the interface between two compartments. The first is the continuity of current density, according to which, all the current that leaves one compartment is equal to the current that injects to the other. There is an exception if the outsider compartment is the air, for which the current is equal to zero (Neumann boundary condition). The second is the continuity of potential, according to which, the potential that passes through the interface between two non-air compartments stays steady (Dirichlet boundary condition). Mathematically, the above conditions can be expressed as (Hallez, et al., 2007):

- Two compartments with conductivities σ_1 and σ_2:

$$\boldsymbol{J_1} e_n = \boldsymbol{J_2} e_n \Rightarrow \sigma_1(\nabla V_1) = \sigma_2(\nabla V_2) \tag{2.4.24}$$

$$V_1 = V_2 \tag{2.4.25}$$

- One compartment with conductivity σ_1 connected with air:

$$\boldsymbol{J_1} e_n = 0 \Rightarrow \sigma_1(\nabla V_1) = 0 \tag{2.4.26}$$

where the e_n is the outward unit normal to the surface of interface at some n direction.

2.4.3.4 HEAD VOLUME CONDUCTOR MODELS

The head volume conductor model is a simulation of the shape (geometrical features) and the conductivity (electrical features) of each different part of the human head (e.g. scalp, skull, brain etc.). The varieties of head models could be divided into two distinguished categories, simple head models and realistic head models. The former category includes models like a single homogeneous sphere and a multi-sphere head model. As the name suggests, these models are simple and fast but they do not have good accuracy because they take a coarse shape of the head that is not representative of a real one. The latter category consists of head models that can be solved by boundary element method (BEM) and finite element method (FEM), which are more computationally complex and expensive but they prevail over accuracy. The anatomical characteristics of the human head for the realistic head model could be acquired by magnetic resonance image (MRI) data.

2.4.3.4.1 SPHERICAL HEAD MODEL

The first attempt to simulate the head was a homogeneous sphere (Frank, 1952; Hallez, et al., 2007) but soon that implementation was abandoned. The reason for that was that researchers realized that they needed a structure more complex than a simple homogeneous sphere, due to the fact that there is a significant difference of conductivity values in the skull in comparison with the brain and the scalp. As a consequence, they started using an isotropic multi-sphere model which started with three concentric spheres for the different conductivities of brain, skull, scalp and proceeded to more complex structures with some additional four and five spheres models. In the three spheres model, the outer layer represents the scalp, the intermediate layer represents the skull and the inner sphere represents the brain. Additionally, some implementations use four or five spheres models. The four spheres model has the extra cerebrospinal fluid (CSF) layer which is located between the brain sphere and the skull layer. Finally, the 5 layers spheres model divides the brain sphere into two layers, the gray and white matter. The spherical head models use a semi-analytical expression in order to solve the forward problem.

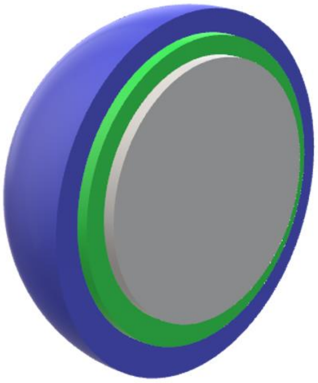

Figure 2. 10: The three concentric spherical head model, from the outer layer to the inside sphere the compartments represent the scalp, the skull and the brain.

As mentioned before, the spherical head models enable simple and fast methods. On the other hand, they do not represent the real anatomic characteristics of the head and they do not take into consideration the anisotropy of the skull and the white matter, yielding significant errors in modeling accuracy. Therefore, modern studies prefer the realistic head models for deriving more accurate results.

2.4.3.4.2 BOUNDARY ELEMENT METHOD (BEM)

The boundary element method (BEM) (Hallez, et al., 2007) uses a numerical approximation in order to solve the forward problem with a boundary limitation. First, let us consider the case of a frequently used BEM, which is the head model with three compartments (scalp, skull, brain). For each compartment, an outer enclosed surface of its shape will be created by various triangular shapes (boundary elements). These surfaces will function as interfaces between the different compartments conductivities (air-scalp, scalp-skull and skull-brain). For each center of the triangles, the electric potential difference is calculated between the two compartments. This potential difference is produced by a source inside the brain. Each compartment is a homogeneous and isotropic volume conductor. The homogeneous condition implies that the conductivity is identical in every location of the volume. The isotropic condition holds when the current flows the same way in every direction (i.e. the current flow in each direction is passed through the same conductivity or conductivities). This could be an important limitation in brain conductivity, because it does not represent a realistic phenomenon. For instance, the anisotropy of the different conductivities in the layers of skull and the anisotropy of white matter make the current flow to be highly dependent on the direction due to the different conductivities. However, the benefit of BEM is that it does not have high computational cost due to the fact that it does not simulate the inner part of each compartment. Moreover, the BEM model produces a more realistic geometry in comparison with the multi-sphere model.

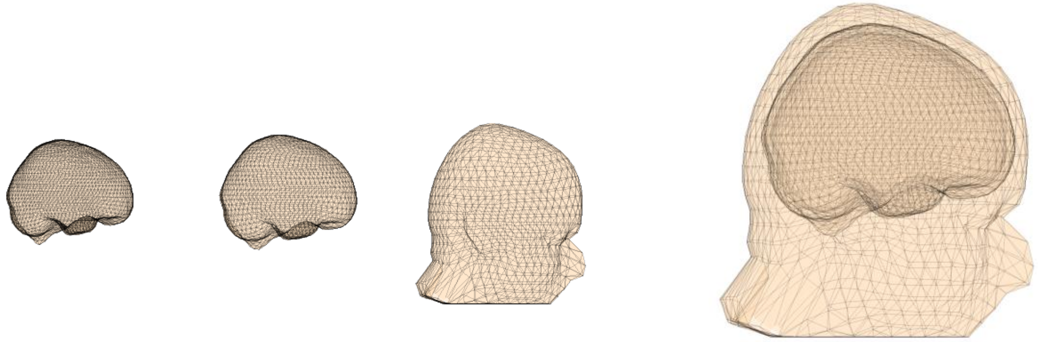

(a) (b)

Figure 2. 11: Boundary Element Method (BEM) with three compartments which is produced via the fieldtrip toolbox. a) From left to right, the separate compartments are the brain, the skull and the scalp. b) All compartments together.

2.4.3.4.3 FINITE ELEMENT METHOD (FEM)

The finite element method (FEM) (Wolters, et al., 2006; Hallez, et al., 2007; Rullmann, et al., 2009; Aydin, et al., 2014; Vorwerk, et al., 2019) is also a numerical approximation in order to solve the forward problem. In contrast to BEM, this method models the inner volume with finite elements, usually in the form of tetrahedrons. In such model, the points in which the potential is calculated are the vertices of the tetrahedrons. By using finite elements, we can also model the anisotropy of skull and white matter for more realistic results. Furthermore, the method can reach spatial accuracy up to 1 mm. The compartments which are modeled are the scalp, the skull compacta, the skull spongiosa, the CSF, the gray and the white matter. The primary drawback of FEM in comparison to other models can relate to the computational cost, which nowadays does not pose a serious concern. In conclusion, the FEM model represents the head in more realistic representations with high resolution. The implementation of FEM has high impact at the subsequent source localization of EEG and MEG signals and for this reason it is highly preferred.

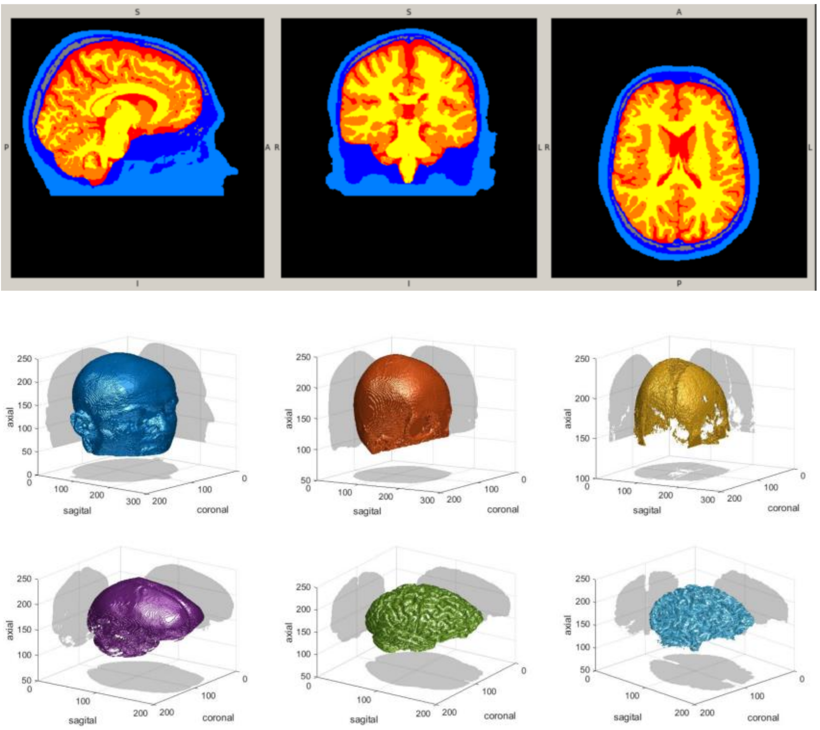

Figure 2. 12 : The realistic head model that is produced by FEM, from left to right the figure show: the above figures show: the head model in sagittal, coronal and axial, the middle figures show: the scalp, skull compacta and skull spongiosa, the below figures show: CSF, gray and white matter. Adapted from www.baci-conference.com/, www.sci.utah.edu/~wolters/PaperWolters/2017/ AntonakakisTalkBACI2017.pdf)

2.4.4 INVERSE PROBLEM

2.4.4.1 MATHEMATICAL BACKGROUND FOR THE INVERSE PROBLEM

The measurement data X_{orig} (from EEG,MEG or EMEG) which are produced by the unknown source(s) S are related in a linear form as:

$$X_{orig} = LS + n \qquad (2.4.27)$$

Because of the noise from a Bayesian approach (Grech, et al., 2008; Lucka, et al., 2012), we consider X_{org} and S as random variables and we model the noise as zero-mean Gaussian random variable $n \sim N(0, \sigma^2 \mathrm{I}_{chs})$, where σ is the standard divination of Gaussian noise and I_{chs} is the identity matrix. The likelihood density is the conditional probability density of X_{org} given S, thus:

$$p_{li}(x|s) = \left(\frac{1}{2\pi\sigma^2}\right)^{\frac{chs}{2}} \exp\left(-\frac{1}{2\sigma^2}\|x - Ls\|_2^2\right) \tag{2.4.28}$$

But in order to take the estimation of the source(s) $\hat{S}$, we need to find the conditional density of S given X_{org}, which is called posterior density $p_{post}(s|x)$. Also, before such a derivation we should define the a priori information for the source S, which is called prior $p_{pr}(s)$. Then, from Bayes' rule:

$$p_{post}(s|x) = \frac{p_{li}(x|s)p_{pr}(s)}{p(x)} \tag{2.4.29}$$

The $p(x)$ is the model evidence and for our purpose it does not play an important role and operates as a normalizing constant. We can mention two different choices to find out the estimation of the source(s) $\hat{S}$, the maximum a posteriori estimate (*MAP*) and the conditional mean estimate (*CM*):

$$\hat{S}_{MAP} := \underset{S}{\operatorname{argmax}}\, p_{post}(s|x) \tag{2.4.30}$$

$$\hat{S}_{CM} := E[s|x] = \int s\, p_{post}(s|x)\, ds \tag{2.4.31}$$

Let us consider the priors as Gibbs distribution:

$$p_{pr}(s) \propto \exp\left(-\frac{\lambda}{2\sigma^2}\mathcal{P}(s)\right) \tag{2.4.32}$$

where the λ is the regularization parameter and the $\mathcal{P}(s)$ is the penalty function. We will focus on the MAP estimate, which becomes:

$$\begin{aligned} \hat{S}_{MAP} &:= \underset{S}{\operatorname{argmax}}\left\{\exp\left(-\frac{1}{2\sigma^2}\|x - Ls\|_2^2 + \frac{\lambda}{2\sigma^2}\mathcal{P}(s)\right)\right\} \\ &= \underset{S}{\operatorname{argmin}}\left\{\left\|X_{org} - Ls\right\|_2^2 + \lambda\mathcal{P}(s)\right\} \end{aligned} \tag{2.4.33}$$

2.4.4.1.1 MINIMUM NORM ESTIMATES (MNE)

The minimum norm estimates (MNE) (Hämäläinen & Ilmoniemi, 1994; Grech, et al., 2008) is using Tikhonov regularization by setting $\mathcal{P}(\mathrm{s}) = \|s\|_2^2$, which investigates the solution with minimum power (minimum norm) of the current density. This finds a distributed source solution which means that the dipole has a distributed activation instead of a point activation. The estimation of the source $\hat{S}_{MNE}$ could be obtained by the minimization of $\left\|X_{orig} - Ls\right\|_2^2 + \lambda\|s\|_2^2$, which alternatively can be expressed like:

$$\hat{S}_{MNE} = (L^T L + \lambda \mathrm{I}_{sources})^{-1} L^T X_{orig} \quad (2.4.34)$$

or

$$\hat{S}_{MNE} = L^T (L L^T + \lambda \mathrm{I}_{chs})^{-1} X_{orig} \quad (2.4.35)$$

If the $chs > sources$, the first equation is more appropriate. Otherwise, if the opposite is valid, then we use the second equation. The moment source $\hat{S}_{MNE_k} \in \mathcal{R}^{3x1}$ is in Cartesian system, for one source/position k and one sample. The MNE is more appropriate for reconstruction of spread activation that are located in cortical surface.

2.4.4.1.2 STANDARDIZED LOW RESOLUTION BRAIN ELECTROMAGNETIC TOMOGRAPHY (SLORETA)

The sLORETA (Pascual-Marqui, 2002; Hallez, et al., 2007; Lucka, et al., 2012) operates with the same estimation of the MNE and apart from that it standardizes the estimation source of MNE $\hat{S}_{MNE}$ by using its variance. The variance of the estimated current density can be computed from:

$$R = L^T (L L^T + \lambda \mathrm{I}_{chs})^{-1} L \quad (2.4.36)$$

The sLORETA estimates the standardized current density power for one source/position k as:

$$\hat{S}_{MNE_k}^T \{[R]_{kk}\}^{-1} \hat{S}_{MNE_k} \quad (2.4.37)$$

then $\hat{S}_{MNE_k} \in \mathcal{R}^{3x1}$ and the $[R]_{kk} \in \mathcal{R}^{3x3}$ is the k^{th} diagonal block of the R, all in Cartesian system. In our work we apply the Cholesky decomposition to illustrate the dipole on the symmetric inverse R. The covariance matrix R is semi-positive matrix and it becomes positive definite matrix due to the positive regularization parameter λ at (2.4.36). Thus, the Cholesky decomposition can be applied as $R^{-1} = A_R A_R^T$ to compute the moment estimation of the source(s) $\hat{S}_{sLOR}$:

$$\hat{S}_{MNE}{}^T A_R A_R^T \hat{S}_{MNE} = \left(A_R^T \hat{S}_{MNE}\right)^T \left(A_R^T \hat{S}_{MNE}\right) = \hat{S}_{sLOR}^T \hat{S}_{sLOR} \quad (2.4.38)$$

so,

$$\hat{S}_{sLOR} = A_R^T \hat{S}_{MNE} \quad (2.4.39)$$

In comparison with the MNE, the advantages of sLORETA are that without noise it has zero localization error and with noise it achieves better localization error. The sLORETA also has spread solution but is able to extract deeper sources. In our work, we want to extract deeper sources and for this reason we perform sLORETA.

2.5 CONNECTIVITY

2.5.1 INTRODUCTION OF CONNECTIVITY

The connectivity analysis is very useful at brain signal, since it investigates the connections of the different brain areas that their functionality has not been fully understood yet. The connectivity for EEG/MEG signals could be approached from channel to channel interaction or at a source level interaction. For the illustration of the connectivity we can use directed or undirected weighted graphs (Bastos & Schoffelen, 2016). The unidirectional connectivity is derived from the methods like weighted phase lag index (WPLI) or mutual information (MI). The directional connectivity (Omidvarnia, et al., 2013) is acquired by using the multivariate autoregressive (MVAR) models. The data are fitted in a MVAR model; the solution of this linear parametric model gives the coefficients matrix A. The matrix A has the information about the interactions between pairs of signals and is used to calculate causality methods such as directed transfer function (DTF) and the partial directed coherence (PDC). In our implementation we focus on directional connectivity with time-varying generalized orthogonalized partial directed coherence (tv-GOPDC).

2.5.2 MULTIVARIATE AUTOREGRESSIVE (MVAR) MODEL

The EEG/MEG signal records a time series for each channel with *M* time samples, so that the data measurement are defined as $X \in \mathcal{R}^{channels\, x\, samples}$ (where the channels = 1 … *N* and samples = 1 … *M*). The MVAR model (Baccalá & Sameshima, 2001; Baccalá & Medicina, 2007; Omidvarnia, et al., 2013) aims to describe the multivariate signal *X* at a time instant t by the sum of the p previous weighted samples of *X* with adding noise. This type of model for measurement data *X* at one time sample t is written as:

$$\begin{bmatrix} x_1(t) \\ \vdots \\ x_N(t) \end{bmatrix} = \sum_{r=1}^{p} A_r \begin{bmatrix} x_1(t-r) \\ \vdots \\ x_N(t-r) \end{bmatrix} + \begin{bmatrix} w_1(t) \\ \vdots \\ w_N(t) \end{bmatrix} \qquad (2.5.1)$$

and

$$A_r = \begin{bmatrix} a_{11}(r) & \cdots & a_{1N}(r) \\ \vdots & \ddots & \vdots \\ a_{N1}(r) & \cdots & a_{NN}(r) \end{bmatrix} \qquad (2.5.2)$$

where the p is the order of the model, the $w_i(t)$ is the white Gaussian noise for the i^{th} channel, for each delay $r = 1 \ldots p$, the coefficients matrix $A_r \in \mathcal{R}^{N\,x\,N}$ and each coefficient $\alpha_{ij}(r)$ is interpreted as the amount of linear influence that is exerted from the channel j at the time instant $t - r$ (i.e. $x_j(t - r)$) to the channel i at the time instant t (i.e. $x_i(t)$). The selection of the order p of MVAR model is an essential step for the computation of model coefficients and it is estimated by appropriate criteria like Akaike information criterion (AIC) [Akaike 1974, Ding 2000] and Bayesian information criterion (BIC) […]:

$$AIC(p) = 2\log\left(\det(\sigma_W^2)\right) + \frac{2N^2 p}{M} \qquad (2.5.3)$$

$$BIC(p) = 2\log\left(\det(\sigma_W^2)\right) + \frac{2N^2 log(M)p}{M} \qquad (2.5.4)$$

where σ_W^2 represent the covariance matrix of the white Gaussian noise, N is the total number of channels, M is the total number of samples and p is the order. The equation 2.5.5 can be expressed as:

$$\sum_{r=0}^{p} \bar{A}_r X(t - r) = W(t) \qquad (2.5.6)$$

When $r = 0$ the $\bar{A}_0 = \mathrm{I}$ and when $r > 0$ the $\bar{A}_r = -A_r$. Most methods implement this time-domain convolution-like equation and solve for the signal in the frequency domain as:

$$X(f) = \bar{A}^{-1}(f) \cdot N(f) = H(f) \cdot N(f) \qquad (2.5.7)$$

with $\bar{A}(f)$ equal to:

$$\bar{A}(f) = \mathrm{I} - \sum_{r=1}^{p} A_r e^{-i2\pi r f/f_s} \qquad (2.5.8)$$

Some other methods like coherence use the power spectrum of X as:

$$S(f) = X(f) \cdot X^*(f) = H(f) \cdot V \cdot H^H(f) \qquad (2.5.9)$$

where V is not dependent on frequency because denotes the power spectrum matrix of white Gaussian noise. There are different approaches for finding the coefficient of MVAR model (matrix $\bar{A}$). In this work we use the ARfit toolbox (Schneider & Neumaier, 2000), which applies a stepwise least squares algorithm estimating the coefficients of MVAR model. In addition, the optimal order p_{opt} is estimated by the Schwarz's Bayesian Information Criterion (BIC). Most often the model is computed in the frequency domain, so that the interactions among channels are also evaluated in the frequency domain using various considerations on $\bar{A}(f)$, viewed as a mixing matrix. Variations of the Partial Directed Coherence (PDC) are presented in subsequent sections.

2.5.3 PARTIAL DIRECTED COHERENCE (PDC)

The partial directed coherence (PDC) (Baccalá & Sameshima, 2001) is a method which highlights only the directed interactions between the channels. For instance, the channels $1, 2\ and\ 3$ have activity flow with the direction of the arrows $1 \leftarrow 2 \leftarrow 3$, the activity from 2 to 1 is the directed interaction and the activity from 3 to 1 is the undirected interaction because passes through other channel(s). Moreover, the PDC is a frequency domain method based on the calculation of the matrix $\bar{A}(f)$ from MVAR. The directed influence of the channel *j* at the channel *i* is expressed as:

$$\pi_{ij}(f) = \frac{\bar{A}_{ij}(f)}{\sqrt{\bar{\alpha}_j^H(f)\bar{\alpha}_j(f)}} \tag{2.5.10}$$

where $\bar{\alpha}_j$ is the j^{th} column of the $\bar{A}(f)$ and $\bar{\alpha}_j{}^H$ indicates the Hermitian transpose operation. If the $\pi_{ij}(f) = 0$ this means that for the frequency f the channel j does not influence the channel *i*. Otherwise if the $\pi_{ij}(f) = 1$ this implies that for the frequency f the channel *i* is driven by the channel *j*. Sometimes it is useful to calculate the total PDC in specific range of frequencies that is:

$$\int_{f_1}^{f_2} \pi_{ij}(f)df = \sum_{f=f_1}^{f_2} \frac{\bar{A}_{ij}(f)}{\sqrt{\bar{\alpha}_j^H(f)\bar{\alpha}_j(f)}} \tag{2.5.11}$$

The above equations calculate the PDC for the specific time instant *t* of the data *X*. The investigation of the time evolution of the channels interaction could be acquired by the time-varying PDC (tv-PDC) (Omidvarnia, et al., 2013). For this purpose, it is necessary to consider the matrix $\bar{A}$ depending on time and we need to calculate the $\bar{A}(f)$ for each time point via time-varying MVAR model:

$$\pi_{ij}(t,f) = \frac{\bar{A}_{ij}(t,f)}{\sqrt{\bar{\alpha}_j^H(t,f)\bar{\alpha}_j(t,f)}} \tag{2.5.12}$$

2.5.4 GENERALIZED PARTIAL DIRECTED COHERENCE (GPDC)

The generalized PDC (GPDC) (Baccalá & Medicina, 2007) is a variation of the original PDC that is invariant to amplitude scaling. Now, the influence from the channel *j* to the channel *i* is calculated by:

$$\tilde{\pi}_{ij}(f) = \frac{\lambda_{ii}^{-1}\bar{A}_{ij}(f)}{\sqrt{\bar{\alpha}_j^H(f)\Sigma_W^{-1}\bar{\alpha}_j(f)}} \tag{2.5.13}$$

where the λ_{ii} are the diagonal elements of the covariance noise matrix Σ_W.

2.5.5 GENERALIZED ORTHOGONALIZED PARTIAL DIRECTED COHERENCE (GOPDC)

The generalized orthogonalized PDC (GOPDC) (Omidvarnia, et al., 2013) has the properties of gPDC and additionally performs orthogonalization at the level of MVAR coefficients (i.e. matrix *A*) instead of being done at the measurement data. The orthogonalization process is used to diminish the co-variability due to spatial smearing (i.e. spatial diffusion or volume conduction effects) in the recordings of EEG channels. This activity is not produced by brain sources and can be lead to unreliable connectivity. Corresponding to the tv-PDC we calculate the time-varying GPDC (tv-GOPDC):

$$\tilde{\pi}_{ij}(t,f) = \frac{1}{\lambda_{ii}^2}\cdot\frac{\left|Real\{\bar{A}_{ij}(t,f)\}\right|\cdot\left|Imag\{\bar{A}_{ij}(t,f)\}\right|}{\bar{\alpha}_j^H(t,f)\Sigma_W^{-1}\bar{\alpha}_j(t,f)} \tag{2.5.14}$$

2.5.6 SURROGATE DATA ANALYSIS

The directional causality methods have highly non-linear relation with the time signals from which they are derived, so it is difficult to find the distributions of their estimators. This problem can be overcomed by an estimate empirical distribution using surrogate data (Kamiński, et al., 2001), on which the statistical significance of the results can be evaluated. The surrogate data form random and independent rearrangements of the time series for each channel. This procedure is useful for breaking the existing causality between the signals, forming the null hypothesis to be checked, i.e. absence of signal associations. Then the surrogate data pass through the same methods for finding the connectivity under this hypothesis. More specifically, they are fitted to MVAR model and after that the causality structure is calculated (e.g. GOPDC). This process is iterated for a large number of different surrogate data in order to compute the empirical distribution for the causality measure. The values of each interaction for all iteration are placed in a histogram in the form of frequencies providing the empirical distribution. Because the surrogate data have loose interactions between the original signals, the derived empirical distribution simulates the behavior of the null hypothesis reflecting the condition of zero causality, when there is no interaction between two signals. However, the residual noise can still create weak (random) interactions between the signals, which are captured by the empirical distribution. Finally, the assessment of the significance values of the derived causality structure of the model is examined by an appropriate threshold on the values of the empirical distribution reflecting a preselected confidence limit on the null hypothesis (i.e. reject all the activity that is under 90% of the empirical distribution). As a particular example, consider the case of (Figure 2. 13) obtained from the application of GOPDC in section 2.5.5. The first plot shows the histogram of GOPDC values for the couple (2,1) and frequencies considered. By summarizing over frequency, the second plot reflects the average (over frequencies) GOPDC histogram for the couple (2,1) of channels derived from the surrogate analysis. The selected threshold of 90% leads to the value of 0,3 as a threshold for assessing the significance of derived association (2,1) in our model.

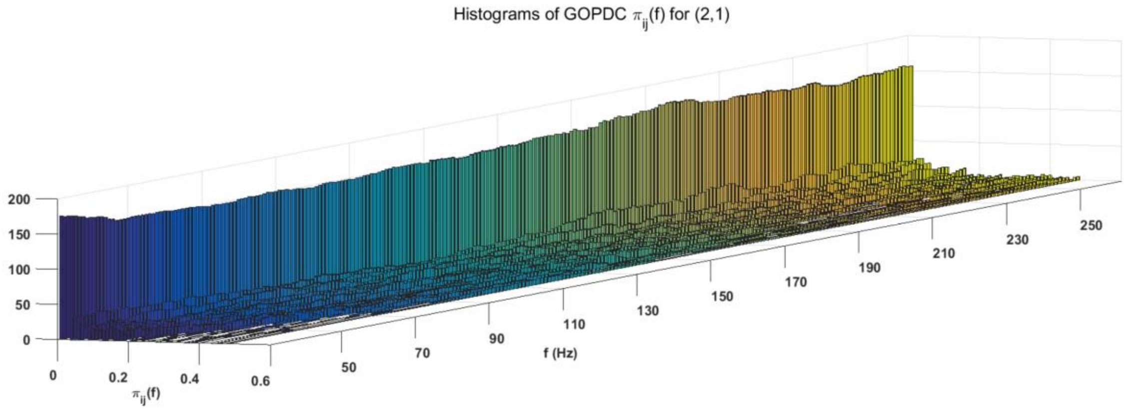

a)

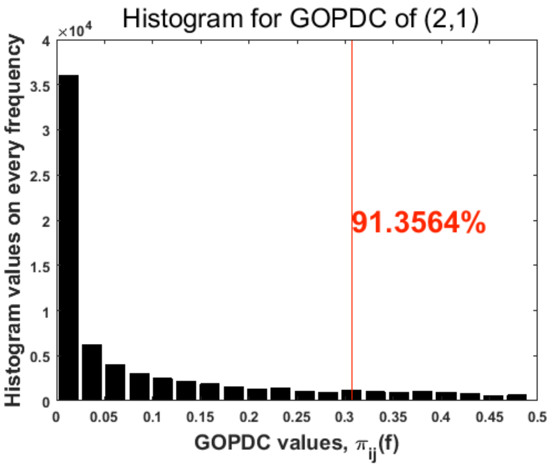

b)

Figure 2. 13: An example of computing the threshold for assessment of the significance values of the causality method a) The histogram of GOPDC for the couple (2,1) and b) the empirical distribution and the threshold value for the same couple.

CHAPTER 3: METHODOLOGY AND RESULTS

3.1 EXPERIMENT SETUP

A healthy subject underwent a median nerve stimulation on the right wrist using square electrical pulses with $0.5\ ms$ duration. The stimulus strength was adjusted until we saw a clear movement of the thumb. The inter-stimulus interval (ISI) was $400\ ms$ with a random deviation of $50\ ms$ avoiding the habituation. The measurement time was 10 minutes with a stimulus duration of $200\ ms$ and 1198 trials in total. Simultaneous EEG/MEG electrophysiological activity was acquired with a sample frequency of $1200\ Hz$. The EEG system consist of 74 electrodes (plus adding 6 electrooculogram EOG and one electrocardiogram ECG). The MEG system (VMS MedTech Ltd) was comprised of 275 first order axial gradiometers (plus adding 29 references to calculate synthetic gradiometers). The anatomical characteristics of the subject were included T1w-, T2w- and diffusion tensor imaging (DTI) sequences scanned by a 3 T MAGNETOM MRI (Siemens Medical Solutions) with $1\ mm$ accuracy.

3.2 ACQUISITION AND PREPROCESSING

The preprocessing is implemented with the high level FieldTrip toolbox at MATLAB (Oostenveld, et al., 2011), which is an open source software for analyzing the EEG and MEG data. Most of the functions in FieldTrip take as input a configuration structure (cfg) with all necessary information for the function. The first step is to read the data from EEG and MEG in the same structure with the function *ft_preprocessing* which takes as input the path with the name of the data experiment. In our case, the event is an electrical stimulus at the wrist for the right hand, it comes approximately at time 0 seconds and the window of analysis is from -0.1 seconds for the pre-stimulus to 0.2 seconds for the post-stimulus activities. This information is used for the isolation of trials of interest from the raw data by using the function *ft_definetrial*, which produces a new configuration structure. The *ft_redefinetrial* takes as input that configuration structure together with the raw data and returns the event related potential and field (ERP and ERF) data trials of our experiment. Then, we apply the band-pass filter from 20 to 250 Hertz to keep the frequency of interest, a Notch filter for eliminating of harmonics of power line noise of 50 Hz and the window of each trial is defined as the time interval from -0.1 to 0.2 seconds. This is done again with the *ft_preprocessing* function, but with different configuration structure and the data trials as input. The *ft_preprocessing* separates in different structures the EEG and MEG data trials. The conversion of the gradiometers in 3rd order is done with the *ft_denoise_synthetic* function. Furthermore, the visual inspection and rejection of the bad channels and trials for each structure is done by the routines *ft_databrowser* and *ft_rejectvisual* (Figure 3. 1 and Figure 3. 2). The latter offers a visual way to investigate the bad channels and trials, whereas the identification of outliers has been performed using metrics like z-value, kurtosis and variance. In addition, we take into consideration the bad channels that are manually observed within the duration of the experiment. Then, we re-reference the EEG data at common average reference over all electrodes with *ft_preprocessing*. Furthermore, for both structures the time-locked analysis (TLA) is applied which is an average of the trials at each channel *ft_timelockanalysis* (Figure 3. 3). Finally, the plotting of the activities at the specific times is done by *ft_topoplotER* (Figure 3. 4).

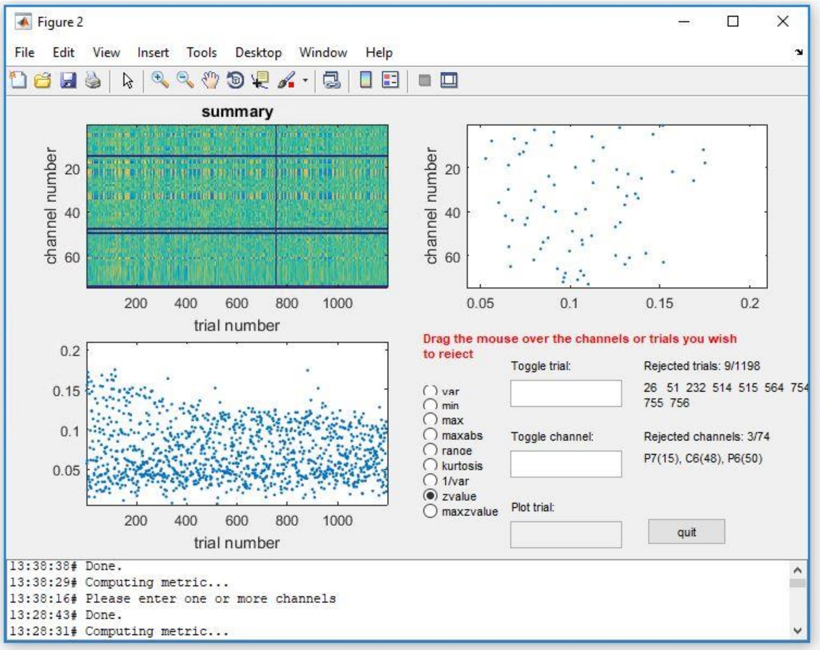

Drag the mouse over the channels or trials you wish to reiect

○ var
○ min
○ max
○ maxabs
○ ranoe
○ kurtosis
○ 1/var
● zvalue
○ maxzvalue

Toggle trial:

Rejected trials: 9/1198

26 51 232 514 515 564 754 755 756

Toggle channel:

Rejected channels: 3/74

P7(15), C6(48), P6(50)

Plot trial:

```
13:38:38# Done.
13:38:29# Computing metric...
13:38:16# Please enter one or more channels
13:28:43# Done.
13:28:31# Computing metric...
```

Figure 3. 1: The visual inspection and the rejection of the bad channels and trials is done by using the metrics z-value, kurtosis and variance from ft_rejectvisual.

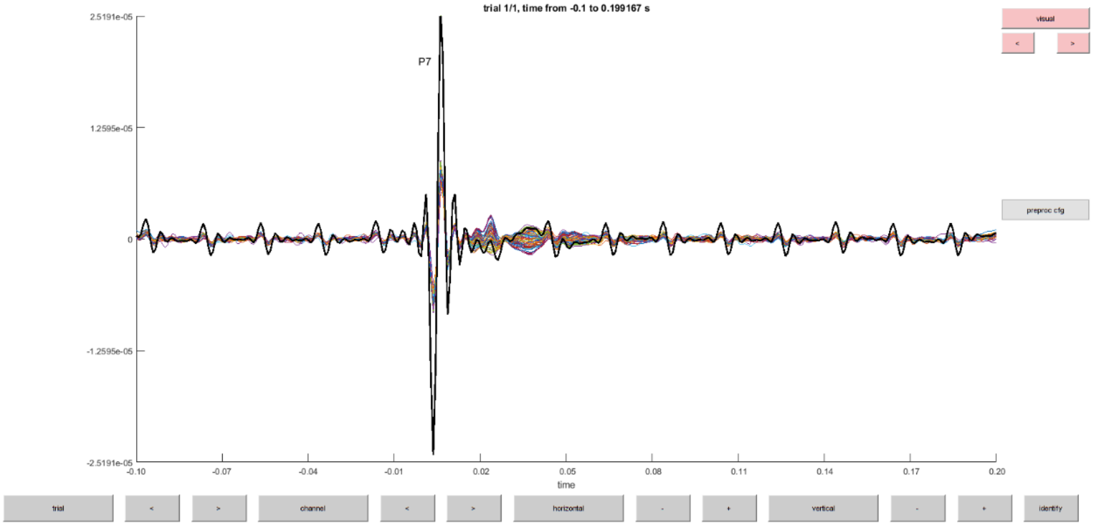

Figure 3. 2: Visual detection of the bad channel P7 at EEG data, which has high amplitude by using the ft_databrowser.

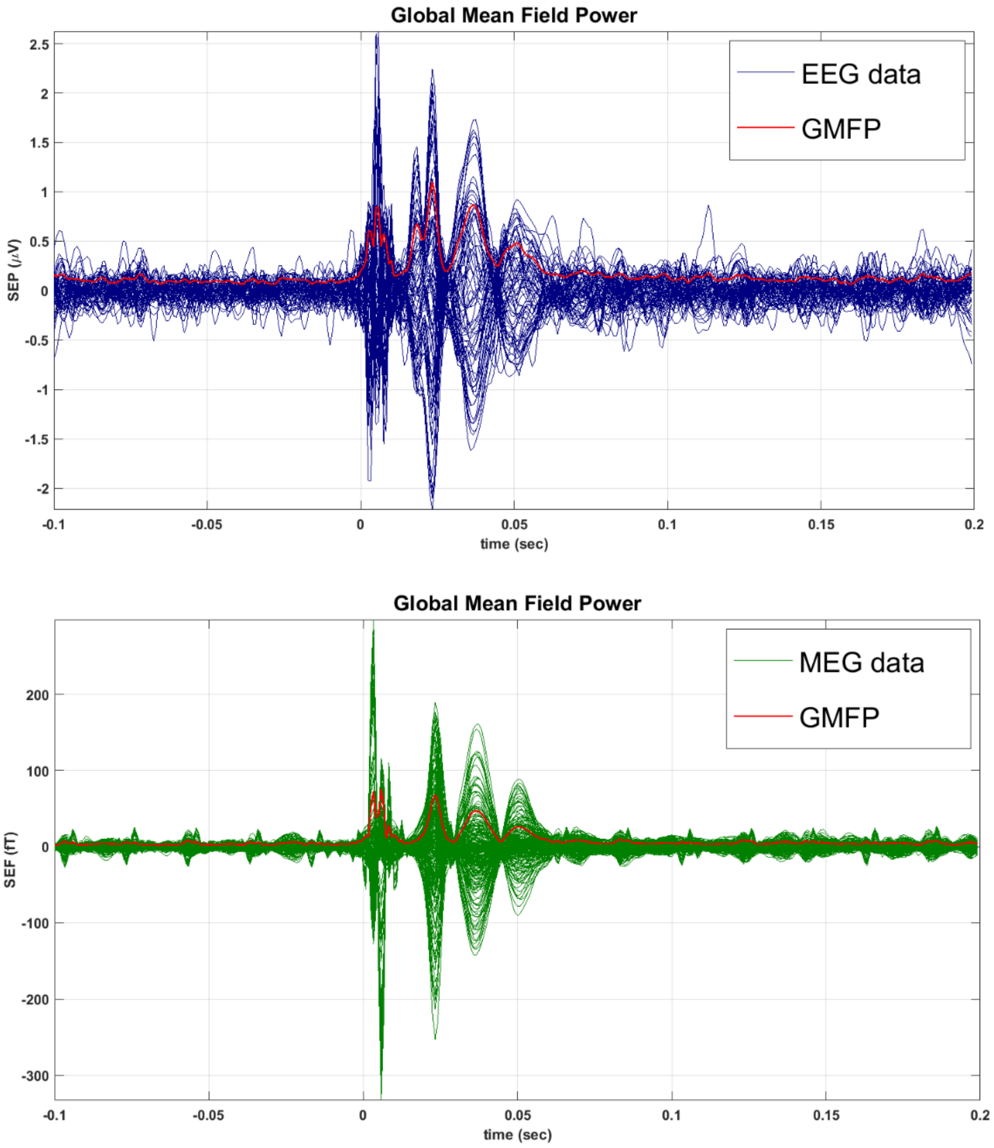

Figure 3. 3: The SEP (above) and SEF (below) after the preprocessing steps together with the GMFP.

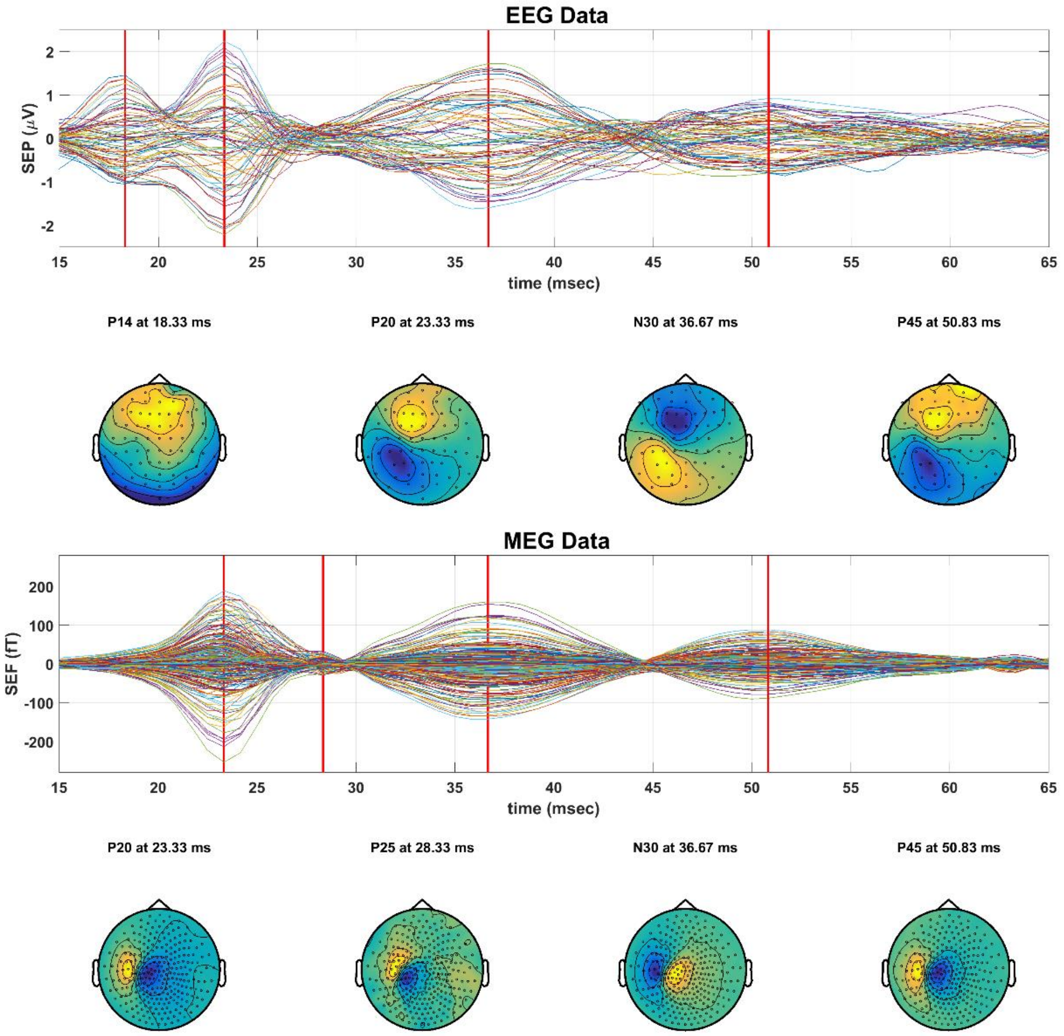

Figure 3. 4: The SEP and SEF at the interval of interest with the functional components.

The functional Components which are revealed by EEG and MEG are illustrated in Figure 3. 4 and Table 1. For simplicity reasons, only the first name of the components will be used. For the next sections we will use the 3b area which is an average activation of the P20 and N30. Furthermore, the MEG detects a small activation around at 28 ms the component P25. However, the investigation of this component needs more trials due to very low amplitude, so we exclude this from further analysis.

	P14	P20	P25	N30	P45	3b
EEG	18.33 ms	23.33 ms	–	36.67 ms	50.83 ms	30 ms
MEG	–	23.33 ms	28.33 ms	36.67 ms	50.83 ms	30 ms

Table 1: The somatosensory functional components and the actual times of their peaks for each modality together with the 3b area.

3.3 FUNCTIONAL SOURCE SEPARATION (FSS)

The separation and enhancement of each functional component from the mixed observed measurements is done by the semi-blind technique FSS. This formulation facilitates the extraction of functional components with evident activity, so as to examine the connectivity between such components at further steps. The first step of FSS is to find the temporal limits of a priori informative regions for each functional component around its maximum activation (i.e. $\Delta 1t_k$ and $\Delta 2t_k$ from eq. 2.3.16). In our implementation scheme, we empirically choose five points around the peaks, which can be detected from the GMFP that is calculated on the time-locked data. We append all trials of clean data, subtract the mean from the rows and whiten them (by using the PCA as whiting step only) $X_{ap} \in \mathcal{R}^{channels\ x\ (samples\ x\ trials)}$, and we keep the matrices of transformations. We define the cost function $F = J + \lambda R_{FSk}$ for the k^{th} functional component as is determined at section 2.3.4. The cost function takes as input an initial random unmixing vector $W_{in} \in \mathcal{R}^{1\ x\ channels}$ and the appended data X_{ap}. For each functional component, the simulated annealing (SA) finds the global optimum for the cost function and returns the an optimal unmixing vector $W_{opt} \in \mathcal{R}^{1\ x\ channels}$. In each iteration i of the SA, the appended functional source $FS_{ap_i} = W_i \cdot X_{ap}, \in \mathcal{R}^{1\ x\ (samples\ x\ trials)}$ is computed. Then, the $FS_{avg_i} \in \mathcal{R}^{1\ x\ samples}$ is derived by averaging the trials of FS_{ap_i} and it is used for the calculation of R_{FSk_i} for the new cost value F_i. Finally, when we find the W_{opt}, we normalize it and the final appended functional source for k^{th} the functional component becomes $FSk_{ap} = W_{opt} \cdot X_{ap}, \in \mathcal{R}^{1\ x\ (samples\ x\ trials)}$. Furthermore, the back-projected data is computed as $backproFSk = inv(W_{opt}) \cdot FSk_{ap}, \in \mathcal{R}^{channels\ x\ (samples\ x\ trial)}$. We restore the original amplitudes of signals by adding the mean from before and applying the inverse procedure of whitening. Then, we separate the trials and apply time-locked analysis to derive the final data as $backproFSk \in \mathcal{R}^{channels\ x\ samples}$. Additionally, for illustration reasons (Figure 3. 5) we compute the average of trials at the final functional source $FSk \in \mathcal{R}^{1\ x\ samples}$. The parameters that we use are: The λ is set at $1e^5$ for EEG and $1e^3$ for MEG and for SA the cooling factor $\alpha = 0.8$, initial temperature at 1, stop temperature at $1e^{-16}$ and max iteration at 300.

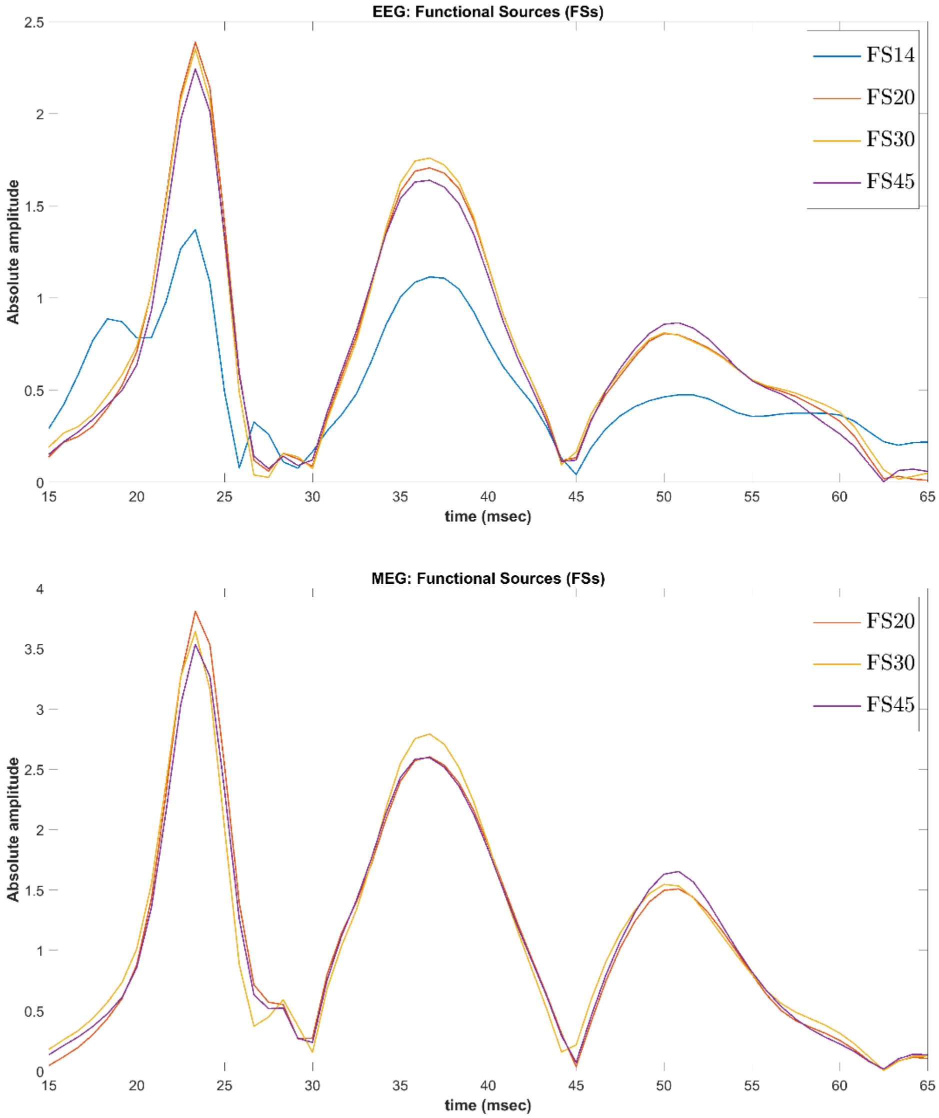

Figure 3. 5: The average of trials functional sources of the EEG (above) and the MEG (below)

Each average functional source FSk (Figure 3. 5) is enhanced around the corresponding peaks of the functional components (Table 1). The clearest example is FS14, which has higher amplitude around the peak of the P14 at 18.33 ms because the P14 is the only component that its activation starts before others. In the figures (Figure 3. 6 and Figure 3. 7) below, we show together the measurement data and $backproFSk$ with two different ways. The first way is with signals, in which the limits are not so easily represented. Therefore, we also use the second way that takes the limits and makes two surfaces one for the measurement data and one for the $backproFSk$.

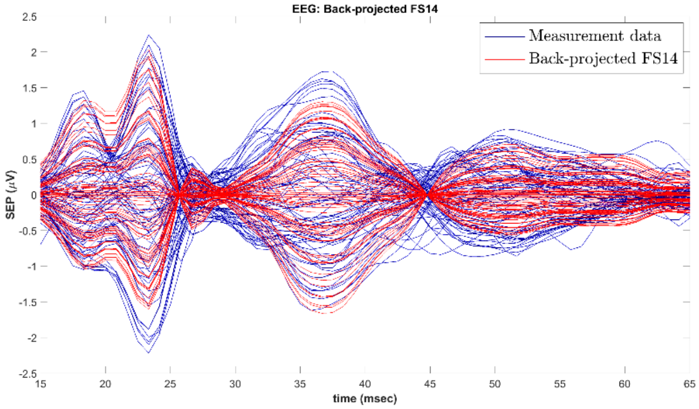
EEG: Back-projected FS14

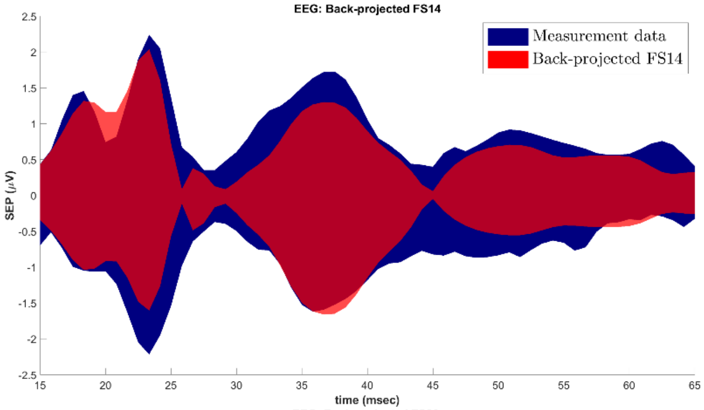
EEG: Back-projected FS14

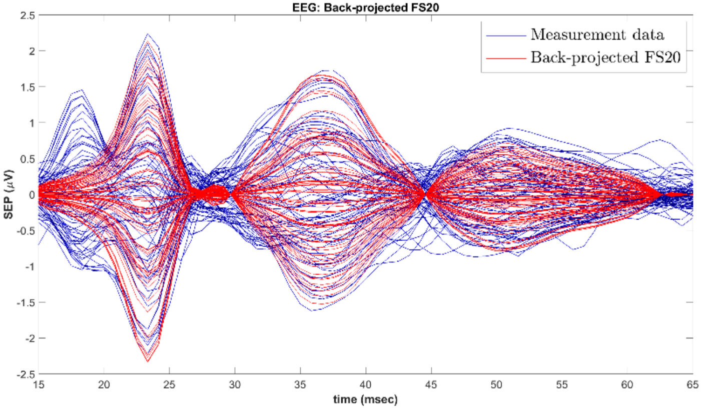
EEG: Back-projected FS20

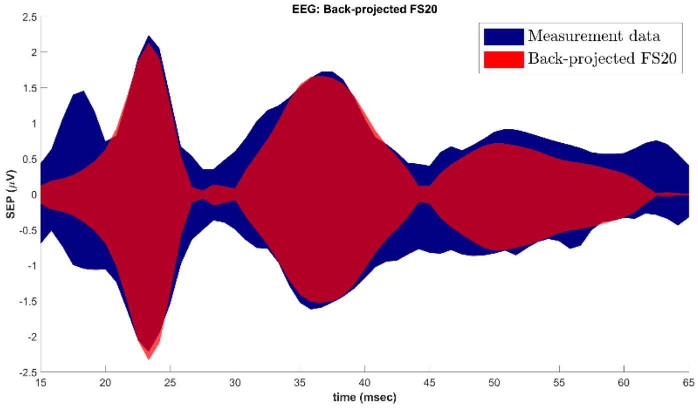
EEG: Back-projected FS20

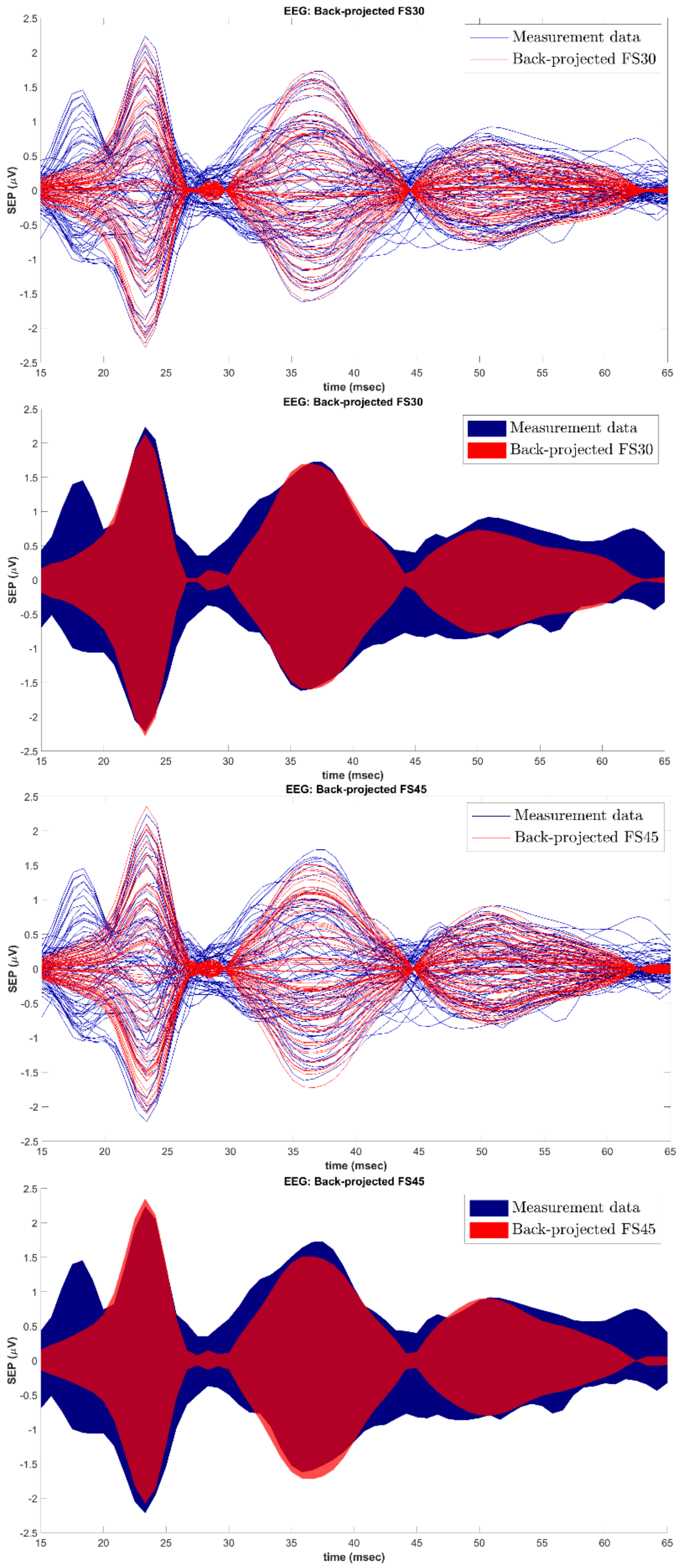

Figure 3. 6: Comparison the back-projected FSk for the EEG components P14, P20, N30 and P45 with EEG measurement (observed) data.

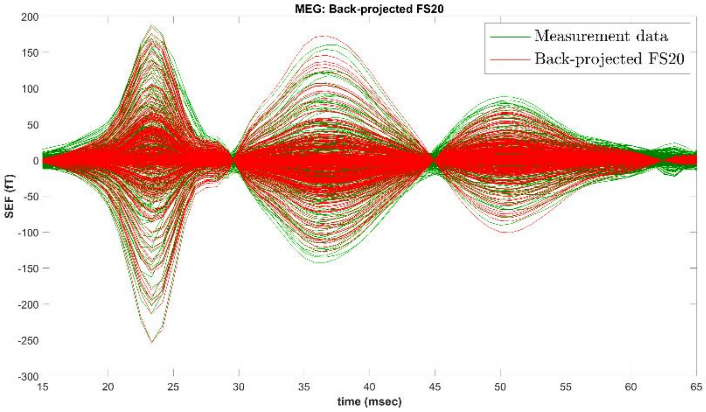
MEG: Back-projected FS20
Measurement data
Back-projected FS20
SEF (fT)
time (msec)
200
150
100
50
0
-50
-100
-150
-200
-250
-300
15
20
25
30
35
40
45
50
55
60
65

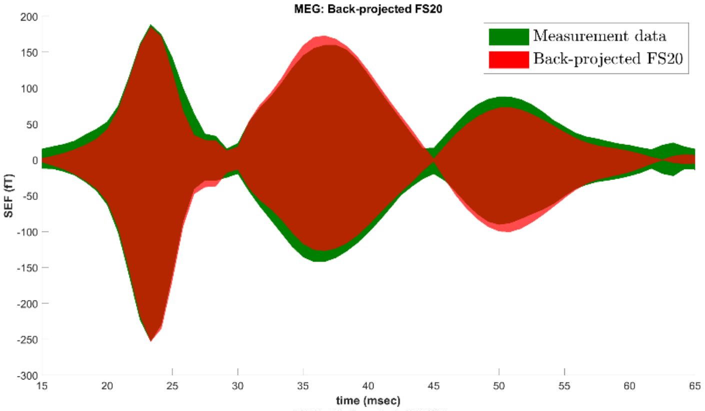
MEG: Back-projected FS20
Measurement data
Back-projected FS20
SEF (fT)
time (msec)
200
150
100
50
0
-50
-100
-150
-200
-250
-300
15
20
25
30
35
40
45
50
55
60
65

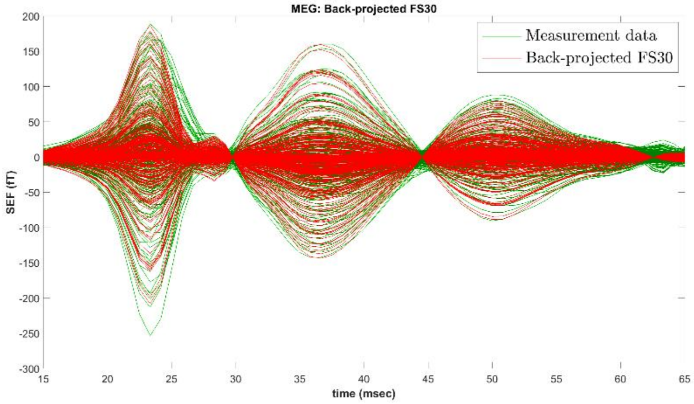
MEG: Back-projected FS30
Measurement data
Back-projected FS30
SEF (fT)
time (msec)
200
150
100
50
0
-50
-100
-150
-200
-250
-300
15
20
25
30
35
40
45
50
55
60
65

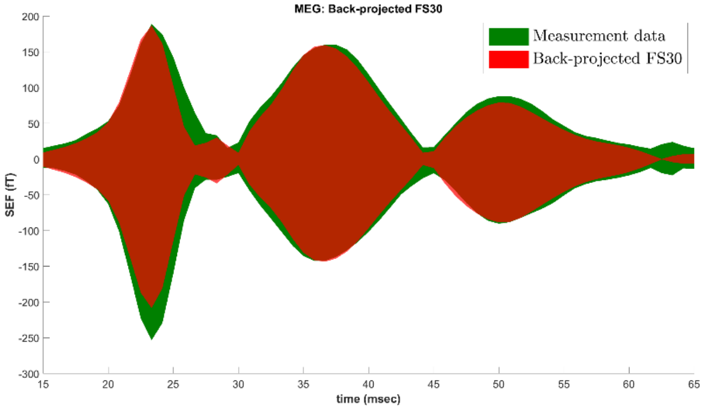
MEG: Back-projected FS30
Measurement data
Back-projected FS30
SEF (fT)
time (msec)
200
150
100
50
0
-50
-100
-150
-200
-250
-300
15
20
25
30
35
40
45
50
55
60
65

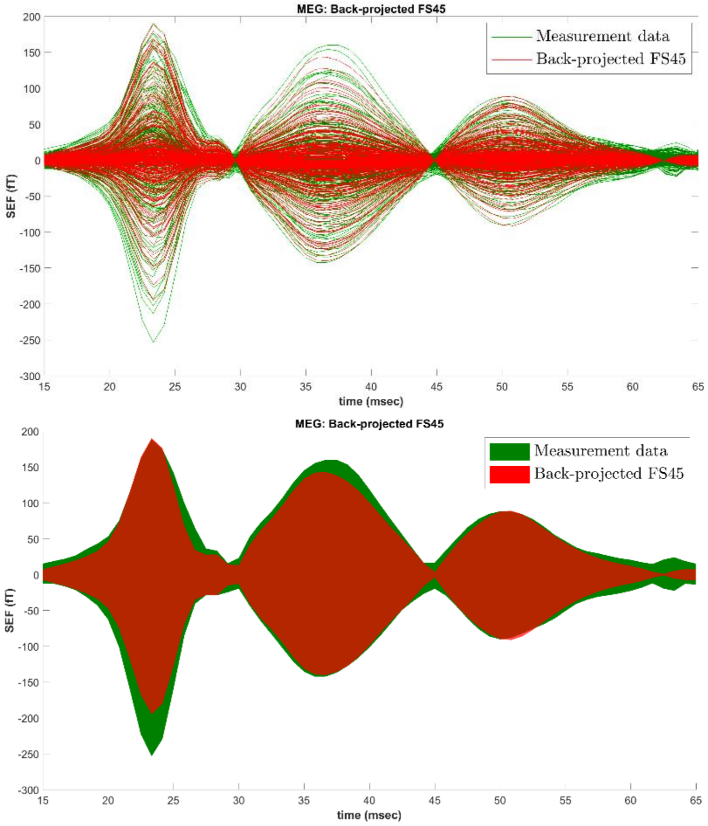

Figure 3. 7: Comparison the back-projected FSk for the MEG components P20, N30 and P45 with MEG measurement (observed) data.

The $backproFSk$ data of each modality (Figure 3. 6 and Figure 3. 7) captures almost the entire activation of the corresponding component and subsequently suppresses (sometimes in greater and sometimes to a lesser extent) other component activations.

3.4 SOURCE ANALYSIS

In this section we are searching for the topological areas inside the brain, which produce the functional components. Thus, the evaluation of the localization of our results and the computation of the source waveforms of each functional component are accomplished. As mentioned in section 2.4, the source localization consists of two main steps (Figure 3. 8): the forward and the inverse solutions. The former computes the lead-field, which is a requirement for the latter step, and takes as input the head model, source model and the position of the electrodes or sensors. In our work, we use the realistic head model that is produced by FEM that comprises six tissues (skin, skull compacta, skull spongiosa, CSF, gray and white matter) and it is constructed by the images of MRI T1w- and T2w- using MATLAB and SPM12 – FieldTrip (Oostenveld, et al., 2011). The mesh of the head model is constructed by the FEM with hexahedral as finite elements to include the brain anisotropy and the calibrated skull conductivities and (Aydin, et al., 2014). A Venant source model is simulated by using the SimBio package with 17618 positions at the cortical gray matter . The inverse solution takes as input the appropriate lead-field(s) and the $backproFSk$ from one of the modalities (EEG, MEG or EMEG). The EMEG is computed by using the EEG and MEG $backproFSk$ data of the same components k except for the first component, which is not detected by the MEG and in this case its values are zero padded. The sLORETA method is used to solve the inverse solution and computes the power for each source point, so that it forms a spread solution. The parameter λ in equations (2.4.34-36) is set empirically equal to five. For every $backproFSk$ of each modality (EEG, MEG or EMEG) and for each time point, we repeat the solution of source localization, as indicated in Figure 3. 8. Before the sLORETA begins, the lead-field and the $backproFSk$ data are made unitless by using the covariance noise matrix of the respective observed data, which is calculated at the pre-stimulus duration.

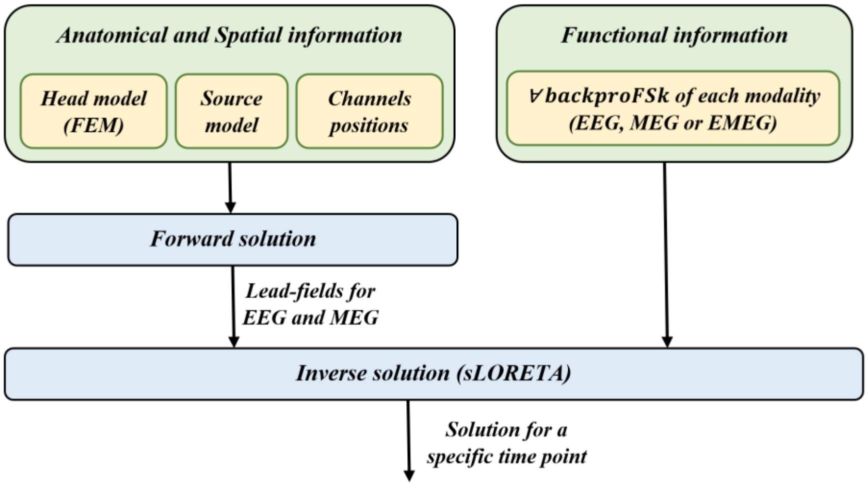

Figure 3. 8: Diagram of the source localization in our implementation.

Therefore, for each $backproFSk$ the source waveform $sLOR\_FSk$ is produced by taking the average of 100 samples in the source space with maximum power, which is less than 0.2% of the total source space. For the sake of simplicity, the MRI images in the following figures do not illustrate the entire sLORETA activation for each source space but only the power values above the $0.5 \cdot \max(power\ values)$, which are then normalized. Additionally, the dipoles at MRI images are produced by the same 100 average points by the Cholesky decomposition as we explain in section 2.4.4.1.2. Because the average position of the dipole does not always matches with an available slice of MRI, the nearest slice is selected for illustration. Additionally, our source model does not include positions at subcortical areas so the subcortical component P14 is computed by the nearest source space positions to subcortical.

EEG sLORETA activation and dipole of P14 at 18.33 ms

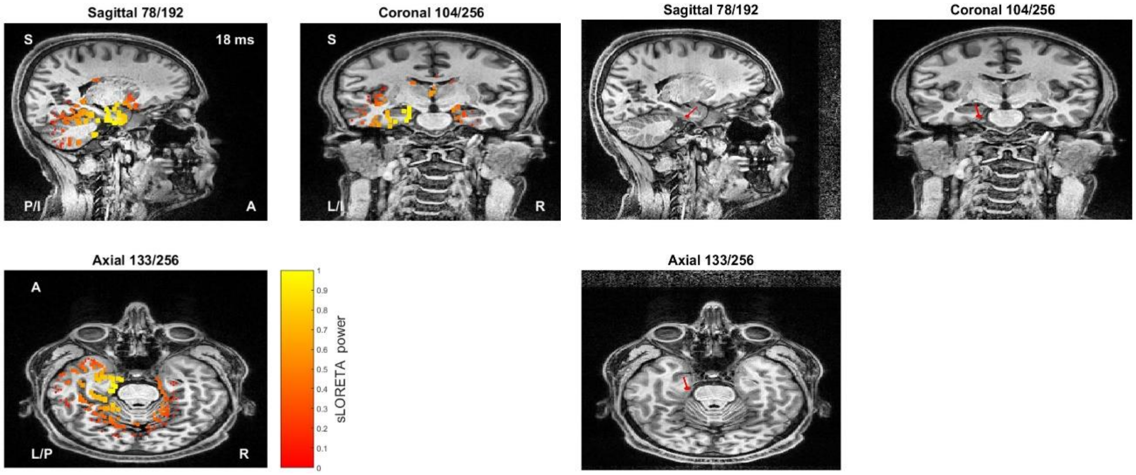

EEG sLORETA activation and dipole of P20 at 23.33 ms

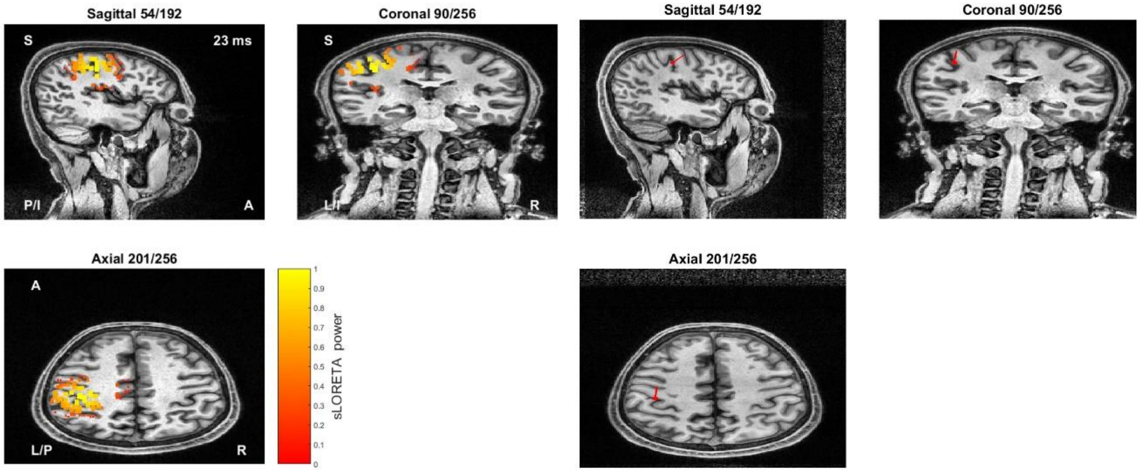

EEG sLORETA activation and dipole of N30 at 36.67 ms

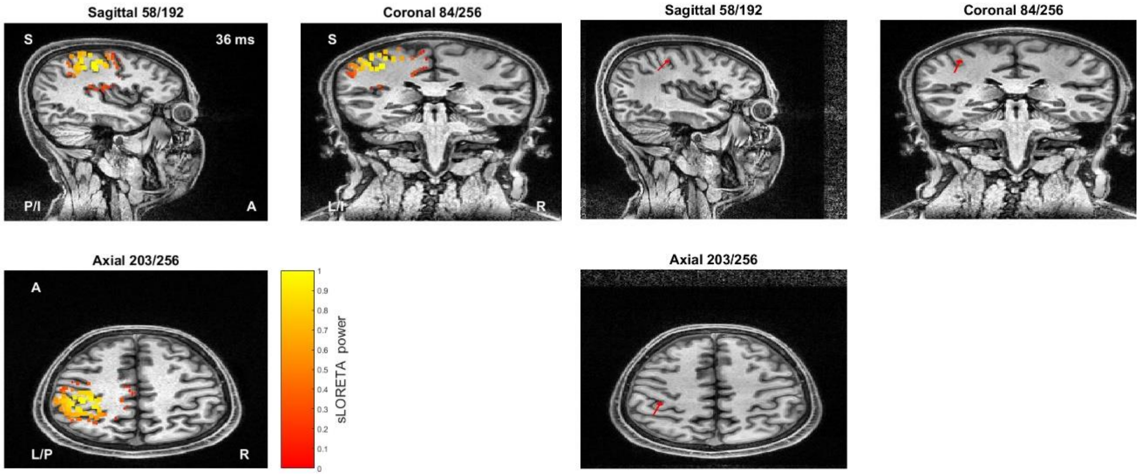

EEG sLORETA activation and dipole of P45 at 50.83 ms

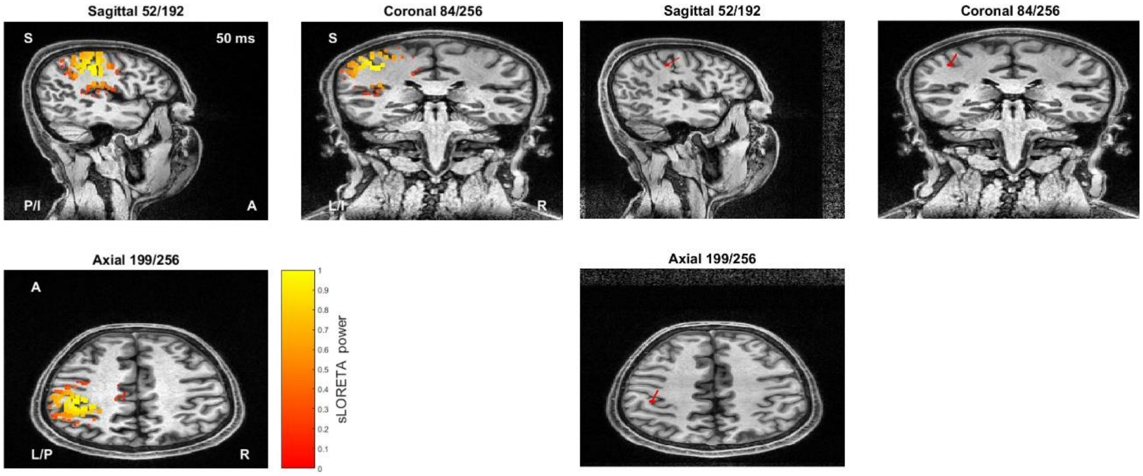

Figure 3. 9: The sLORETA activations and dipoles for the functional sources (FSs) of EEG

MEG sLORETA activation and dipole of P20 at 23.33 ms

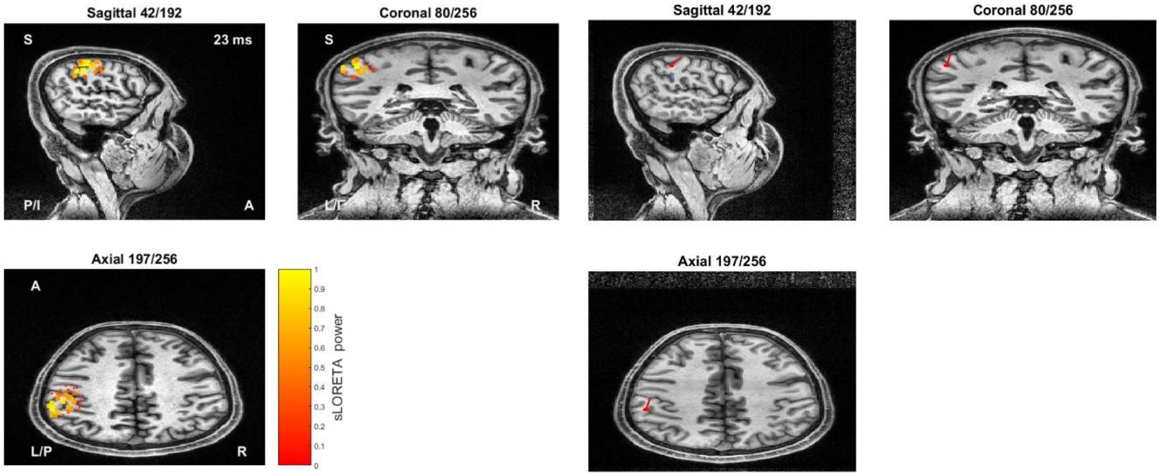

MEG sLORETA activation and dipole of N30 at 36.67 ms

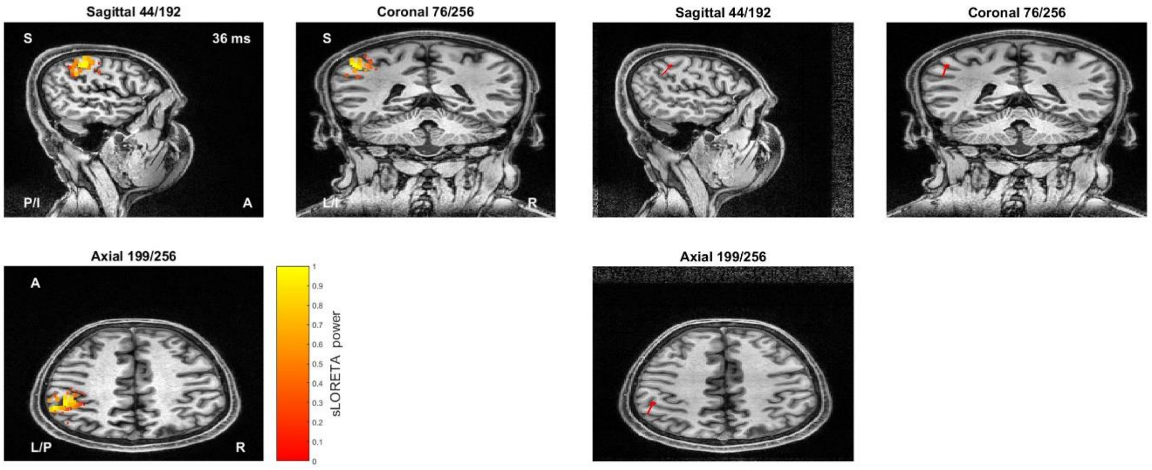

MEG sLORETA activation and dipole of P45 at 50.83 ms

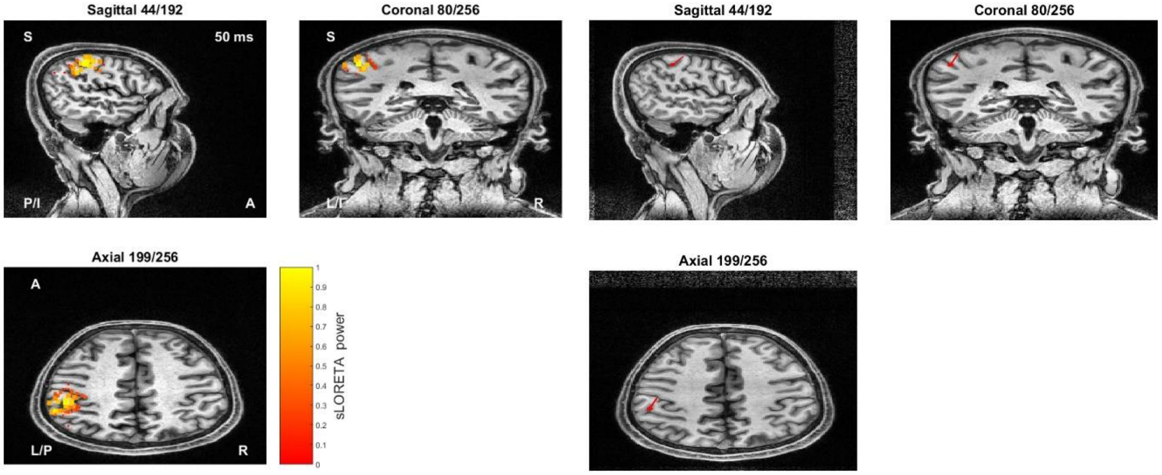

Figure 3. 10: The sLORETA activations and dipoles for the functional sources (FSs) of MEG

EMEG sLORETA activation and dipole of P14 at 18.33 ms

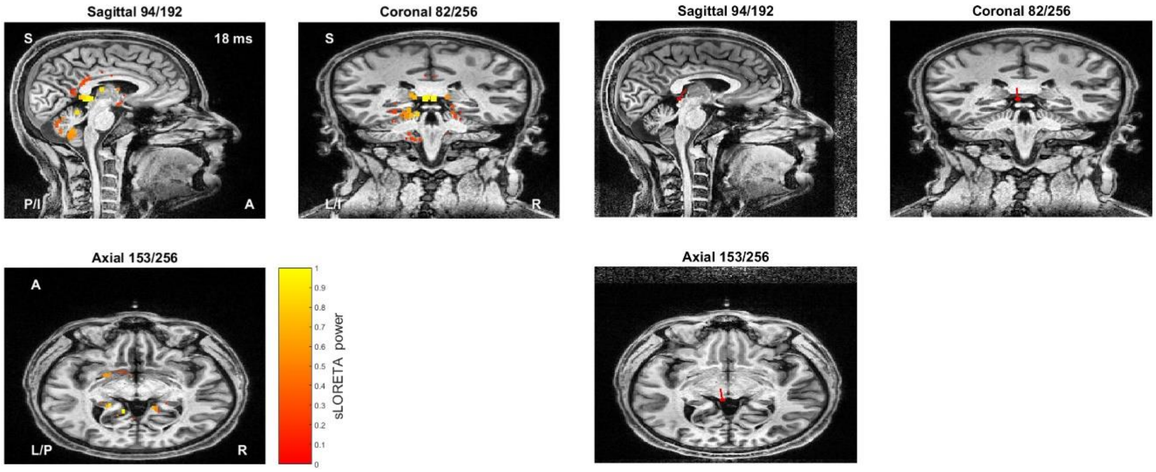

EMEG sLORETA activation and dipole of P20 at 23.33 ms

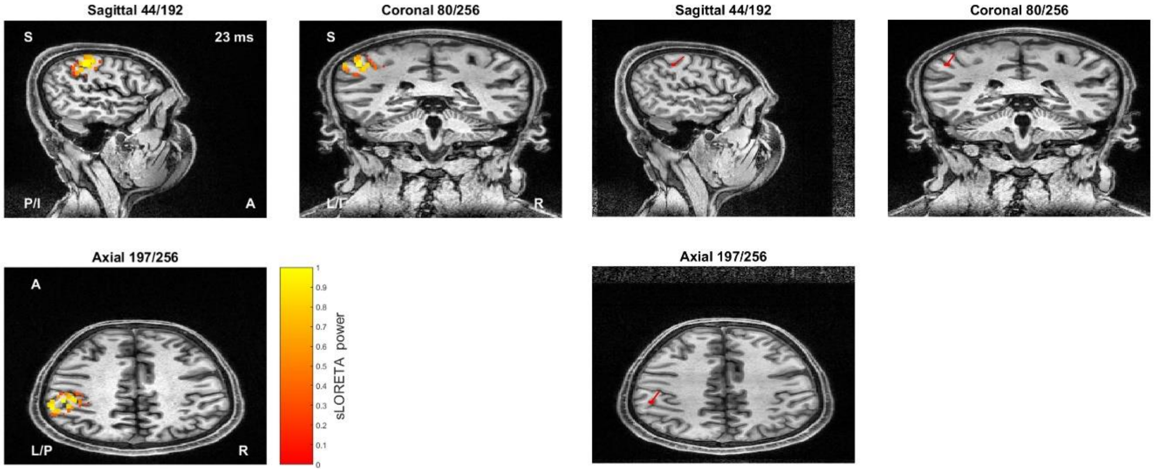

EMEG sLORETA activation and dipole of N30 at 36.67 ms

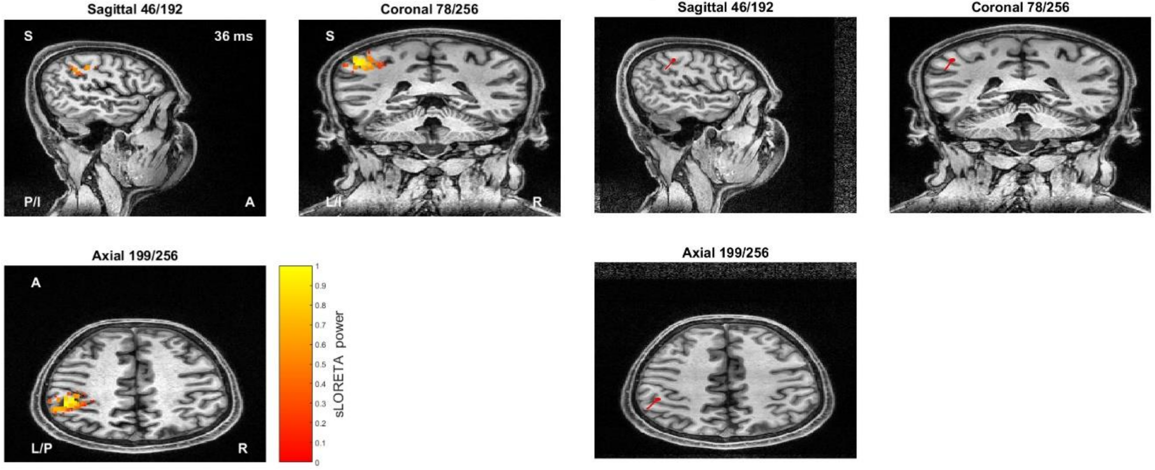

EMEG sLORETA activation and dipole of P45 at $50.83\ ms$

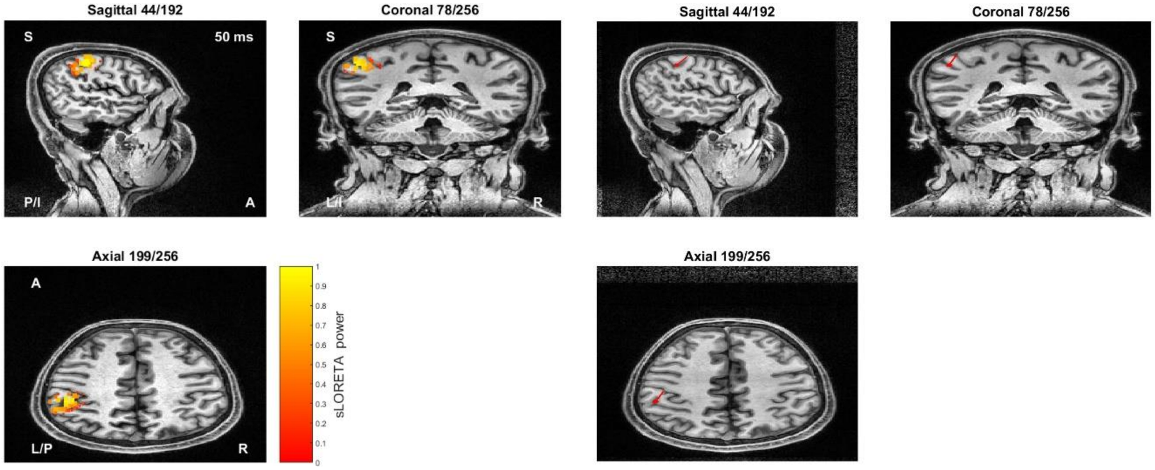

Figure 3. 11: The sLORETA activations and dipoles for the functional sources (FSs) of EMEG

The sLORETA achieves good localization for each modality as shown in above figures. More specifically, the deep and most radial component P14 with peak at 18.33 ms is located near to Thalamus in both EEG and EMEG, with better localization at EMEG. All the rest, most tangential components are localized near to the central sulcus and the primary somatosensory cortex. This small divergence is logical due to the fact that we use average positions for the dipoles and non-invasive measurements which import noise to our data and we also employ techniques that loose a small amount of information. Perfect localization can theoretically be achieved only if the ideal data are obtained without noise and processed through a lossless scheme, otherwise the inversion crime occurs (Lucka, et al., 2012).

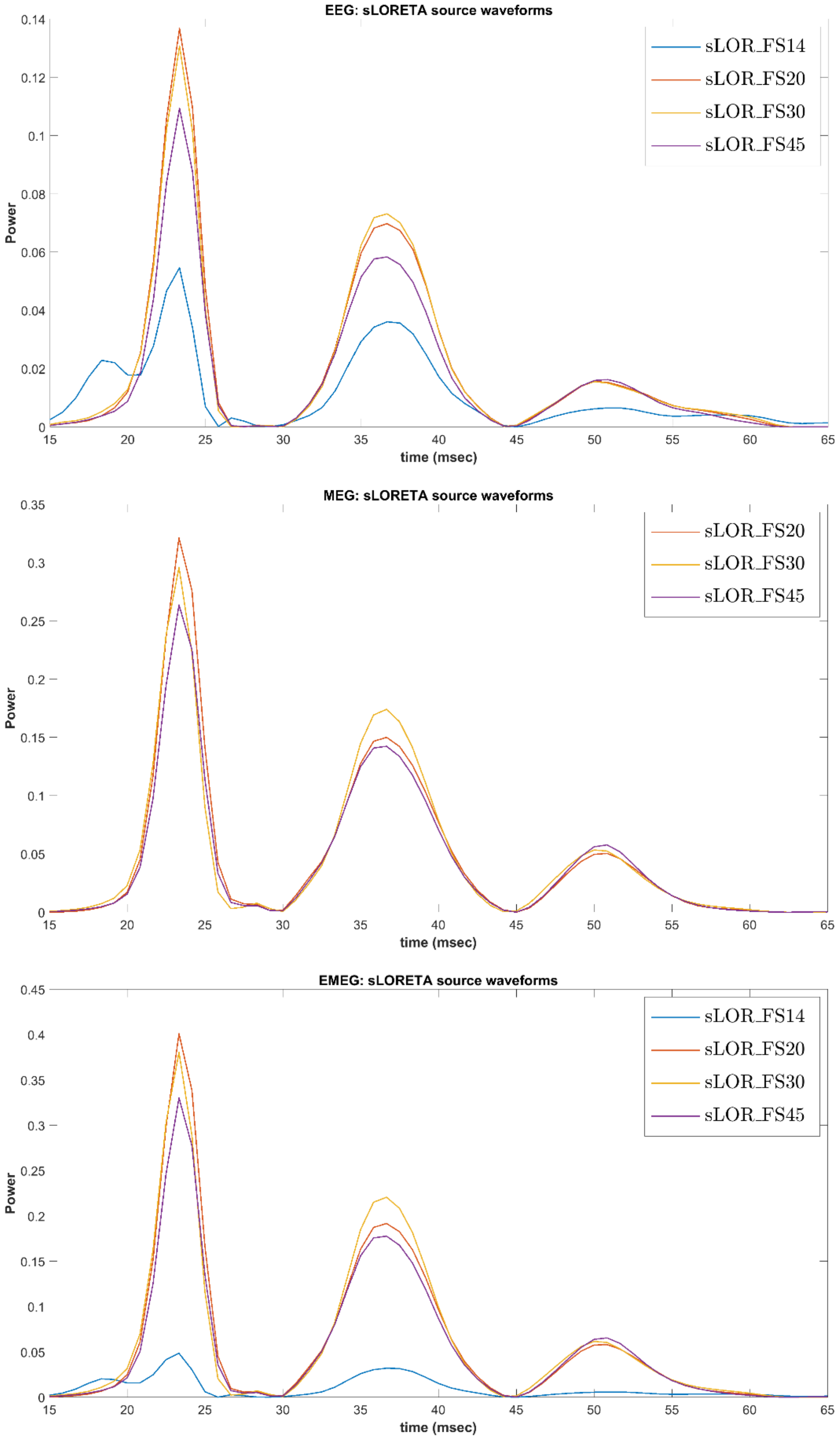

Figure 3. 12: The sLORETA source waveforms of the average of 100 maximum power activations for each modality (above: EEG, middle: MEG and below: EMEG)

At each source waveform $sLOR\_FSk$ and for each modality shown in Figure 3. 12, we can observe a higher or smaller enhancement around the peaks of the functional components (Table 1) at the corresponding $sLOR\_FSk$. For instance, let us take the simple case of the functional component P14 at the EEG measurements, which has a maximum peak of around 18 ms, and it is the only component whose activation starts before the others. We can see that the corresponding source waveform $sLOR\_FS14$ is more enhanced from other source waveforms around this peak. The case of other components is more complicated because there are simultaneous activations of many functional components. Thus, in these cases we see the corresponding source waveforms $sLOR\_FSk$ to follow similar patterns. However, we have succeed to enhance the corresponding source waveforms $sLOR\_FSk$ around the corresponding peaks. Furthermore, it can be easily noticed from the above figures (Figure 3. 12) that the EMEG keeps the information of $sLOR\_FS14$ from EEG and at the same time enhances the other three source waveforms that are common for both EEG and MEG.

3.5 CONNECTIVITY

In this section we investigate the connectivity analysis for the source waveforms $sLOR\_FSk$ of the three modalities EEG, MEG and EMEG (Figure 3. 12). A window of 10 ms is selected for the calculation of the tv-GOPDC, which corresponds to 12 time samples. Each next window is selected with latency of 1 time sample from the previous one (i.e. two successive windows differ by one sample). The number of surrogate data is chosen to 300 and the threshold on the surrogate data distribution (for the H_0 hypothesis) is set at 90%. The algorithm starts from the source waveforms $sLOR\_FSk$ of one modality. For each iteration, a window is selected and fitted in the MVAR model. The matrix coefficients $\bar{A}$ is calculated by using the ARfit toolbox (Schneider & Neumaier, 2000), which takes as input the window of the $sLOR\_FSk$, a range of orders for the MVAR model, which in our case is selected from 1 to 2, and the method for finding the optimal order p_{opt}, which in our study is the Schwarz's Bayesian Information Criterion (BIC). After the calculation of the tv-GOPDC, the step of thresholding starts with estimating the empirical distribution for each window as mention in section 2.5.6. Both tv-GOPDC and surrogate data are computed in absolute value. Since the tv-GOPDC is in a time-frequency domain and we need to express it in time domain, the mean of frequencies for the range of 20 to 250 is calculated. Thus, each window refers to a single time instant that is set at the middle of the window. For instance, at the window from 10 ms to 20 ms the time instant is set at 15ms. The figures below illustrate the interaction between of the functional components as they are derived from the tv-GOPDC of the corresponding $sLOR\_FSk$. The illustration of graphs for each modality have been given on three time instants, one for each of the following interactions: $P14 \rightarrow 3b$, $3b \rightarrow P45$ and $P45 \rightarrow 3b$, which represent a possible and logical propagation of signal in respect of anatomical features. In other words, after the signal from peripheral nervous system has arrived in Thalamus, this propagation is about to start in the form that the first interaction is thalamocortical followed by corticocortical interactions. Each one of these interactions represents the maximum influence at tv-GOPDC of the first component to the second, around its peak ($P14, 3b$ and P45 at Table 1) for a range of a $\pm 5\ ms$ since we use a window 10 ms. Let us consider for example the interaction $P14 \rightarrow 3b$, where the functional component P14 of EEG has peak at 18.33 ms. In this case, we are searching at a range of 13.33 to 23.33 ms to find the biggest influence of P14 to the 3b area. Thus, the following graphs represent a time instant of the maximum activation of each functional component around its peak. The graphs are in a time order matching the sequence of component activations: first is the P14, second the 3b area and third the P45 except for the MEG cannot capture the P14 component and starts from 3b area. Additionally, the causalities inside the 3b area are also illustrated, which has to do with the interaction of the P20 with the N30.

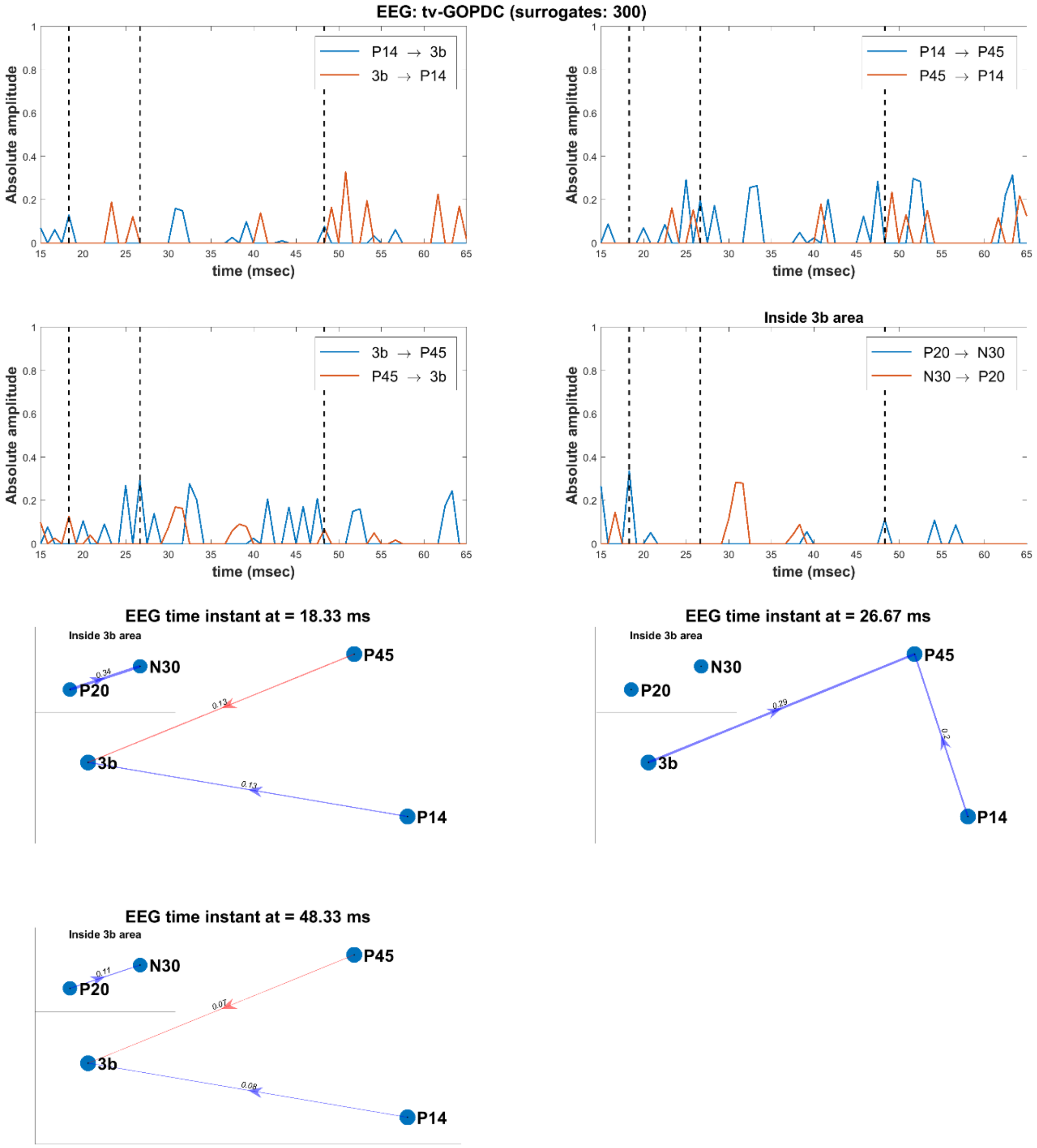

Figure 3. 13: The tv-GOPDC causalities of the functional component (above) and the graphical representation of these causalities at specific time instant of interest (dashed vertical lines) for the EEG modality.

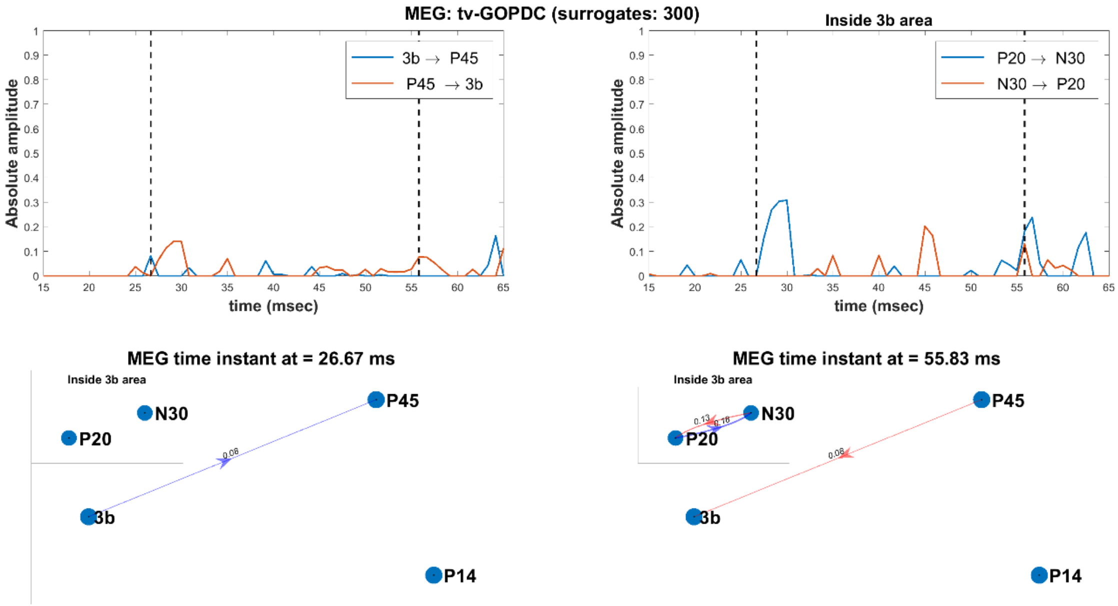

Figure 3. 14: The tv-GOPDC causalities of the functional component (above) and the graphical representation of these causalities at specific time instant of interest (dashed vertical lines) for the MEG modality.

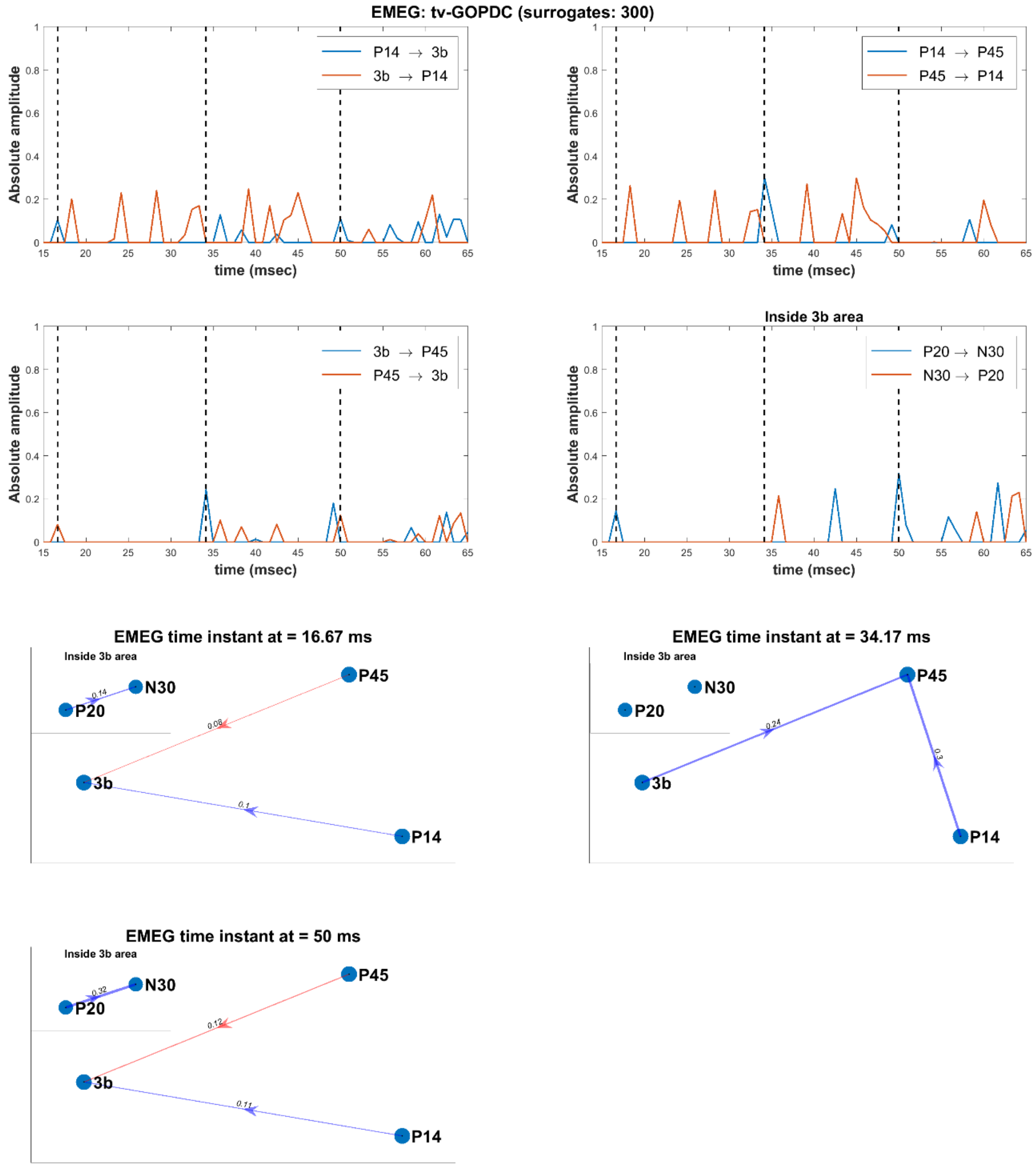

Figure 3. 15: The tv-GOPDC causalities of the functional component (above) and the graphical representation of these causalities at specific time instant of interest (dashed vertical lines) for the EMEG modality.

A general observation related to our results is that the graphs among the modalities have very similar information for the three time instants, which may differ within a limit of $\pm 5\ ms$ around their peaks (Table 1). More specifically, let us compare the graphs of three modalities at the same time instants (graphs: Figure 3. 13, Figure 3. 14 and Figure 3. 15). The first time instant shows activation in EEG and EMEG, with EMEG reflecting more reasonable amplitudes enhancing the causality of P14 → 3b and suppressing the causality of P45 → 3b. At the second time instant, all modalities have pointed out the forward propagation from 3b to P45, with EEG and EMEG to give higher amplitudes for 3b → P45 and P14 → P45 in comparison with MEG. For the last time instant, the only difference between the modalities apart from amplitudes is that the MEG has a backward propagation from N30 to P20. In regards to the tv-GOPDC interactions, we will further discuss each two-way communication separately (tv-GOPDC: Figure 3. 13, Figure 3. 14 and Figure 3. 15):

- The interactions P14 ↔ 3b:

  The component P14 starts first and conveys information to 3b area. Subsequently (in following time instants), a frequent interaction between them occurs. This situation is illustrated in both EEG and EMEG, with the difference that in the EMEG the backward propagation from 3b is more intense.

- The interactions P14 ↔ P45:

  Similar as above, the exchange of the information happens after the first time instant in both EEG and EMEG. In this case, the forward propagation from P14 in EEG and the backward propagation from P45 in EMEG are more intense.

- The interactions 3b ↔ P45:

  Initially, a small backward propagation from P45 for a short time can be seen in the three modalities. Then, at the second time instant the 3b stimulates the P45 and immediately after that, the P45 responds back with a big amplitude, especially seen in EEG and MEG. Then, the backward propagation from P45 stays in lower amplitudes until the third time instant, which is more intense in MEG and EMEG.

- The interactions inside the 3b area P20 ↔ N30:

  The interactions between P20 and N30 are sparse and remain in low amplitudes except for the small windows around the time instants of interest.

CHAPTER 4: DISCUSSION, CONCLUSION AND FUTURE WORK

4.1 DISCUSSION

In this study, we examined the connectivity of the early somatosensory components P14, P20, N30 and P45 at low frequencies for the modalities EEG, MEG and EMEG. Our main goal was to investigate the connectivity between these components for each modality by using a pipeline that combines relevant techniques in a modular way. The first step after preprocessing was the separation of the somatosensory components from the time-locked EEG and MEG data with the functional source separation (FSS). Therefore, this process for every component separately produced the corresponding functional source (FS). The FSs are more enhanced around their corresponding component peaks (Table 1) and are more suppressed at the regions of other components. These conclusions are verified from the comparison of the back-projection data of each FS with the measurement data (Figure 3. 6 and Figure 3. 7). The combined EMEG is computed using the back-projected data of the same k EEG and MEG components with the exception of first component, which is not detected by the MEG. We applied source localization for every component of each modality (EEG, MEG or EMEG) and for each time point by exploiting the algorithm sLORETA to compute the source waveforms. Three significant observations are derived from the source localization results. The first is that accurate source localization is achieved for each modality, since the orientation and position of each activation/dipole are close to the real ones (Figure 3. 9, Figure 3. 10 and Figure 3. 11). The second is that the source waveforms preserve the corresponding enhancement around the peaks of the functional components and the suppression of other activations (Figure 3. 12). The third point is that the EMEG achieved better localization for the component P14, which is located nearest to the VPL of the Thalamus, while combining information of the EEG and MEG amplitudes of the source waveforms (18.33 ms at Figure 3. 11 and EMEG source waveforms at Figure 3. 12). Finally, the connectivity is computed from the source waveforms for each modality by using tv-GOPDC and the assessment of its significance is derived by an empirical distribution, which is produced by three hundred surrogate data with a significance threshold of 90% (Figure 3. 13, Figure 3. 14 and Figure 3. 15). The final graphs point out three important directional causalities: one thalamocortical $P14 \rightarrow 3b$ and two corticocortical $3b \rightarrow P45$ and $P45 \rightarrow 3b$ at the corresponding time instants. The results show that the three modalities share similar information with some small differences mainly to amplitude. In addition, the EMEG results reflect amplitudes more accurate, since it combines complementary information from EEG and MEG. The authors in (Barbati, et al., 2006) by using FSS achieve to enhance the somatosensory functional sources for MEG data. Furthermore, a similar study (Porcaro, et al., 2013) utilized the FSS method for the extraction of EEG low and high frequencies in early somatosensory components from a grand average of six subjects. The source waveforms of the source localization were produced by using the simple four concentric conductive spheres head model and the method of dipole fitting. The data was acquired by a 32-channels EEG and the montage was referenced to auricular electrodes, with a sample frequency of $4096\ Hz$ and 1000 trial. The connectivity results were acquired by the PDC and the assessment of significance was derived by bootstrap resampling technique with threshold at p = 0.01. This study showed that FSS was able to derive components that accurately reconstruct the activities of the brain in somatosensory experiments. In our study, we enhance these results by using more detailed analysis with a more realistic head model, better spatial and temporal resolution, more detailed connectivity model and combined information from EEG and MEG. Furthermore, the FSS method has been recently used in (Ji, et al., 2019) for the fusion of EEG and fMRI data for the study of visual evoked potentials.

4.2 CONCLUSION

This study proposes a subject specific pipeline for the exploration of functional connectivity for event-related brain activities which are recorded by non-invasive EEG and MEG measurements. Furthermore, it takes into account the combined EMEG that can bring out the complementary information of the EEG and MEG, which can be considered essential for many other studies. Last but not least, the realistic head model that is used in source localization comprises six compartments (skin, skull compacta, skull spongiosa, cerebrospinal fluid (CSF), gray and white matter) including the anisotropies of the white matter and skull can leads to results close to the real ones.

4.3 FUTURE WORK

As future work we can apply the same connectivity pipeline for a larger number of subjects with the grand average on functional sources and the source localization on a common head model. In this way, the functional sources will isolate more clearly the corresponding activity and reduce the irrelevant signal. Additionally, if we acquire data with more trials the investigation of P25 component could be performed including Brodmann's area 1 in the connectivity analysis. A comparison of the low and high frequencies of the short and long latency sensorimotor components will also form an interesting investigation. In this case, the current study will be expanded into the motor network and will search if the high frequencies include extra information that is not visible in low frequencies. Finally, we can compare the primary somatosensory network before and after the transcranial direct-current stimulation (tDCS) (Antonakakis, et al., 2019; Khan, et al., 2019) to investigate if we can achieve significant enhancement on the connectivity.

BIBLIOGRAPHY

Akaike, H., 1974. A new look at statistical model identification. *IEEE Transactions,* Volume 19, pp. 716-723.

Allison, T., McCarthy, G. & Wood, C. C., 1992. The relationship between human long-latency somatosensory evoked potentials recorded from the cortical surface and from the scalp. *Electroencephalography and clinical Neurophysiology,* Volume 84, pp. 301-314.

Allison, T., McCarthy, G., Wood, C. C. & Jones, S. J., 1991b. Potentials evoked in human and monkey cerebral cortex by stimulation of the median nerve. A review of scalp and intracranial recordings. *Brain,* Volume 114, p. 2465–2503.

Allison, T., Wood, C. C., McCarthy, G. & Spencer, D. D., 1991a. Cortical somatosensory evoked potentials. II. Effects of excision of somatosensory or motor cortex in humans and monkeys. *Journal of Neurophysiology,* Volume 66, pp. 64-82.

Antonakakis, M. et al., 2019. *Individual targeting and optimization of multi-channel transcranial electric stimulation of the human primary somatosensory cortex.* s.l., 41st Int. Eng. in Medicine and Biology Conf. (EMBC), Berlin, July 23-27.

Antonakakis, M. et al., 2018. *Combined EEG/MEG source analysis for presurgical epilepsy diagnosis using calibrated realistic volume conductor model.* Philadelphia, USA, 21th Int.Conf.on Biomagnetism (Biomag2018), Aug.26-30.

Aydin, Ü. et al., 2017. Zoomed MRI Guided by Combined EEG/MEG Source Analysis: A Multimodal Approach for Optimizing Presurgical Epilepsy Work-up and its Application in a Multi-focal Epilepsy Patient Case Study. *Brain topography.*

Aydin, Ü. et al., 2014. Combining EEG and MEG for the reconstruction of epileptic activity using a calibrated realistic volume conductor model. *PLoS One,* 9(3), p. e93154.

Baccalá, L. A. & Sameshima, K., 2001. Partial directed coherence: a new concept in neural structure determination. *Biological Cybernetics,* Volume 84, pp. 463-474.

Baccalá, L. & Medicina, F. d., 2007. Generalized Partial Directed Coherence. *presented at the 15th International Conference on Digital Signal Processing, Cardiff, UK.*

Barbati, G. et al., 2006. Functional source separation from magnetoencephalographic signals. *Human Brain Mapping,* Volume 27, pp. 925-934.

Bastos, A. M. & Schoffelen, J.-M., 2016. A Tutorial Review of Functional Connectivity Analysis Methods and Their Interpretational Pitfalls. *Frontiers in Systems Neuroscience,* p. 9.

Bast, T. et al., 2007. Combined EEG and MEG analysis of early somatosensory evoked activity in children and adolescents with focal epilepsies. *Clinical Neurophysiology,* Volume 118, pp. 1721-1735.

Buchner, H. et al., 1994. Source analysis of median nerve and finger stimulated somatosensory evoked potentials: multichannel simultaneous recording of electric and magnetic fields combined with 3D-MR. *Brain Tomography,* Volume 6, p. 299–310.

Ding, M., Bressler, S. L., Yang, W. & Liang, H., 2000. Short-window spectral analysis of cortical event-related potentials by adaptive multivariate autoregressive modeling: Data preprocessing, model validation, and variability assessment. *Biological cybernetics,* Volume 83, pp. 35-45.

Esser, S. et al., 2006. A direct demonstration of cortical LTP in humans: A combined TMS/EEG study. *Brain Research Bulletin,* 69(1), pp. 86-94.

Frank, E., 1952. Electric Potential Produced by Two Point Current Sources in a Homogeneous Conduction Sphere. *Journal of Applied Physics,* 23(11), pp. 1225-1228.

Fuchs, M. et al., 1998. Improving source reconstructions by combining bioelectric and biomagnetic data. *Electroencephalography and clinical neurophysiology,* Volume 107, pp. 93-111.

Galán, J. G. N., 2013. *Functional and effective connectivity in MEG: Application to the study of epilepsy,* s.l.: s.n.

Grech, R. et al., 2008. Review on solving the inverse problem in EEG source analysis.. *Journal of NeuroEngineering and Rehabilitation,* pp. 5-25.

Gross, J. et al., 2013. Good practice for conducting and reporting MEG research. *NeuroImage,* Volume 65, pp. 349-363.

Hallez, H. et al., 2007. Review on solving the forward problem in EEG source analysis. *Journal of NeuroEngineering and Rehabilitation,* pp. 4-46.

Hämäläinen, M. et al., 1993. Magnetoencephalography - theory, instrumentation, and applications to noninvasive studies of the working human brain. *Reviews of Modern Physics,* 65(2), pp. 413-497.

Hämäläinen, M. & Ilmoniemi, R., 1994. Interpreting magnetic fields of the brain: minimum norm estimates. *Medical & Biological Engineering & Computing,* Volume 32, pp. 35-42.

Handy, T., 2005. *Event-Related Potentials: A Methods Handbook.* s.l.:The MIT Press.

Hansen, P. C., Kringelbach, M. L. & Salmelin, R., 2010. *MEG: An Introduction to Methods.* s.l.:Oxford university press.

Hassan, M. et al., 2014. EEG Source Connectivity Analysis: From Dense Array Recordings to Brain Networks. *PloS one.*

Haueisen, J. et al., 2007. Identifying mutual information transfer in the brain with differential-algebraic modeling: evidence for fast oscillatory coupling between cortical somatosensory areas 3b and 1. *NeuroImage,* Volume 37, p. 130–136.

Hyvärine, A., Karhunen, J. & Oja, E., 2001. *Independent component analysis.* s.l.:A Wiley-Interscience Publication.

Hyvärinen, A. & Oja, E., 2000. Independent component analysis: algorithms and applications. *Neural Networks,* Volume 13, pp. 411-430.

Ioannides, A., 2007. Dynamic functional connectivity. *Current Opinion in Neurobiology,* Volume 17, p. 161–170.

Ji, H. et al., 2019. Functional Source Separation for EEG-fMRI Fusion: Application to Steady-State Visual Evoked Potentials. *Frontiers in Neurorobotics,* Volume 13.

Jolliffe, I., 2002. *Principal Component Analysis.* 2nd ed. New York, NY: Springer-Verlag.

Kamiński, M., Ding, M., Truccolo, W. A. & Bressler, S. L., 2001. Evaluating causal relations in neural systems: Granger causality, directed transfer function and statistical assessment of significance. *Biological Cybernetics,* 85(2), pp. 145-157.

Kandel, E. R. et al., 2013. *Principles of neural science.* 5th ed. s.l.:McGraw Hill.

Khan, A. et al., 2019. *Constrained maximum intensity optimized multi-electrode tDCS targeting of human somatosensory network.* s.l., 41st Int. Eng. in Medicine and Biology Conf. (EMBC), Berlin, July 23-27, accepted for publication.

Kibble, J. & Halsey, C., 2008. *Medical Physiology: The Big Picture.* s.l.:McGraw Hill.

Kirkpatrick, S., Gelatt, C. D. & Vecchi, M. P., 1983. Optimization by simulated annealing. *Science,* Volume 220, pp. 671-680.

Larsson, J., 2007. Electromagnetics from a quasistatic perspective. *American Journal of Physics,* 75(3), pp. 230-239.

Lehmann, D. & Skrandies, W., 1980. Reference-free identification of components of checkerboard-evoked multichannel potential fields. *Electroencephalography and Clinical Neurophysiology,* 48(6), pp. 609-621.

Lucka, F., Pursiainen, S., Burger, M. & Wolters, C. H., 2012. Hierarchical Bayesian inference for the EEG inverse problem using realistic FE head models: depth localization and source separation for focal primary currents. *NeuroImage,* 61(4), pp. 1364 -1382.

McCorry, L. K., 2009. *Essentials of human physiology for pharmacy.* second edition ed. Boca Raton: CRC Press/Taylor & Francis: s.n.

Naik, G. R. & Wang, W., 2014. *Blind Source Separation: Advances in Theory, Algorithms and Applications.* s.l.:Springer Publishing Company.

Omidvarnia, A. et al., 2013. Measuring Time-Varying Information Flow in Scalp EEG Signals: Orthogonalized Partial Directed Coherence. *IEEE Transactions on Biomedical Engineering,* 61(3), pp. 680-693.

Oostenveld, R., Fries, P., Maris, E. & Schoffelen, J. M., 2011. FieldTrip: Open source software for advanced analysis of MEG, EEG, and invasive electrophysiological data. *Computational Intelligence and Neuroscience,* Volume vol. 2011, Article ID 156869.

Pascual-Marqui, R., 2002. Standardized low resolution brain electromagnetic tomography (sLORETA): technical details.. *Methods & Findings in Experimental & Clinical Pharmacology Author's version.*

Porcaro, C. et al., 2013. Multiple frequency functional connectivity in the hand somatosensory network: An EEG study. *Clinical Neurophysiology,* Volume 124, p. 1216–1224.

Purves, D. et al., 2004. *Neuroscience (3rd ed.).* s.l.:Sunderland, MA, US: Sinauer Associates..

Rullmann, M. et al., 2009. EEG source analysis of epileptiform activity using a 1mm anisotropic hexahedra finite element head model. *NeuroImage,* 44(2), pp. 399-410.

Sanei, S. & Chambers, J. A., 2007. *EEG signal processing.* Centre of Digital Signal Processing Cardiff University, UK: John Wiley & Sons Ltd.

Schneider, T. & Neumaier, A., 2000. Algorithm 808: ARfit - a MATLAB package for the estimation of parameters and eigenmodes of multivariate autoregressive models. *ACM Transactions on Mathematical Software.*

Schwarz, G., 1978. Estimating the Dimension of a Model. *The Annals of Statistics*, 6(2), pp. 461-464.

Sharon, D. et al., 2007. The advantage of combining MEG and EEG: Comparison to fMRI in focally stimulated visual cortex. *NeuroImage,* Volume 36, pp. 1225-1235.

Sternberg, R. J. & Sternberg, K., 2012. *Cognitive Psychology.* Sixth Edition ed. s.l.:Wadsworth Cengage Learning.

Vallaghé, S., 2008. *EEG and MEG forward modeling : computation and calibration,* s.l.: s.n.

Vorwerk, J., Aydin, Ü., Wolters, C. & Butson, C., 2019. Influence of Head Tissue Conductivity Uncertainties on EEG Dipole Reconstruction. *Frontiers in Neuroscience.*

Widmaier, E. P., Raff, H., Strang, K. T. & Vander, A. J., 2008. *Vander's human physiology: The mechanisms of body function.* Boston: McGraw-Hill Higher Education: s.n.

Wolters, C. H. et al., 2006. Influence of tissue conductivity anisotropy on EEG/MEG field and return current computation in a realistic head model.. *NeuroImage*, Volume 30, pp. 813-826.